Structural and Compositional Analysis of Pristine and Cycled Li Ion Battery Cathode Material $Li_wMn_xCo_yNi_zO_2$

By

FEI YANG, B.Eng.

A Thesis

Submitted to the School of Graduate Studies

in Partial Fulfilment of the Requirements

for the Degree

Master of Applied Science

McMaster University

MASTER OF APPLIED SCIENCE (2014) McMaster University

(Materials Science and Engineering) Hamilton, Ontario

TITLE: Structural and Compositional Analysis of Pristine and Cycled Li Ion Battery Cathode Material $Li_wMn_xCo_yNi_zO_2$

AUTHOR: Fei Yang, B.Eng. (Xi'an Jiaotong University)

SUPERVISOR: Professor Gianluigi A. Botton

NUMBER OF PAGES: xvi, 116

Abstract

Rechargeable lithium ion batteries are common materials in everyday applications. The most frequently used cathode material, $LiCoO_2$, provides high energy density and stable charge/discharge performance. However, $LiCoO_2$ is toxic and relatively expensive, therefore, other alternatives are being sought after in the development of battery materials, such as $LiMn_{0.33}Ni_{0.33}Co_{0.33}O_2$ (identified commonly as 333 compound). The 333 compound is now popular due to its comparable performance with $LiCoO_2$, lower price, enhanced stability, and more environmentally friendly characteristics. In addition, $Li_{1.2}Mn_{0.54}Ni_{0.13}Co_{0.13}O_2$ (HENMC) is still on the stage of testing and it attracts wide attention due to its higher rechargeable capacity and thermal stability. However, there are still challenges confronted: cycle stability and low rate capability.

In order to verify all the roles played by different elements shown in NMC materials and explore the corresponding performance with different formula units, compositional analysis is needed. ICP-MS (inductively coupled plasma mass spectrometry) can provide bulk compositional information and has been used in recent work, giving a general idea of the composition of NMC materials. However, compositional inhomogeneity analysis has usually been neglected in these studies. Therefore, the objective of this work was to explore this variation in composition locally with higher spatial resolution, at the NMC particle level. This work was carried out through the use of scanning electron microscopy – energy dispersive spectroscopy (SEM-EDS) and Auger electron spectroscopy (AES). Furthermore, nano-scale quantitative analysis was done with transmission electron microscopy – energy dispersive spectroscopy (TEM-EDS). Moreover, an optimal approach and procedure of compositional analysis by using EDS and AES was explored with proper standards and operation conditions to provide consistent and stable results.

The optimal quantification method was applied to investigate the compositions of 333 compound before and after ball milling and HENMC specimen before and after cycling. The results support the structural changes and in turn the electrochemical performance of the battery material. In the 333 compound, the electrochemical performance of the battery

was deteriorated due to ball milling, during which Zr was introduced and particles were more compact. In HENMC, during cycling, the Mn distribution was homogeneous at the beginning, then inhomogeneous and homogeneous again, supporting the hypothesis of the transformation of phases: formation of spinel phase and potential SEI layer.

In-depth structural analysis of different NMC materials has been reported previously by other groups. However, the structural effects due to cycling, within particles still needs investigation. Therefore, X-ray diffraction (XRD) was used to investigate the bulk material crystalline structure. Local nano-scale level structural variations amongst different isolated primary particles were investigated by the electron diffraction pattern based on TEM. The 333 compound and HENMC cycling was examined before and after cycling. After cycling, in the 333 compound, the O1 phase domains with P-3m1 space group appear inside the O3 phase with R-3m lattice. With more cycling, more domains appear. For HENMC, the original pristine samples exhibit the rhombohedral and monoclinic phases. After cycling, more and more spinel phase appear. Finally, after 100 cycles, we observe evidence of the potential solid electrolyte interphase (SEI) formation.

In all, all the results above support the phase changes of 333 compound and HENMC. More investigations are needed to understand the degradation process of both compounds.

Acknowledgement

This thesis would not have been possible without the consistent help and support from the nice and wonderful people around me. My first and foremost thanks would give to my supervisor, Dr. Gianluigi Botton for all the guidance and support through my entire graduate career. On both academic and personal level, I learned many things from him that would absolutely benefit me in the future.

I would also acknowledge the whole group members for giving me all those valuable and memorable time for my graduate life. I would like to thank Lis Melo and Andrew Scullion who helped me with ideas on my work and sacrificed their time for the correction of my thesis. Along with Shooka Mahboubi and Steffi Woo who taught me the indexation of diffraction patterns and supported me with on my project in a number of ways. I also want to thank Travis Casagrande and Carmen Andrei for all sorts of technical support for the microscopes.

In addition, I am grateful to have Dr. Gillian Goward and Mark J. R. Dunham as my collaborator for providing me samples and sharing ideas on the project. I also want to thank Dr. Joey Kish and Dr. Gillian Goward to be my committee members and give me advice.

At the end, I want to thank my friends and family, especially for Darko Ljubic, who spent his precious time checking my whole manuscript while I was writing. I also appreciate the support from my parents sincerely. Thank you for always keeping me company and support my back no matter what.

List of Figures

List of Tables

List of Abbreviations

333 compound: $LiCo_{0.33}Ni_{0.33}Mn_{0.33}O_2$

BF: Bright Field

BNMC: Ball-milled NMC

BSE: Backscattered Electron

BSEI: Backscattered Electron Image

CV: Cyclic Voltammetry

EDS: Energy Dispersive Spectroscopy

ED: Electron Diffraction

HENMC: High Energy $Li_{1.2}Co_{0.13}Ni_{0.13}Mn_{0.54}O_2$

ICP: Inductively Coupled Plasma

ICSD: Inorganic Crystal Structure Database

LCO: $LiCoO_2$

LT: Low Temperature

HT: High Temperature

LMO: $LiMn_2O_4$

LNO: $LiNiO_2$

NMP: N-methyl-2-pyrrolidone

NMR: Nuclear Magnetic Resonance

ND: Neutron Diffraction

PVDF: Polyvinylidene Fluoride

SE: Secondary Electron

SEI: Secondary Electron Image

SEM: Scanning Electron Microscope

TEM: Transmitting Electron Microscope

TMO: Transition Metal Oxide

WDS: Wavelength Dispersive Spectroscopy

XRD: X-ray Diffraction

Table of Contents

Ch 1. Introduction

Lithium ion (Li-ion) batteries have attracted widespread attention due to their high electrical capacity, high energy and power density and long cycle life with a low self-charge effect ever since they hit the market. Both in consumer electronic devices such as mobile phones, digital cameras and laptop computers, and in energy storage devices for hybrid electric vehicles, biomedical applications and even space technology, Li-ion batteries are used practically everywhere.[1] However, the electrochemical performance of the Li-ion batteries is limited by component variability and design deficiencies such as high cost, low environmental compatibility, thermal safety issues and inadequacy in high-power applications.[2]

One alternative solution to the problems associated with the Li-ion batteries is to find the optimal electrode materials, and to build a stable and efficient electrolyte.[3] Moreover, materials have to be customized considering cost, safety and applications in different working conditions and environment.[4,5]

A schematic of the battery charging/discharging mechanism is presented in Fig. 1-1. In this model, this battery consists of a solid transition metal oxide (TMO) as the cathode, Li metal foil as the anode and $LiPF_6$ as the electrolyte. When it is charging as shown in Fig. 1-1, the mobile guest Li ions are released from the host network of the solid (TMO) in the cathode, and are injected into the Li metal foil.

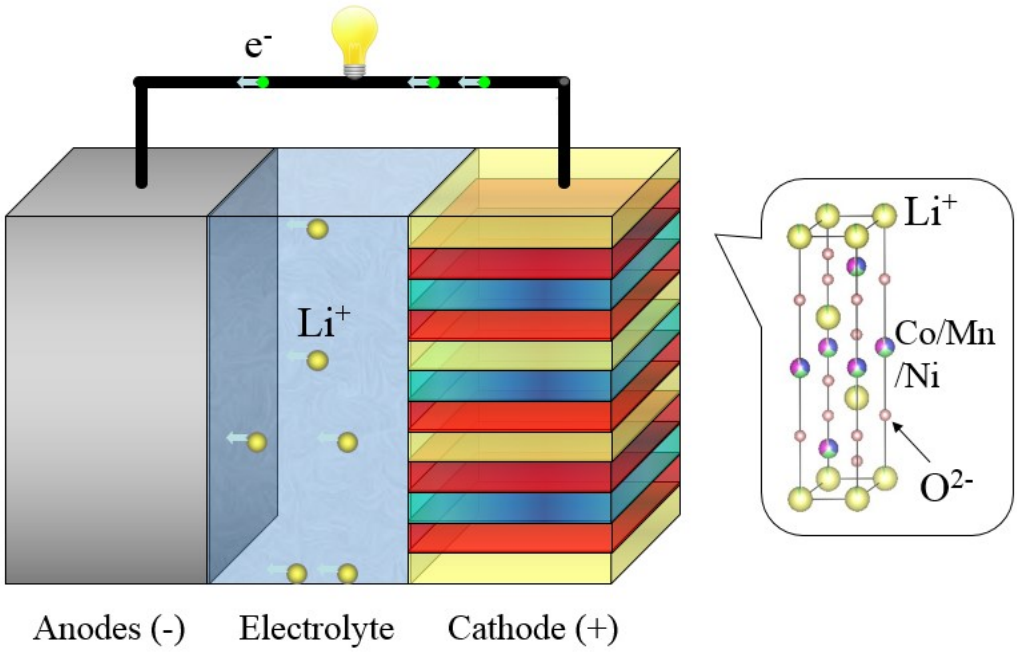

Figure 1-1: Charging process of the Li-ion battery.

On the other hand, when it is discharging, the Li-ions travel from the Li metal foil anode back to the TMO cathode which is in the opposite direction of the inner and outer circuit compared to the charging process.

1.1. Components of Li-ion battery

In terms of anode materials, Li metal possesses highest capacity related to weight, high electron exchange and energy transformation proficiency, high cell-voltage and long shelf-life. Even though Li-foil anode is commonly used in commercial products, some problems remain to be solved: reaction with electrolyte, short-circuiting of the cell due to dendrite production, and interaction with the environment. Therefore, the Li metal anode is gradually being replaced by carbon-based insertion electrodes, such as graphene, that can circumvent the problems listed above.[6]

As for the cathode materials, the intercalated solid compounds are employed. During the process of charging and discharging, the Li-ions enter and leave the cathode host network and affect the host structure slightly. In this way, the lithiation and delithiation are not hindered by the configuration of the cathode so that this process is mostly reversible

and hence suitable for rechargeable batteries. The positive Li^+ guest ions are absorbed around the negative O^{2-}, and repulsed by the positive transition metal ions. Different host structures provide different sites for Li^+.[7]

Overall, three common types of cathodes are utilized in commercial products[8]:

1. Li-based transition metal oxides, e.g. $LiCoO_2$ (or LCO for short) and $LiNiO_2$ (or LNO for short) with a layered structure have advantages (high capacity, easy synthesis, excellent cycle ability) and disadvantages (structural changes, high toxicity and high cost). Several approaches such as doping, nanocrystallization, coating and transition metal exchange, are applied to solve the challenges confronted.

2. Li-based transition metal oxides, e.g. $LiMn_2O_4$ (or LMO for short) with a spinel structure, are used to reduce the cost and environmental impact. However, considerable limitations on capacity fading were introduced by structural changes, Mn dissolution and lattice distortion. By introducing Ni or nanocrystalline cathodes, the performance of this type of batteries can be improved.

3. Li-based transition metal phosphates (e.g. $LiFePO_4$), offer low cost, low toxicity and long cycle life with excellent reversibility. Moreover, dramatic increases in conductivity can be seen by doping with high valence cations. The cycling rate capability is improved by incorporating conductive carbon, and synthesis of nanoscale $LiFePO_4$ particles.

However, there are some comparatively new cathode materials, $LiMn_xCo_yNi_zO_2$ (or NMC for short). A combination of all three transition metals with different compositions merges all the advantages and disadvantages to various degrees, which is of interest in this work.

Except for the electrodes as the main part of the Li-ion batteries, there are other indispensable components to an operational battery, namely the electrolyte, the separator, the binder, etc. The diversity of each component renders the Li-ion batteries assorted applications.[9]

1.2. Roles of Elements

Three transition metals render the Li-based transition metal oxide different properties in the structure and performance. Generally, the introduction of Mn^{4+} in NMC improves the

thermal stability compared to LCO. In terms of the electrochemical reaction, the electro-active species Ni^{2+}/Ni^{4+} and Co^{3+}/Co^{4+} are used. When it is charging, the Li^{+} is released from the cathode, Ni^{2+} and Co^{3+} are oxidized to Ni^{4+} and Co^{4+}, respectively, and vice versa during discharge process. Particularly, the use of the Ni^{2+}/Ni^{4+} redox couple can maintain the theoretical capacity of the material, since Co^{3+}/Co^{4+} electro-active species are replaced by thermally inactive Mn^{4+}. As for Co, it provides better crystallinity, less cation mixing, and a change of particle morphology from octahedral to sphere-shaped with size around 200–350 nm.

The mixing of the Li ions and transition metal cations between the two layers forms a "disordered" rock salt structure. Therefore, the degree of cation exchange determines the disorder extent, which occurs more often between Ni^{2+} and Li^{+} in NMC, as a result of their similar size. In $LiNiO_2$, around 2% of the Ni content exist in the Li layer which significantly decreases the cycling life. However, by substitution of Mn in $LiNiO_2$ to form $LiNi_{0.5}Mn_{0.5}O_2$, the consequence of ions mixture is the rearrangement of Li, Ni, and Mn in the transition metal layers. In this manner, further Co substitution decreases the degree of cation disorder, and this has resulted in the increase in the Li extraction rate in the composition of $LiCo_{1-2x}Ni_xMn_xO_2$. In addition, a slight stoichiometric excess of lithium is beneficial to the charging-discharging capability and cycling behavior, which has drawn the interest in the research of Li-rich high energy cathode material.[10]

In all, the elemental composition in the Li-ion transition metal oxide is closely related to the structure and in turn the performance. However, not enough composition analysis in the powders has been done, not to mention the compositional information inside the secondary particles or even in primary nano-scale particles. Therefore, in this project, the composition of NMC particles is carefully analyzed, especially under micro-level or even nano-level. The comparison of compositions are made before and after ball-milling preparation, and before and after different charging and discharging cycles.

1.3. Objective

The general objective of this thesis is to acquire local compositional and structural information from Li-ion battery cathode material $LiMn_{0.33}Co_{0.33}Ni_{0.33}O_2$ and $Li_{1.2}Mn_{0.54}Co_{0.13}Ni_{0.13}O_2$ (labeled here after as "333" compound and HENMC respectively)

in order to establish a clearer connection between structure and measurements of performance as part of subsequent work.

In the compositional aspect, the first step was to find out how to accurately quantify the distribution of all transition metals and Li inside NMC particles with standards using different techniques: Scanning Electron Microscopy (SEM) based Energy Dispersive Spectroscopy (EDS) and Auger Electron Spectroscopy (AES). The objective was to establish the procedure for a higher degree of confidence in the qualitative and quantitative analysis, by employing the proper technique with the respective optimal conditions providing reliable results. Then the quantification technique is used in order to compare cycled and non-cycled, ball-milled and original pristine cathode material.

As for the investigation of the local crystallographic structure of NMC, Transmission Electron Microscopy (TEM) Selected Area Electron Diffraction (SAED) was utilized. The space group, structure and phase inside NMC particles were investigated. Through the examination of $LiMn_2O_4$, $LiCoO_2$, $LiNiO_2$ using electron diffraction and a literature review of all Mn-Co-Ni combination in Li-ion battery cathode materials, the effects of the mixture of all transition metals are discussed. Moreover, cycled and non-cycled NMC particles and high-energy NMC were compared to see the changes of the structure as well.

Ch 2. Literature review

This project was mainly focused on the compositional and structural analysis of $LiMn_{0.33}Co_{0.33}Ni_{0.33}O_2$ and $LiMn_{0.54}Co_{0.13}Ni_{0.13}O_2$ (333 compound and HENMC). The original Li transition metal oxides found were LNO, LCO and LMO. Then partial replacement of another transition metal was used to form Li-based double transition metal dioxides as the cathode. This idea provides a new approach to improve the performance of the cathode. Therefore, compounds with three transition metals Mn, Co and Ni of different compositions have been attempted. By mixing the three transition metals, the advantages of different elements can be customized according to different applications. In general, the electrochemical performance is improved dramatically and the capacity can be retained better. Specifically, "C" is used as the unit for measuring the charging-discharging rate, and 1C means the maximum safe continuous discharge rate of a battery batch (usually C is expressed in mA hours, so unit of C-rate is mA).

2.1. Triple-element cathode

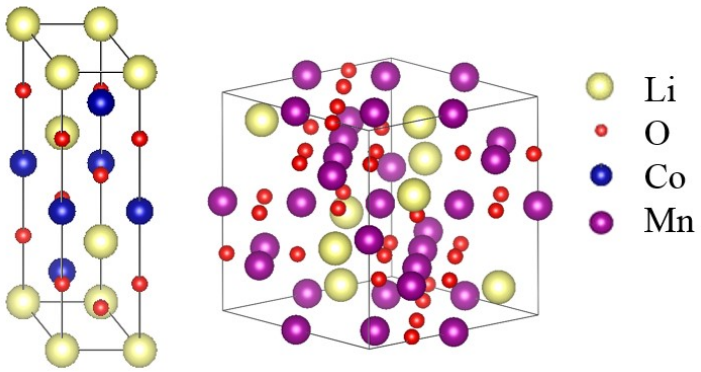

a) b)

Figure 2-1 Structural schematic of a) LCO and b) LMO.[11]

$LiCoO_2$

$LiCoO_2$, or LCO for short, was the first commercial cathode material introduced by the SONY company. Because of its success with high capacity reversibility and excellent

charging-discharging ability, much research has been done on this material. However, the high toxicity and cost issues of Co has led to the exploration of alternatives to replace it.[12]

The energy density of LCO is relatively low at around 130 mAh/g because only half of Li ions are involved in reversible cycling without causing cell capacity loss. The capacity loss may be due to the reaction between LCO and the electrolyte, electrolyte decomposition, and small structural changes of the electrode during deintercalation. [13] Two approaches can improve the capacity: coating a metal oxide, and switching to the electrolyte that doesn't react with LCO.[11]

In terms of the charge cutoff voltage, 4.2V is widely adopted as the reversible voltage limit even after 50 cycles. Since when it is above 4.2V, particularly above 4.5V, all the close-packed LCO is transferred to other stacking sequence which disrupts the whole structure.[14,15]

Both layered LCO and spinel LCO exist in the cathode material. Generally, layered LCO has a higher thermodynamic stability, while spinel LCO causes capacity fading of the battery with continual cycling. The layered LCO host structure belongs to the R-3m space group in Figure 2-1 *a)* which easily accommodates large changes of Li guest ions. As long as more than half of the Li ions stay in the structure, the layered structure exists and the whole electrode functions properly.[7]

$LiNiO_2$

$LiNiO_2$, or LNO for short, is inexpensive and less toxic compared to LCO but with an equally high capacity and good reversibility. A comparable cycle life can be achieved with an even larger reversible capacity.[7] The Li chemical diffusion coefficient increases with the increasing deintercalation degree because of the improved electronic transport properties of the cathode.[16]

The LNO current-voltage curve shows higher initial charge and discharge capacities up to 4.4 V. However, it undergoes a much larger capacity fading during long-period charging-discharging than in LCO. This behavior is due to the Ni cations migrating from the transition metal layer to the Li layer, thereby altering the subsequent electrochemical behavior.[14]

During deintercalation of lithium ions from LNO, the hexagonal symmetry R-3m is preserved in Fig. 2-1 a). However, as a battery cathode, it is often not in the pure state. There is a variety of reasons for this effect: the stoichiometric $LiNiO_2$ is hard to obtain since the Ni is always found in the Li layer, which pins the NiO_2 layers together, thereby both the lithium diffusion coefficient and the power capability of the electrode are reduced. Secondly, compounds with low Li concentration might be unstable and even dangerous with organic solvents.[16]

By replacing partial Ni with Co or Al, the performance of LNO is greatly improved. With Co, the ordering in the structure is better kept which reduces the exchange between Li and Ni. On the other hand, Al prevents the complete removal of Li, which stabilize the structure and prevent phase changes that might occur with low content of Li.

$LiMn_2O_4$

$LiMn_2O_4$, or LMO for short, is presently of interest as the cathode of a high-power Li battery for hybrid electric vehicles. Compared to LCO and LNO, LMO has clear advantages of their high specific capacity, in combination with low manufacturing cost, long cycle-life and superior environmental advantages.[7]

However, there is potentially a slow capacity loss during its performance attributed to the oxidation of the electrolyte at the high voltage, slow dissolution of Mn ions and retention of Li atoms after the first charge/discharge cycle.[17] Moreover, as the cathode of a high-power Li battery for hybrid electric vehicles, LMO's capacity is still too low under high discharge rates, so change of electrolyte, substitution of Mn with Al are attempted to solve this problem. [18,19]

In the spinel structure of LMO, which has a Fd3m cubic space group (Fig. 2-1 b)), the oxygen atoms are coordinated octahedrally around Mn and tetrahedrally around Li.[6] That is to say, the Li atom reside in the interstices, and forms a tetrahedron with four oxygen atoms. In this way, 3-D network channels were formed so that Li atoms can be inserted and leave smoothly.[7]

2.2. Li-based double-transition-metal mixture cathode

Even though LCO, LNO and LMO are still the most common cathode materials in commercial batteries, alternative materials are being searched for better electrochemical performance. Substitution of transition metal atoms is one of the main approaches and much work has been done along this way. In a R-3m rhombohedral structure like in LCO, by exchange of transition metals, both Li and transition metal layers are changed, and in turn, the stability of the Li removal, energy density and the retention of capacity during cycling are greatly improved.

$LiNi_{1-y}Co_yO_2$

In the $LiNi_{1-y}Co_yO_2$ system, the whole structure is more ordered with the increase of Co content. When the value of "y" increases to 0.3, there is no Ni content found in the Li layer. That is to say, Co suppresses the migration of Ni ions to the Li site in the compound, which is the same case in NMC compounds.[20,21]

The electronic conductivity of $LiNiO_2$ is the highest among the triple element Li transition metal oxides.[7] Therefore, with the Co substitution in LNO, the conductivity is reduced.[21]

The addition of elements such as Mg and Al reduces the effects of capacity loss and Li ions are not removed completely, thus minimize the possibility of structural collapse. In $LiNi_{1-y-z}Co_yAl_zO_2$, during charging the Ni is oxidized first and then Co. It can be cycled 1000 times with an energy density of 120-130 W·h/kg.[22]

$LiMn_{1-y}Co_yO_2$

By ion exchange, Co-substituted $LiMn_{1-y}Co_yO_2$ is synthesized with a rhombohedral structure. Like LMO, this material convert to the spinel structure during cycling even at a low rate, and it becomes apparent after the 30th cycle. At elevated temperature, the transformation is faster.[23,24]

Substitution of Mn ions with Co, Fe or Ni can boost the electronic conductivity. However, Co-substituted rhombohedral structure materials where the Mn is the redox-

active ion are not used in commercial batteries anymore because it is hard to maintain the structure and keep it from converting to the spinel structure under realistic conditions.[25]

Ni-substituted compounds have become promising since in this case, the Mn becomes the structure stabilizer with a tetravalent state and Ni is the electrochemically active ion between +2 and +4 oxidation states. The Mn here helps in reducing the cost and stabilizes the lattice.

$LiNi_{1-y}Mn_yO_2$

The optimum behavior of $LiNi_{1-y}Mn_yO_2$ material can be achieved when y = 0.5.[26] In particular, the compounds with the composition of $LiNi_yMn_yCo_{1-2y}O_2$, ($0.5 \leq y \leq 0.33$), are treated as a combination of $LiNi_{0.5}Mn_{0.5}O_2$ and $LiCoO_2$ in the form of a solid solution. Data has shown that for $LiNi_{0.5}Mn_{0.5}O_2$, the stable maximum charge potential is set at 4.2V with a capacity of 130 mAh/g.[27] Moreover, by substituting partial transition metal with Li to form Li-rich high energy NMC, the capacity can be increased.

Around 10% Ni can be found on the Li sites, which shows that there is no significant layer stabilization capability because Ni is expected to reduce the rate capacity.[28] Ni is considered as the electrochemically active element in this compound, which cycles between +2 and +4, while Mn remains as +4 independent of Li content. In this way, no Jahn-Teller distortion is involved because of free of Mn^{3+}.

On charging, the Li is firstly removed from Li layer, and then the Li from the transition-metal layer. Only when it is at the highest potential, the Li ions in transition metal layer are removed.[29]

2.3. Li-based triple-transition-metal mixture cathode

2.3.1. Mixed Ni-Mn-Co Dioxide $LiMn_yCo_zNi_{1-y-z}O_2$

Electrochemical properties

Yoshio et al. hypothesized that the addition of Co to $LiMn_{1-y}Ni_yO_2$ made the structure stable. It is found that the amount of exchange between Ni and Li ions are reduced from

$LiMn_{0.2}Ni_{0.8}O_2$ to $LiMn_{0.2}Ni_{0.5}Co_{0.3}O_2$. Moreover, the lithium insertion capacities exceeded 150 mAh/g for the cobalt-substituted compounds. The other mixed Mn-Co-Ni dioxide $LiNi_{0.33}Mn_{0.33}Co_{0.33}O_2$ have a capacity of around 150 mAh/g cycling between 2.5 and 4.2 V as well. If the charge cutoff potential is increased to 5.0V, the capacity can exceed 220 mAh/g, but capacity fade occurs.[30]

Even though all of these materials have good electrochemical performance, their electronic conductivity is still low for a high-rate cathode. By adding the additional excessive amount of a conductor such as carbon black, the conductivity will increase. However, the volumetric energy storage capacity is decreased. By adding Co to $LiNi_{0.5}Mn_{0.5}O_2$ to form $LiNi_{0.4}Mn_{0.4}Co_{0.2}O_2$ (442), the conductivity is increased. While adding Co to $LiNiO_2$ to form $LiNi_{0.8}Mn_{0.2}O_2$, the conductivity is reduced[21]. Therefore the addition of Co which changes the electrochemical behavior has nothing to do with the conductivity. However, the increasing Co content increases the rate capability, which might be associated with fewer Ni ions in the Li layer reducing the diffusivity of Li.

Among all the compositions, 442 has the highest capacity and the ability to maintain it during cycling. The charging potential is critical and an appropriate coating would allow the charging potential and hence the capacity to be increased. For $LiNi_{0.33}Mn_{0.33}Co_{0.33}O_2$ (333 compound), the capacity increases with increasing charging potential. However, sometimes, there is marked capacity fade.[31]

The voltage-capacity curve in different voltage windows vary according to the cut off potential (4.4 – 4.8V), and it varies between 190 and 220 mAh/g. [14] The optimum upper cut off voltage is 4.6V where transformation to the O1 phase (with space group P-3m1) becomes more efficient. Since the O1 phase is not reversible for the battery cycling, it is the main reason why the cathode material deteriorates. The C/10 rate may be sufficiently high such that the transition is over a range of compositions, and/or it occurs at slightly different compositions within different regions in the crystallites due to local cation disorder effects.[32]

Structure

i) Original Material

The X-ray datasets shows that there is an excellent match with all the XRD lines from 333 compound results and the simulated rhombohedral structure in space group R-3m.[2]

More structural data can be shown such as the position of atoms, occupancy and lattice parameters (a = 2.86Å, c = 14.25Å). They are listed in Table 2-1.[32] The structure is shown in Fig. 2-2 a) below.

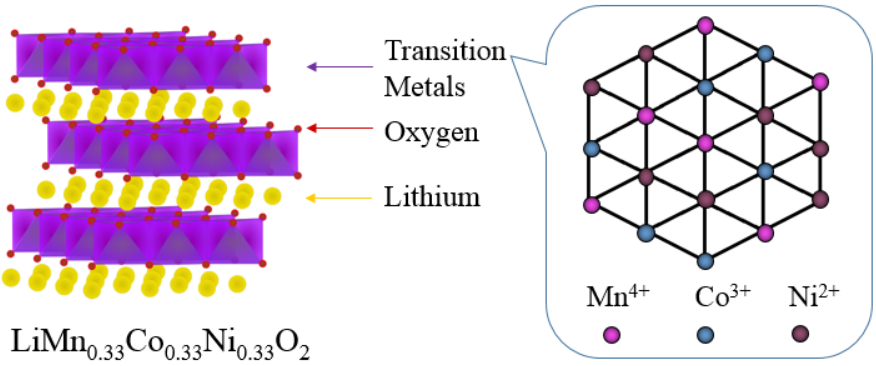

a) b)

Figure 2-2 a) The structure of $LiNi_{0.33}Mn_{0.33}Co_{0.33}O_2$ adapted from Kang's work [35]; b) in the transition metal layer (3a layer), transition metal atoms are distributed randomly.

Table 2-1 Refined NMC site and occupancy of different ions.[33]

Site	Ion	z	Occupancy
3b	Li^+	0.5	0.978
	Ni^{2+}	0.5	0.021
3a	Li^+	0	0.024
	Mn^{4+}	0	0.335
	Co^{3+}	0	0.332
	Ni^{2+}	0	0.309
6c	O^{2-}	0.26	0.024

Three cations with difference valences within a trigonal lattice suggest that they may adopt a special arrangement such as a superlattice. The synchrotron x-ray datasets which provide a good signal to noise ratio, and more contrast shows no long range superlattice.

Neutron diffraction show the same results. It seems that most of the transition metals were consistent with a random distribution over the R-3m 3a sites [Figure 2-3 b)].[32]

It might be the Li/Ni exchange that disrupts long-range metal cation ordering. Because of the small ionic radii difference (Li^+ = 0.76Å, Ni^{2+} = 0.69 Å), it is determined that in the 333 compound, 2-3% of the Ni migrates to the Li site, while Mn and Co remain in the transition metal site. Similarly, in $LiNi_{1/2}Mn_{1/2}O_2$, when Li/Ni position exchange is over 10%, superlattice disappear. However, short-range superlattices might exist and local probe (short-range) techniques, such as selected-area diffraction are used in this thesis.

Moreover, the exchange of Ni^{2+} and Li^+ causes damage to the electrochemical properties like a loss of capacity and lithium diffusion reduction. Cobalt can reduce the number of nickel ions in the lithium layer. On the other hand, a certain level of nickel ions will maintain capacity on cycling at low Li concentration. Therefore there is a need for a determination of the acceptable level of nickel in the Li layer, as it will not be zero.

ii) Charging-Discharging Material

During the charging and discharging, $Li_xCo_{1/3}Ni_{1/3}Mn_{1/3}O_2$, the 333 compound is oxidized to provide $Li_xCo_{1/3}Ni_{1/3}Mn_{1/3}O_2$ (x = 1.0; 0.8, 0.6, 0.45, 0.30, 0.04). S. C. Yin used these samples to examine the structural changes during the cycling.[32]

Li ions are gradually removed from both Li (3b site) and metal (3a site) layer. Between x = 0.6 – 0.4 in $Li_xCo_{1/3}Ni_{1/3}Mn_{1/3}O_2$, all Li ions in 3b site are removed. On the other hand, all of transition metals are pretty stable in their own sites. 333 compound has the same characteristic with $LiCoO_2$, that new phase is formed upon deep extraction of Li. When x > 0.45, the whole material is still O3 phase, which is R-3m space group. However, when x = 0.45, the O1 phase appears, which is P-3m1 space group. When x = 0.3, this phase becomes evident. Moreover, when x reaches 0.26, this phase can be seen in XRD pattern. The Li stoichiometry of the O1 phase is very low or close to zero. Undoubtedly, there is some region converting to O1 phase, but others may be inhibited by forming defects within the structure that impede the “slippage” necessary to accommodate the reaction.

Although the changes in lattice parameter and cell volume are very small from O3 phase to O1 phase. It leads to difficulty in transforming the O1 structure back to the O3 phase. At high upper cutoff voltages for cycling, the deterioration of the electrode might be due

to this. In conclusion the solid solutions of the $LiNi_{0.5}Mn_{0.5}O_2$ material and $LiCoO_2$ which is $LiMn_yCo_zNi_{1-y-z}O_2$, have more than one phases involved during charging and discharging process.

2.3.2. Li-rich mixed-metal dioxides, $Li_{1+x}M_{1-x}O_2$

Nowadays, Li-rich materials are taken into account in designing the optimum composition for the ideal cathode. Excess Li is mostly from the Mn-rich material Li_2MnO_3 and the new material can be considered as a solid solution of Li_2MnO_3 and LMO_2. The M can be Mn, Co, Ni or any mixture of them.[34]

For the transition metals, Mn is used to keep the stability of the lattice in the 333 compound. Since Mn keeps the valence as 4+, so it does not involve any reactions and can keep its position while no dissolution was detected [35]. However, in the case of Mn-rich compound Li_2MnO_3, Mn will take part in the reactions and finally being soluble in the electrolyte. Ni is the electrochemical active member. In Li_2MnO_3-$LiNiO_2$ system, the electrochemical capacity falls rapidly with the nickel content decreased. Moreover, addition of some cobalt to these Li and Mn-rich compounds was reported to help retain the capacity at higher discharge rates.[36]

Stoichiometrically, $Li_{1.2}Mn_{0.42}Co_{0.13}Ni_{0.13}O_2$ (labeled hereafter as HENMC) can be considered as the combination of Li_2MnO_3 and $LiMn_{0.33}Co_{0.33}Ni_{0.33}O_2$ with the ratio of 1:1. The 333 compound will react the same way as in the pure 333 phase as mentioned before, however, the introduction of Li_2MnO_3 gives a different electrochemical property.

Li_2MnO_3 was considered electrochemically inactive, however, in acid environment, or with smaller particle size, it becomes active. When it is charging, Li ions leave both the Li and transition metal layers. The delithiation process always goes with oxygen loss as gas. From the other perspective, in the first cycle, when it is charging, Mn remains 4+ valence, but reduces to 3+ while discharging. During discharging, the local spinel-like structure is observed. This phase is linked directly to the loss of O and the rearrangement of Mn.

Li-rich layered oxides have much higher capacity and thermal stability. The rechargeable capacity can reach 280 $mAhg^{-1}$. The energy density can be as much as twice

of the commercial cathode.[33] However, there are some disadvantages of HENMC that are challenging: cycle stability and low rate capability.[33,37]

Electrochemical properties

The initial discharge capacity of original HENMC and after 50 cycles, are 277.3 and 272.8 mAh/g separately which demonstrates the high capacity and good cycling performance.[38]

There are many reactions occurred in the first cycle. During the charging process, Li ions left the lamellar Li-rich compound while the oxygen is oxidized in the form of gas. So basically, the Li_2O leaves the compound. Both Ni^{2+} and Co^{3+} are oxidized to 4+. However, when it is discharging in the first cycle, since O is gone, the Mn changes its positions and start to form the spinel structure. Meanwhile Ni and Co ions go back to their original valence.[39]

In the XRD pattern, the peaks indicating the cation ordering in the transition metal layers disappear during the first cycle. This shows that the migration of transition metal ions to Li vacancies might cause the irreversible capacity change. Surface modification and mixture with other compounds might change this situation. The formation of micro-cracks might cause the rapid capacity fading. By pre-cycling or coating on the surface, the cycle performance might be improved.[39]

Before the 25^{th} cycles, the capacities of charging-discharging process was increasing with more cycling. However, after that, it goes to the other direction (at least before 100^{th} cycles, it was this trend). This shows that the more and more Mn was activated through the first 25^{th} cycling. Moreover, the charge voltage decrease due to the lower redox reaction of Mn^{3+}/Mn^{4+} than Ni or Co. While in the second stage, because of the instability of this structure formed during long cycling, the capacities decreases. There is a transformation of the layered phase to cubic spinel phase locally gradually completed.[33]

Structure

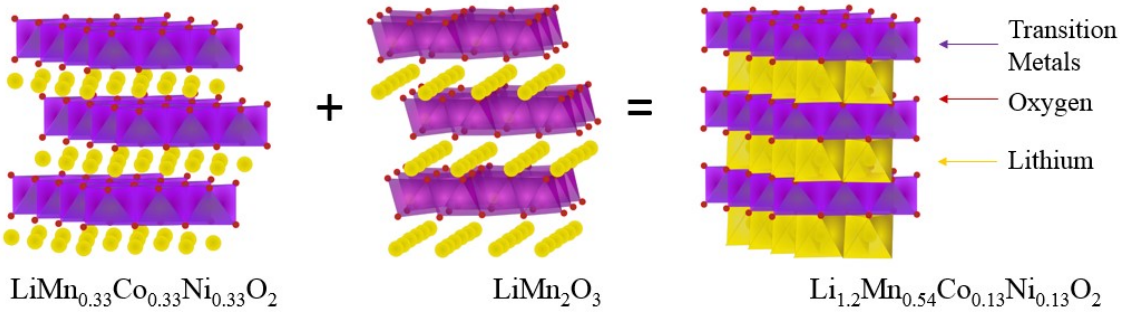

Figure 2-3 The c) $LiMn_{0.42}Co_{0.13}Ni_{0.13}O_2$ is considered as the solid solution of a) $LiMn_{0.33}Co_{0.33}Ni_{0.33}O_2$ and b) Li_2MnO_3.[40]

According to all the strong peaks of X-ray diffraction pattern, typical layered rhombohedral structure of R-3m symmetry is the main structure of HENMC which is the same with one component $LiMn_{0.33}Co_{0.33}Ni_{0.33}O_2$.[41,42] The low intensity superlattice peaks between 20–25° can be indexed to the monoclinic unit cell C2/m, and this is a feature of Li_2MnO_3 type structure. In Li_2MnO_3, the extra Li ions in transition metal layers are usually surrounded by the Mn ions in a regular arrangement, which minimizes the strains in the local lattice and charge compensation. All lithium-rich layered oxides containing Mn possess this feature. [39] In addition, HENMC is the same with the 333 compound in layered oxide structure, which has Li ions at 3a sites, transition metal ions at the 3b sites, and O at the 6c sites.

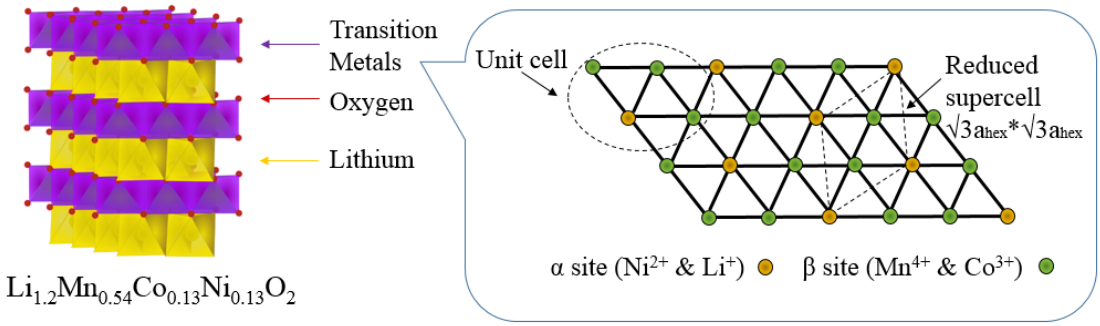

a) b)

Figure 2-4 a) The structure of $Li_{1.2}Mn_{0.42}Co_{0.13}Ni_{0.13}O_2$ adapted from Kang's work [35]; b) in the transition metal layer (3a layer), transition metal atoms are distributed randomly.

In the Li and Mn rich layered materials, the valences of Mn, Co and Ni are usually 4+, 3+ and 2+ respectively. The cations are divided into two groups by the size: larger cations (Ni^{2+} 0.69 Å and Li^{2+} 0.72 Å) and smaller cations (Co^{3+} 0.545 Å and Mn^{4+} 0.53 Å). According to Hideyuki [43], in the possible $\sqrt{3}a_{hex}\times\sqrt{3}a_{hex}$ superlattice, there are α and β sites with the ratio of 1:2. The sites have different sizes shown in Fig. 2-4: the larger cations occupy the α sites and the smaller cations occupy the β sites. The. The transition metal layers will rotate 60° every few layers along the c_{hex} axis. Therefore, depending on the composition of the compound, the local scale of superlattice can be extended more or less.

The original HENMC can be seen as a solid solution of Li_2MnO_3 and $LiMn_{0.33}Co_{0.33}Ni_{0.33}O_2$ without any domains. During the first charge, with the loss of partial ordering in the transition metal layer, a phase separation occurs. With more cycles, there is a continuous structural modification and also a change of the redox couples. Mn ions participate more in the redox processes. In this way, the two phases structure is formed in the end and this can be indicated by the XRD pattern. That is to say, the 333 compound in the bulk remain in the bulk. However, Li_2MnO_3 phase will be oxidized and form more and more $LiMn_2O_4$ on the surface. In this way, two different phases are formed with more cycles, and the phase on the surface will grow up consuming the phase remain in the bulk.

With long-term cycling, because of the acidic species, the cathode surface was etched to form the sponge-like surface which disperse in the solid electrolyte interphase after cycling. The fragmented pieces contain Mn^{2+} which cause the loss of Mn, in turn reduce

the amount of Li stored. In this way, the valence drop becomes the primary reason why there is continuous capacity loss. [37] All the process is shown in the schematic of Figure 2-4.

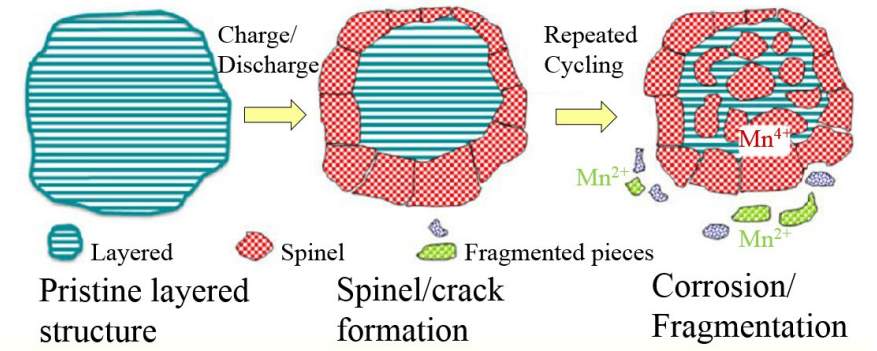

Figure 2-5 The deterioration process of HENMC particles.

2.4. Compositional analysis

There is a variety of ways to acquire compositional data of NMC. In general, Inductively coupled plasma mass spectrometry (ICP-MS) provides an average compositional information from bulk material in the form of powder. When micro-level local information is needed, like for the inside the secondary particles of NMC, scanning electron microscope (SEM) can be used. Both energy dispersive spectroscopy (EDS) and wavelength dispersive spectroscopy (WDS) are based on SEM and used for transition metal elements. In addition, more powerful SEM-based Auger electron spectroscopy (AES) can be used for both Li and all transition metals on the top surface of the sample. Moreover, transmission electron microscope (TEM) is used for further composition of primary particles of NMC.

Most research group operated basic ICP-MS and fast EDS work to get quantitative compositional information. In contrast, this project is more focused on the micro level composition. The more accurate and precise way of doing EDS and WDS is explored. AES is introduced as well since this might be a new and better approach to discover how different atoms are distributed inside individual particle.

2.4.1. Scanning electron microscope

In SEM, an electron beam is swept in a raster-like fashion over the surface of the specimen to form images or to analyze at one spot. From the interaction volume of the electron beam and the specimen, secondary electrons (SE), backscattered electrons (BSE), characteristic X-rays, and Auger electrons etc. are generated and gathered by the detectors to do the examination.

In this project, both SEs and BSEs are used to represent the difference of the surface morphology by images with striking contrast and high depth of field. Characteristic X-rays can yield both qualitative identification and semi-quantitative elemental information. Both EDS and WDS rely on the characteristic X-rays to quantify the materials. In addition, Auger electrons are used to detect the surface composition of NMC.

2.4.2. Energy dispersive spectroscopy and wavelength dispersive spectroscopy in scanning electron microscopy

Using the scanning electron microscope – energy dispersive spectroscopy (SEM-EDS), qualitative and semi-quantitative analysis of specimen can be done by identifying the elements and measuring the intensity of the characteristic peaks from the EDS spectrum as a part of SEM analysis. X-rays escaping from the specimen and passing through the detector, are transformed to electron-hole pairs, charge pulse, and final voltage pulse. After modification and adjustment to remove all the errors caused from the signal acquisition process, the spectrum will be in terms of intensity vs energy to give semi-quantitative results.

Compared with EDS, WDS has advantages of superior energy resolution (by a factor of 10), with high count rate capability (>50,000 counts/s). However, it is more expensive, time-consuming and more difficult to manipulate. X-rays generated from the specimen impinge on the crystal inside the WDS detector. According to Bragg's law, the X-rays are diffracted by some crystallographic planes in the selected crystals and detected. After amplification and transformation, the signal will be then displayed. The qualitative analysis

will be done based on the intensity as a function of the scattered angle. Then each peak position is converted into a wavelength and the corresponding elemental constituents.

Qualitative Analysis

In the EDS qualitative analysis, there is a gold principle for identifying an element: the minimum size of the peak should be at least 3 times of the nearby noise in the background, that is , so that the peak can be considered to belong to some element instead of being random continuum x-ray signals. Also, the electron from a subshell is excited and the atom is ionized, subsequently, all possible transitions involving that shell vacancy will take place, producing a family of x-ray peaks simultaneously.

Practically, the most intense line in high-energy range, which is in the most cases K or L line, is often shown separately from the other peaks, and firstly considered. Then, peaks belonging to the same family can be recognized. After the most intense peaks were identified, the appearance of sum peaks, escape peaks and overlapped peaks are supposed to be considered, as well. After major (>10%) peaks are located, minor (1-10%) peaks and trace (under 1%) elements can be checked as well. When a peak cannot be identified with certainty, collection of more counts can be tried. In addition, WDS can be attempted as well.

Quantitative analysis

After qualitative analysis of the sample, in order to acquire the compositional information of different elements in the specimen, quantitative analysis need to be done. The basic idea of doing quantitative X-ray analysis, is based on “Castaing approximation” which is often used to approximately describe the relationship between the intensity and concentration of both the specimen and the standard.

$$C_{spn} / C_{std} = I_{spn} / I_{std} = k \qquad (2\text{-}1)$$

In which, C is concentration, I is the intensity of the peaks and K is the ratio. Spn means the specimen and std means the standard. The intensity ratio is acquired after the background subtraction and the peak overlaps are also accounted for and is designated by k ratio. Especially in the multi-element composition of specimen and standards, systematic deviations are inevitable such as X-ray absorption and electron back scattering. These

effects, called matrix effects, are supposed to be corrected before it comes to the final k ratio. In all, they are categorized into three groups called "ZAF" factors and the corresponding Castaing approximation becomes:

$$C_{spn} / C_{std} = [ZAF] I_{spn} / I_{std} = [ZAF] k \quad (2\text{-}2)$$

"Z" means atomic number effect. This effect consists of backscatter coefficient and the "stopping power". The backscatter coefficient increases with atomic number, which causes the loss of electrons before they ionize the atom. As a result an X-ray spectrum is obtained. On the other hand, energy loss due to inelastic interaction decreases the power of X-ray. With Z number increases, this effect decreases. Therefore, these two factors tend to cancel each other.

"A" means X-ray absorption effect. In the EDS analysis, many X-rays travel throughout the specimen and are absorbed by electrons. Generally, more absorption will occur when the X-ray energy is slightly higher than the binding energy. In addition, the deeper the X-ray originates, more fractions of those X-rays are lost. The ratio of measured X-rays to the actually generated ones depends on absorption coefficient, specimen density, and path length.

"F" means fluorescence effect. After an atom absorbs the X-ray, it turns into an excited state with subsequent relaxation that emits its own characteristic secondary fluorescence. This effect can be calculated with sufficient accuracy, however, it is the least important among all three ZAF factors.

There are generally two ways of calculating the ZAF factors. The traditional way is to calculate all three factors separately, which is direct but very complicated method since it involves the corresponding physical processes. A new alternative called "phi-rho-z correction" is used. By plotting an ionization $\Phi(\rho z)$ versus mass-depth ρz, the intensity can be displayed by the area under the distribution curve. In this way, the ratio of the unknown specimen and standards are employed to calculate the atomic number factor. Moreover, comparison between the intensity after the absorption and the intensity of the theoretical curve which is calculated according to the physical processes can give the absorption factor.

2.4.3. Energy dispersive spectroscopy using transmission electron microscopy

After the electron beam hit the specimen, generated X-rays are detected by EDS detector and identified. The counts in the energy channels are then displayed by the computer as a spectrum. Similarly with SEM-EDS, prior to quantification, one needs to remove the background and artificial peaks in the X-ray spectrum.

Qualitative analysis

Qualitative analysis requires that every peak in the spectrum must be identified unambiguously. When a spectrum is acquired, one should maximize the X-ray count rate to give a sufficient intensity of the characteristic peaks and minimize the operation time to reduce artifacts.

In order to perform the peak identification, the most intense peak, associated artifacts and overlaps need to be checked, bookkept, and then next most intense peak. The principle that series of peaks coming from the same element have its own peak ratio can also be applied here in TEM-EDS analysis. Even though the automatic identification performed by the computer is very accurate and in most cases trustworthy, certain level of suspicious perspective should be kept. Furthermore, when the peaks are overlapping, deconvolution is applied.

Quantitative analysis

After a spectrum is acquired, the background needs to be removed first. The background refers to the counts under the characteristic peaks in the spectrum displayed, and the same background-removal process must be applied to both the standard and the unknown.

The second step is calculation of the peak intensity. There are some factors taken into account: peak overlapping can be separated by deconvolution; the peak width can change as a function of energy or as a function of count rate; peak distortions due to incomplete charge collection can vary; an absorption edge might show up because of thick sample.

After all, the k factor can be acquired. It is a sensitivity factor that will vary not only with the X-ray detector, the microscope, and the analysis conditions, but also with the choice of background subtraction and peak-integration methods.

2.4.4. Auger electron spectroscopy

As shown in Fig. 2-5, when the electron beam bombards the specimen (step #1), some electrons in the specimen atom gain energy. They leave their energy levels and leave a vacancy behind. This is the ionization step #2. The next step is the relaxation step #3 when another electron from outer shell fill the vacancy. In some cases, shown in Fig. 2-5 (a), after the relaxation, the energy can be released directly in the form of photon, which is detected by the EDS detector; in other ways in Fig. 2-5 (b), the energy will be transferred to the third electron, and that electron will be released in step #4 and it is called Auger electron. Generally, Auger electrons can reveal the compositional information of the top surface few nanometers (2nm to 10nm) with higher accuracy.

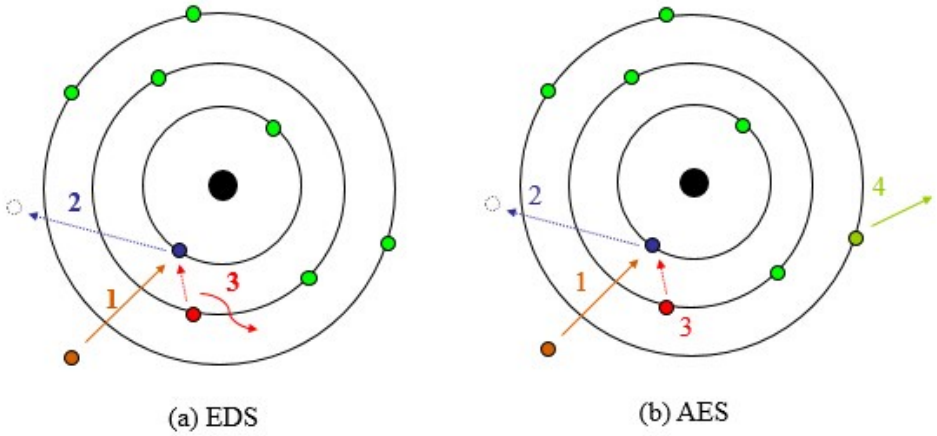

Figure 2-6 Schematic representation of (a) EDS and (b) AES mechanism. In both schematics, the step #1, #2, and #3 are the same: bombardment, ionization and relaxation. While in (b) #4 means the Auger electron emission.

The schematic of SEM with Electrostatic hemispherical analyzer which can separate Auger electrons with different energies and detect them is shown below in Fig. 2-2. Most parts are similar with general SEM instrument. The ultrahigh vacuum need to provide vacuum of better than 5×10^{-8} Pa. The ionization gun of Ar is used for sputtering the contamination caused by carbon deposition or neutralizing the charging on the surface caused by the electron beams on the sample surface.

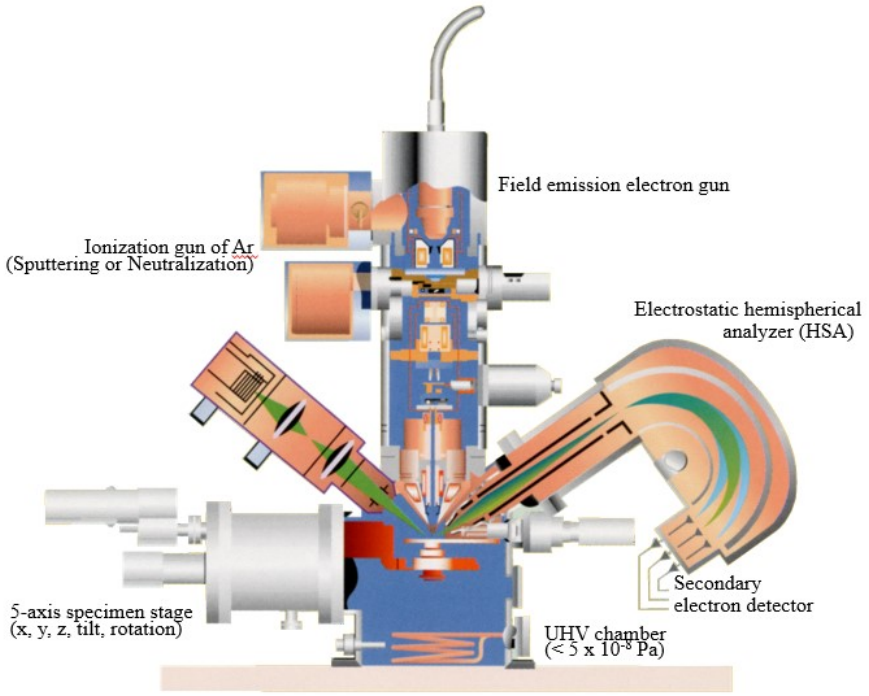

Figure 2-7 Schematic view of JEOL JAMP-9500F instrument from reference[44].

When an Auger electron detector acquires the data, a small energy window with the size of step-size is open and only the Auger electrons that have the same range of the energy are collected during the set dwell time. After the dwell time, the next energy window with higher energy range is open during another dwell time. From electron energy 0 to some certain value, the whole spectrum of collecting electrons is called a sweep. Sweep numbers can be set as well. Every time after a sweep, the value of all peaks will be averaged with all the collected information, so the whole spectrum is actually an average of all the data from many sweeps. Due to some charging or systematic problems, pre-acquisition is recommended before the real acquisition, and corresponding treatment can be done like ion sputtering to remove carbon coating which deteriorate the quantification later.

As shown in Fig. 2-5, when the electron beam bombards the specimen (step #1), some electrons in the specimen atom gain energy. They leave their energy levels and leave a vacancy behind. This is the ionization step #2. The next step is the relaxation step #3 when another electron from outer shell fill the vacancy. In some cases, shown in Fig. 2-5 (a), after the relaxation, the energy can be released directly in the form of photon, which is detected by the EDS detector; in other ways in Fig. 2-5 (b), the energy will be transferred

to the third electron, and that electron will be released in step #4 and it is called Auger electron. Generally, Auger electrons can reveal the compositional information of the top surface few nanometers (2nm to 10nm) with higher accuracy.

Qualitative analysis

Both Auger electron and X-ray are released in most elements after the photon ionization and relaxation. For elements with lower Z, more Auger electrons are observed; while for the higher Z elements, more X-rays can be acquired and EDS might be preferable. The most prominent Auger peaks are KLL transition for elements with Z = 3 to 14 and LMM for Z = 14 to 40 and MNN for heavier elements.

In an original Auger spectrum, plasmon energy losses, ionization losses, Auger peaks and inelastic scattered primary electrons need to be removed. Then the spectrum from the specimen are compared with the standards, the right peak found can be used to do the identification.

Nowadays, Auger instruments are operating in the digital (pulse counting) mode in which the output is the intensity counts per second (N) to kinetic energy (E). Frequently, the derivative spectrum of the direct spectrum is calculated for automatic background subtraction and in this way, the intensity is measured as the Auger peak-to-peak height (APPH). APPH is taken as a measure of the intensity and proportional to the peak area if the peak shape stay stable with intensity.

Quantitative analysis

The quantitation work of AES is done on the intensity of characteristic signal from a measured spectrum. The differentiation of the spectra, which removes the background, is done first. Usually, 9 or 11 point differentiation are used. Overlapping peaks need to be deconvoluted as well and they are treated according to the energy difference and intensity ratio. Then modification of the whole spectrum are to be done by mathematical treatments.

After determining the intensity for all element peaks, in practice, pure standards spectra with appropriate materials and identical instrumental parameters are used for quantification work. Especially those critical factors needs to be the same: beam current and voltage in AES and excitation and emission angle and analyzer settings.

The spectra of the specimen and standards are then compared. By putting different weight of the standards and adding them up, the optimal match with the specimen spectrum is the final goal. The ratio of both intensities is taken as the measure of the mole fraction without consideration of matrix effect and assumption of homogeneous elemental concentrations. Similarly the correction of matrix effects need to be done as well.

The standards composition should be as close as possible to the sample to make it accurate. However, in most cases, it would be easier to get pure element identical standards. When an improved accuracy is required, matrix effects has to be done and elemental relative sensitivity factor have to be corrected to yield matrix relative sensitivity factors.[23]

2.5. Structural analysis

In terms of structural analysis of Li-ion battery cathode material NMC, most of the research is done based on X-ray diffraction (XRD) and neutron diffraction (ND). After Rietveld analysis of either ex-situ or in-situ data acquired from XRD and ND, much structural information such as space group, atoms distribution, lattice parameters, and cations mixing etc. are revealed. Furthermore, micro-level local structural information can be acquired by transmission electron microscopy (TEM) and diffraction patterns (DP). Since most nano-level particles tend to agglomerate and become huge chunk, no electron can travel though large agglomerations. Therefore, isolated particles are used to acquire DPs with the help of Kikuchi pattern as a guide for tilting.

In this project, the DPs from NMC and HENMC are acquired so that comparison can be made by different structure due to different composition. Some LCO, LNO, and LMO DPs are obtained as well to be the standards for further comparison. Moreover, the structures before and after cycling of HENMC are compared to see the effects of charging and discharging.

2.5.1. X-ray diffraction & neutron diffraction

Theoretically, XRD data set lack contrast between coherent transition metal elements Mn Co and Ni, so synchrotron resonant techniques are used to adjust with higher contrast. However, challenges still exist. On the other hand, the neutron scattering lengths of these three elements are distinguishable so that they can be better detected. The ND can also

detect Li which makes this technique ideal for the characterization of lithium transition metal oxides.

Theoretically, XRD data set lack contrast between adjacent transition metal elements Mn, Co and Ni, so synchrotron resonant techniques are used to adjust with higher contrast. However, challenges still exist. On the other hand, the neutron scattering lengths of these three elements are distinguishable so that they can be better detected. The ND can also detect Li which makes this technique ideal for the characterization of lithium transition metal oxides.

Ideally, if the in-situ data of the electrode structure is acquired as a function of electrochemical parameters, the charging-discharging process of the battery can be observed in real time can be investigated and different approaches can be attempted to improve the battery performance. Since the ND can provide more contrast for different transition metal ions, and its sensitive to Li, the in-situ ND is widely used.[17] Later on, the acquired data from either XRD or ND can be analyzed by Rietveld refinement.[2]

2.5.2. The Transmission Electron Microscope

In an electron microscope, an accelerating voltage is applied to the electron beam in high vacuum. After passing through a series of electromagnetic lens, the electron beam will penetrate the specimen, transmit it or be diffracted by it. Then after the magnification system, an image or a diffraction pattern (DP) can be displayed on the fluorescent screen. The image contrast can be enhanced by using an objective lens and the diffraction areas can be selected by using different selected area apertures.

In this project, basic TEM images are acquired to do the comparison with SEM images showing how nano-level particles are connected to form secondary micro-level clusters. Moreover, DPs are used to check the local structural information of NMC as well. In this way, the data can be compared with average structural data from XRD or ND so that a clearer picture of the structure of NMC can be displayed.

2.5.3. Electron Diffraction Pattern

The whole diffraction process can be conveniently visualized as reflection by (hkl) crystal planes with spacing d_{hkl}. The diffracted beam corresponds to reflection for a

particular angle θ between the incident beam and the crystal plane for which $n\lambda=2d\sin\theta$. This law is known as the Bragg's law and corresponds to satisfaction of the Laue conditions. Each spot in reciprocal lattice represent a particular (hkl) plane, $|g|=1/d_{hkl}$, from the origin in a direction perpendicular to the individual (hkl) plane. The incident electron beam B is diffracted by the specimen and can construct an Ewald sphere. When the Ewald sphere cuts a reciprocal lattice spot, a diffraction point is formed, shown in Fig. 2-2. In a single crystal, because of the relaxation of the Laue conditions reciprocal lattice points are streaked perpendicular to the specimen surface. In addition, the intensity of a particular DP spot depends on (a) the position and identity of the atoms in the unit cell through the structure factor F, (b) the size and shape of the crystal through the Laue condition, the (c) the deviation s from the exact Bragg reflection position to the central spot of the streaked reciprocal lattice.

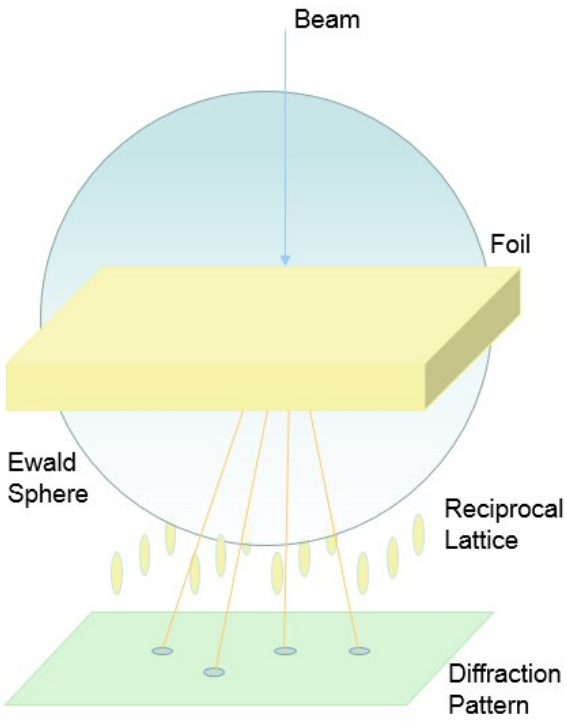

Figure 2-8 Illustration of how electron diffraction pattern is formed.[45]

Electron diffraction patterns formed in TEM can be divided into three different types: ring pattern produced by polycrystalline specimen; or the single-crystal region of the

sample, which can form “selected area” diffraction pattern that consists of spot pattern or Kikuchi line pattern.

i) Ring Pattern

In most cases, the ring patterns are used for identification of different phases and they are from very fine grain size polycrystalline materials. Basically, a series of concentric rings will be produced and each concentric ring corresponds to a particular set of (hkl) reflection.

ii) Spot Pattern

Spot patterns are taken through reciprocal lattice, of which the plane is normal to the incident beam direction B. By using the spot patterns, the specimen orientation can be determined. In turn, orientations between planes can be identified too. Moreover, details of the fine structures like precipitates and twins can be found in samples as well.

iii) Kikuchi Pattern

If a SADP is taken from a single crystal region of the specimen and the specimen is reasonably thick and has a low defect density, the Kikuchi patterns which consist of pairs of parallel bright and dark lines will occur.

There are some advantages in using Kikuchi patterns. By tilting the sample, more accurate determination can be made comparing to the spot patterns. The zone axis can be found according to Kikuchi pattern. Moreover, the sign and magnitude of the deviation s can be determined.

The electrons undergo both the elastic scattering and inelastic scattering. When the electrons are elastically scattered by the specimen, the Kikuchi lines appear. However, those inelastically scattered electrons are present in most spot electron diffraction patterns as a diffuse halo around the transmitted and strong diffracted spot and as an overall faint background intensity.

Indexing diffraction patterns

Ring patterns [in Figure 2-9 a)] are mostly used for polycrystalline specimens to help calibrate the camera lengths or identify precipitates. Most information can be acquired by

calculating the radii of each ring that reflects different planes in the crystal and magnification of the TEM lenses setting.

Both Kikuchi and spot patterns can provide accurate enough information in NMC powder analysis. However, due to the CCD camera quality and the structure characteristic of NMC particles, the spot patterns can give clearer and measurable data represented in Figure 2-9 c) instead of the blurring patterns that are shown in Figure 2-9 b). Therefore, the description below is focused on the spot patterns.

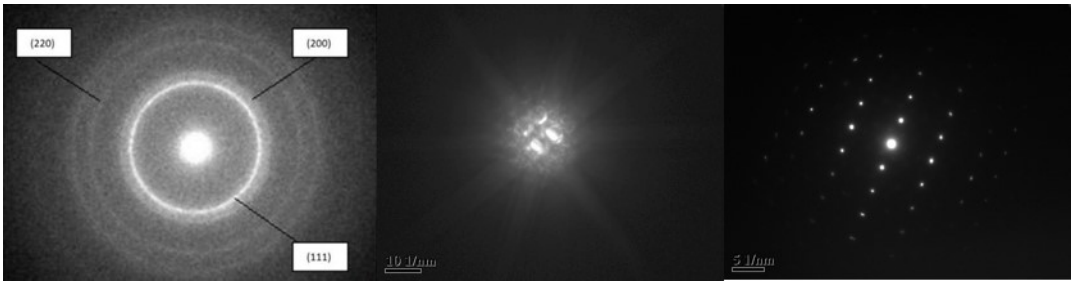

a) b) c)

Figure 2-9 Assorted diffraction patterns: (a) Ring patterns; (b) Kikuchi patterns; (c) Spot patterns.

Before performing the indexation, the sample is usually tilted using the Kikuchi lines as a mark. When the intersection of the Kikuchi lines goes to the center of the viewing screen, it means that the incident electron beam direction B is along one of the zone axis. In this case, the spot patterns are with high symmetry. Finally, the pattern is easy to index without other procedures.

There are two features utilized to index the DP: the distance between the transmitted spot and the diffracted spot, and the angles between the lines of center spots and different diffracted spots. The distance directly connects with the inter-planar spacing and the angle is the same with the angle between the zone axis and the plane normal.

The Figure 2.9 displays the relationship between DP and reflecting planes. It is obvious that the incident beam direction B and the zone axis of reflecting planes are parallel, so B is approximately considered as the zone axis of the reflecting planes. Since one spot in the DP means a series of parallel planes (hkl), the direction R in DP which is from the center

spot to the diffracted spot is almost equal the reflection plane normal, called $\mathbf{g}_{hkl}$. In addition, it is used to represent the crystallographic directions.

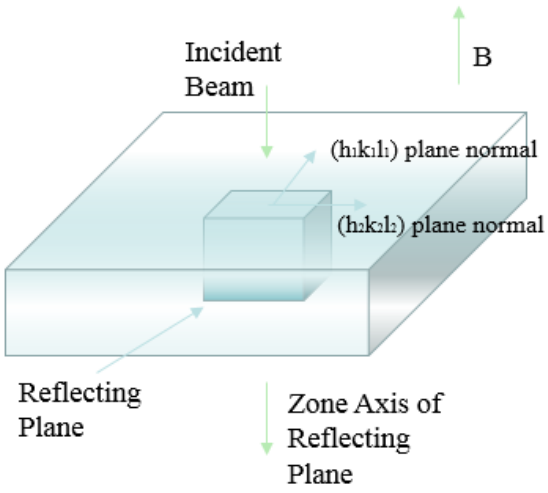

Figure 2-10 Relationship between incident beam and reflecting planes.[45]

When B is very close to a zone axis, all the diffraction spots are almost of uniform intensity. When deviation of lattice points s = 0, then intensity of the spots is in the maximum. For the same B, the same order spots should have the same intensity. The calculated B is actually an average over the region selected by the diffraction aperture. However, when the specimen is/or has a high defect density, the Kikuchi lines become diffuse. Consequently, for materials that have been deformed or undergone phase transformation, Kikuchi line analysis is not applicable.

Ch 3. Experimental method

3.1. Compositional analysis

In most Li-ion battery cathode material analysis, compositional information is partially ignored. However, the content and distribution of elements, for example, Mn, Co and Ni inside the $LiNi_xMn_yCo_{1-x-y}O_2$ cathode significantly influence the stability, crystallinity, conductivity and all other electrochemical properties in cycling. In addition, high-energy Li-ion battery material ($Li_{1.2}Mn_{0.54}Co_{0.13}Ni_{0.13}O_2$) with higher concentration of Li shows completely different electrochemical features comparing to normal NMC ($LiMn_{0.33}Co_{0.33}Ni_{0.33}O_2$). However, since the composition claimed above are all calculated based on the synthesis procedures (i.e. quantities of raw material used), more accurate composition are necessary as there are possibly local variations in composition and even secondary phases that cannot be ignored. In other terms, the composition at the micro-scale or even nano-scale in a local area might be different than the average composition and the distribution of composition might not be homogeneous. Therefore, local composition measurements enable us to understand and improve the performance of batteries.

The first step in our work is therefore to measure the composition in bulk NMC powders, using inductively coupled plasma mass spectrometry (ICP-MS). Local compositional data was then collected using SEM based EDS, and AES at the finer scale to understand local fluctuations. Moreover, for smaller particles, in the range 10-100 nm in size, TEM-EDS was utilized to show more details in nano-meter level.

3.1.1. Inductively coupled plasma mass spectrometry

ICP-MS is a mass spectrometry-based method that is capable of detecting material's composition. By ionizing the sample with inductively coupled plasma and using a mass spectrometer to separate ions, quantification results of composition can be achieved.

An Agilent 750cx ICP-MS was used for $LiMn_{0.33+x}Co_{0.33+y}Ni_{0.33-x-y}O_2$ powder and with all standards for Li, Mn, Ni, Co. However, there was a lack of O standard in this project. One step further, based on valence and charge neutrality, the O content was assumed to be 50% so that comparison between other elements can be done.

3.1.2. Scanning electron microscopy

The JEOL JSM-7000 SEM was used to characterize the morphology of the NMC particles, the ball milled NMC particles, the NMC cathode and ball milled NMC cathode as well. For the secondary electron image, 5.0kV was adequate for NMC since this material will cause charging with high accelerating voltage. The working distance was set to be around 10mm.

3.1.3. Energy dispersive spectroscopy

Sample Preparation

A necessary requirement for quantification with EDS in the scanning electron microscope is that the sample needs to be as flat as possible to ensure that the absorption correction is accurate. More specifically, under the optical microscope, no obvious huge scratches or big holes are to be found. We used three approaches to make sure the sample surface is flat enough.

i) Cross-Sectional Polishing

In order to explore the internal composition of the secondary NMC particles with SEM-EDS, cross-section of NMC particles needed to be prepared. This can be done with a broad ion beam bombarding the powder that is embedded in the matrix. Firstly, one surface of the carbon block used as a powder matrix was pre-polished by sand paper (Fig. 3-1 a). This would ensure precise alignment between the ion gun and the pre-polished surface once the carbon block is placed inside the cross-sectional polisher. Moreover, the top surface should be perpendicular to the pre-polished surface because the angle between these two surfaces would strongly affect the ion gun alignment. Then a blade was used to make a scratch on the top edge of the pre-polished surface to hold the particles (Fig. 3-1 b). The top edge scratching is important since the cross-sectional polishing could only be applied in a shallow area and the NMC particles were put on the top to assure they are cross-section polished. The carbon paste and NMC powder were mixed, followed by the addition of acetone to dilute the solid carbon paste-NMC mixture. The mixture was dropped on the scratched surface allowing the mixture to embed inside the scratch after acetone evaporation (Fig. 3-1 c). In the cross-sectional polishing process, the carbon block was fixed and aligned with the ion gun inside the chamber of cross-sectional polisher. Under 5

kV and after 3 to 4 hours polishing, the first ion-beam bombardment was done (Fig. 3-1 d). Below is the image taken from a cross-sectional polished area of the NMC particles embedded in the Carbon block matrix (Fig. 3-1 e).

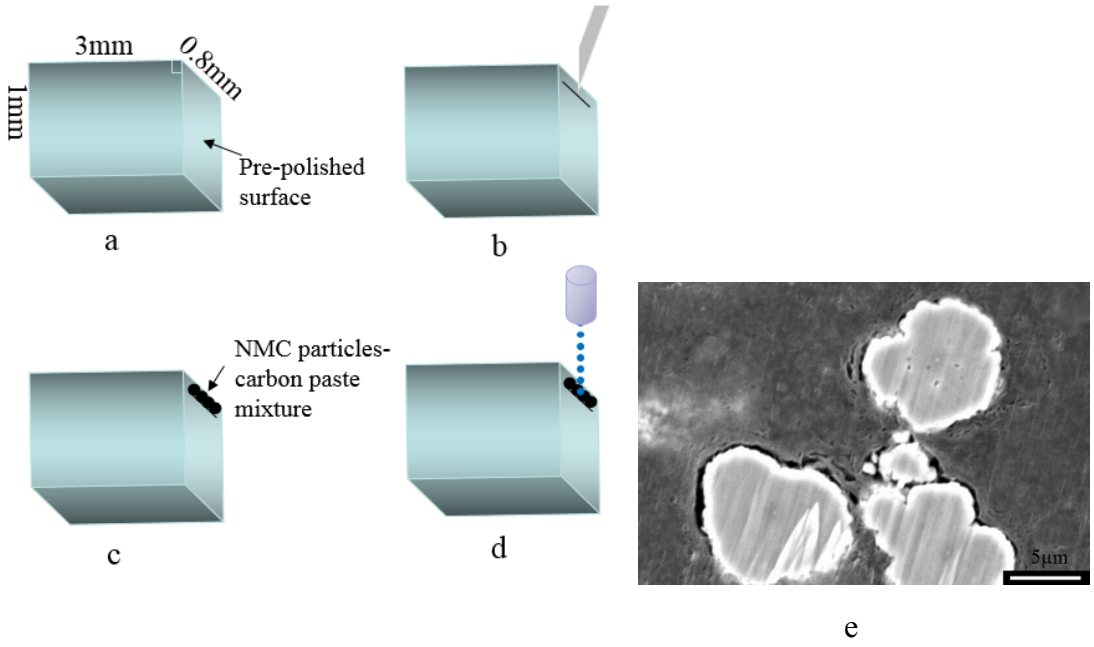

Figure 3-1 a) – d) The procedures of cross-sectional polishing; e) The SEI of cross-sectional polished NMC particles embedded in the carbon block.

ii) Mechanical polishing

The alternative of creating an internal flat surface of NMC particles surface is by mechanical polishing of NMC particles embedded in the epoxy matrix. The fabrication of epoxy was the first step. 15mL resin and 5 mL hardener were mixed slowly and gently, to avoid too many bubbles. On the lid of the mold, plastic clips were used to form a small hollow cylinder to load specimen powder (Fig. 3-2 a). After that the mold was assembled and the mixture was poured in (Fig. 3-2 b). Then all the air in the liquid or sample was pumped away, since the bubbles would hinder the microscope work. The pumping procedure needed to be done a couple of times to assure no visible bubbles are present. After 8 hours, the solidified epoxy was ready for polishing. The automatic mechanical polishing machine could be used. Procedures of using various polishing cloth, lubricants and polishing time needed to be balanced well (Fig. 3-2 c). All the conditions for the mechanical polishing are listed in Table 3-1 below.

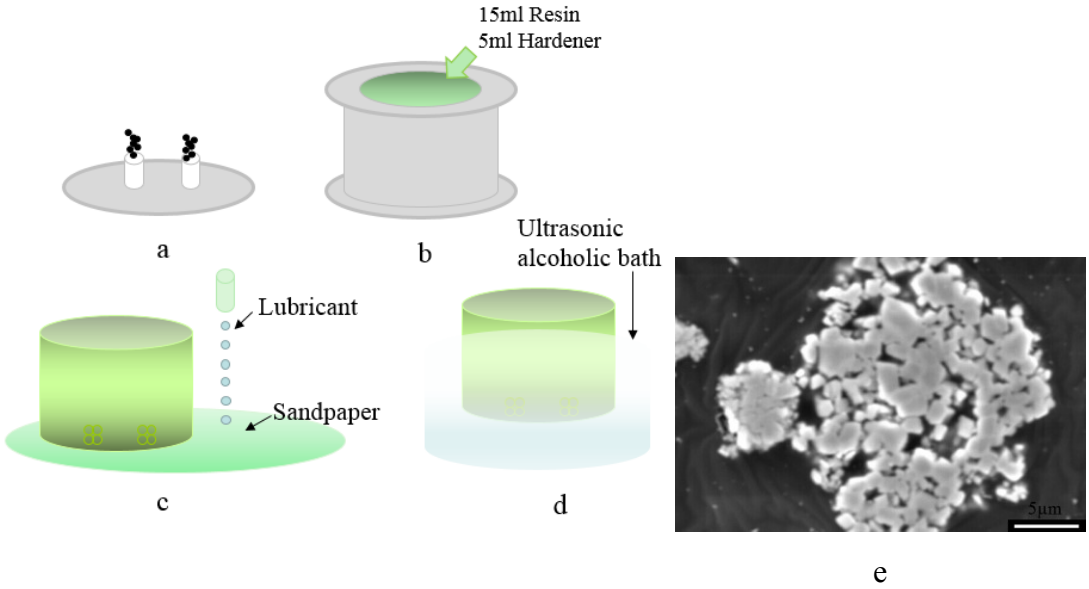

Figure 3-2 a) – d) The procedures of mechanical polishing; e) The SEI of mechanical polished NMC particles embedded in the epoxy matrix.

Table 3-1 List of different mechanical polishing parameters.

Polishing cloth	Lubricant particle size (nm)	Lubricant	Load (N/sample)	Time (min)
MD-MOL	3000	Blue lubricant	15	5
MD-DAC	3000	Blue lubricant	15	5
MD-NAP	1000	Blue lubricant	20	5
MD-CHEM	50	Colloidal silica OPS	20	7

As a final step, samples needed to be washed by alcohol and ultrasonic treatment to get rid of all the residual silica from the lubricant (Fig. 3-2 d). If too many scratches or residual silica were observed by optical microscope, the last step of polishing would be redone). Figure 3-2 e shows an image taken from a mechanical polished area of the NMC particles embedded in the epoxy matrix.

iii) Pellets

The third way to create a flat surface of the sample was to make the sample pellets. Basically, pressure was needed to press the NMC small particles into a pellet with diameter of 3 mm (Fig. 3-3 c). However, before that, grinding was important because the particles

were supposed to be small enough in order to form a compact pellet (Fig. 3-3 a). After grinding, the refined powder was put in the small hole inside the holder and use the dice with proper size and high pressure to create a flat surface. After it was done, an optical microscope check was needed to make sure that there was not too much contamination from the dice or during the grinding (Fig. 3-3 b). The image taken from a pellet made of NMC particles is shown in Fig. 3-3 d.

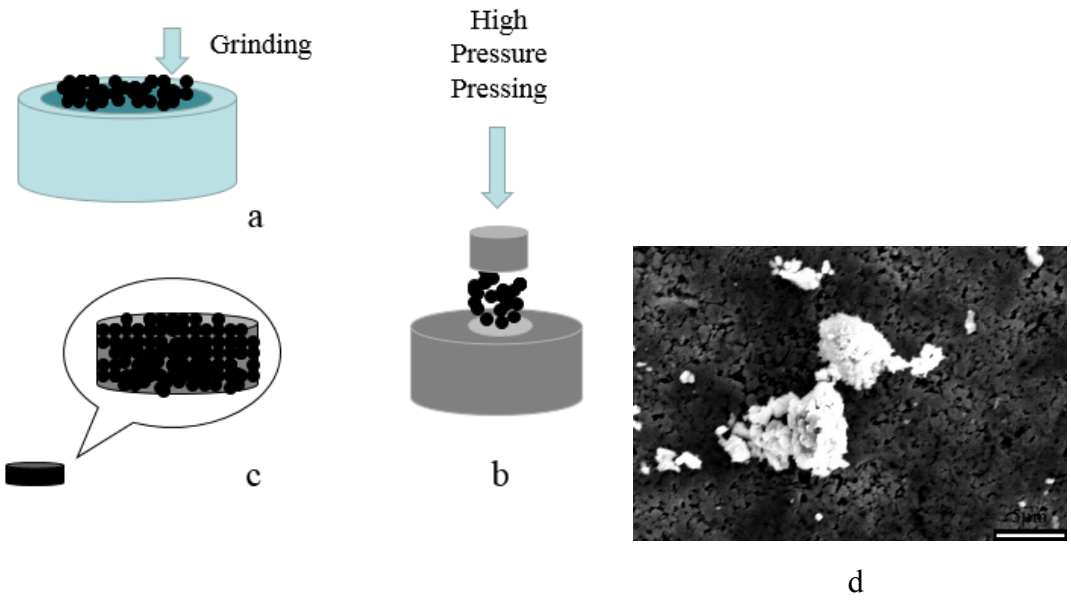

Figure 3-3 a) – c) The procedures of pellets fabrication. d) The SEI of pellet consisting of NMC particles.

Scanning Electron Microscope - Energy Dispersive Spectroscopy

For the EDS analysis, the JEOL 6610LV SEM with the Oxford EDS Silicon Drift detector in energy range from 0.2-12keV was used. The accelerating voltage was set to be 15kV since this is the optimal value necessary for the ZAF factors calculation. The working distance was 14mm as the SEM characterization. The beam current was around 30nA.

The area of interest for quantification must be chosen so that all the criteria for quantification are met: 1) flat surface, 2) particle of NMC large enough that the interaction volume of electrons is contained within the particle. In addition there should not be large holes within the analyzed volume or too many scratches on the polished surface. Then

secondary electron images were acquired by SEM so that morphology of the particles were observed. The INCA EDS analysis system, from Oxford instruments, was used to do EDS qualitative and semi-quantitative analysis. This software was used first to capture a backscattered image which shows some compositional information based on the image contrast. Later, different areas were chosen in the area of interest and spectra were acquired.

The EDS quantification was then carried out. For this, homogeneous standards were needed for all the elements to be quantified. For both the NMC specimen and the standard samples, the surface had to be flat enough that all scratches are smaller than 0.1μm. Then the spectra from both the specimen and standards were acquired in the same conditions: dead time, take-off angle, calibration of the spectra, energy resolution, beam energy, and current. The noise suppression and background subtraction were done automatically within the INCA software using filtering functions. After this, peak deconvolution was carried out since the separation of peaks was limited by the energy resolution of the EDS detector. The X-ray signal intensity was calculated by comparing the specimen and standard intensity. According to the first approximation, the measured peak ratio should be equivalent to the ratio of weight fractions. $I_i/I_{(i)} = C_i/C_{(i)} = k$. However, this is not the case due to the existence of the matrix effects. Therefore, at the last step, the ZAF calculation was done to acquire more accurate and real quantitative concentration values. $C_i/C_{(i)} = I_i/I_{(i)}\ [ZAF]_i = k\ [ZAF]_i$. In standardless quantitative analysis, the standards measurements were performed by the manufacturer on a number of fixed reference samples and adjusted for the characteristics of local instrument.

In order to decide when to use customized standards, as compared to the standardless method, there is a rule of thumb: adequate accuracy with relative errors less than 2%; elements whose X-ray lines are in the low energy region of the spectrum are quantified; the matrix corrections are high such as in the case of light element in heavy matrix or vice-versa, where the intensity correction is >1.25 or <0.8. Different weights are put in the standards spectra and then they are added up to compare with the sample spectrum. The intensity correction represents the ratio between the fitted spectrum and acquired spectrum. So in the case of NMC, standardization was necessary and required.

Two sets of the standards were chosen, one set was $LiMn_2O_4$, $LiCoO_2$, $LiNiO_2$, and the second was MnO_2, Co_3O_4, NiO. They were chosen because they had similar composition with the NMC samples which therefore helped reduce the ZAF factors. However, there were still some issues that make these standards imperfect. In particular, for the triple-element standards, the valence was not the same as for the NMC material. In NMC, the valence of Ni is 2+ and Mn is 4+, however, in $LiNiO_2$ the valence of Ni is 3+, and in $LiMn_2O_4$ Mn is either 3+ or 4+. While in the metal-oxide standards, the Co_2O_3 was not pure enough to be a standard, so the Co_3O_4 was used instead and in this case, the Co valence was mixed of 3+ or 4+.

In terms of the standards' chemical composition ($LiMn_2O_4$, $LiCoO_2$, $LiNiO_2$; MnO_2, Co_3O_4, NiO), they were all purchased from Sigma Aldrich and the purities of all standards are all higher than 97%. No obvious impurities were found in most standards so the results are consistent and trustable.

The same requirements were needed for the measurements of the standards: flat uniform samples. We thus used two methods to prepare the standards: mechanical polishing and the dense pellets approach by using the same preparation procedures as the NMC samples. In the case of epoxy embedding, four plastic clips were placed inside the mold so that the standards and the specimen were embedded in the same epoxy and can be analyzed in very similar conditions one immediately after the other. As for the pellets, a large stub was used to hold four smaller stubs, of which each had one pellet on top so that three required standards and the NMC specimen were in the SEM chamber together. In this way, all standards and sample could be analyzed under the same conditions and unnecessary variables (such as tilt, take off angle, energy, current) were kept constant. All the standardization methods are listed below in Fig. 3-4.

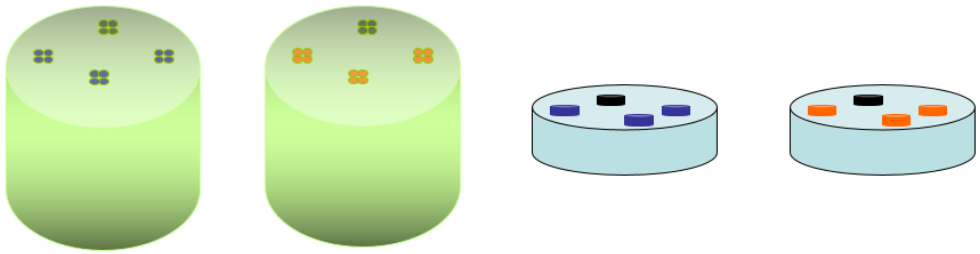

NMC +$LiMn_2O_4$ +$LiCoO_2$ +$LiNiO_2$ a)

NMC +MnO_2 +Co_3O_4 +NiO b)

NMC +$LiMn_2O_4$ +$LiCoO_2$ +$LiNiO_2$ c)

NMC +MnO_2 +Co_3O_4 +NiO d)

Figure 3-4 Four different standardization approaches by using two sets of standards with two preparation methods. Both in a) and b), mechanical polishing method is applied, while in c) and d), pellets preparation method is used. In addition, a), c) and b), d) are using $LiMn_2O_4$, $LiCoO_2$, $LiNiO_2$ and MnO_2, Co_3O_4, NiO as standards sets respectively.

The spectra of the standards were collected and the pure element intensities were converted into concentration based on the weight fraction of elements in these three standards. The pure element intensities were then saved in a data base for use in quantitative measurements of the unknown samples.

Below is the flow chart of Fig. 3-5.

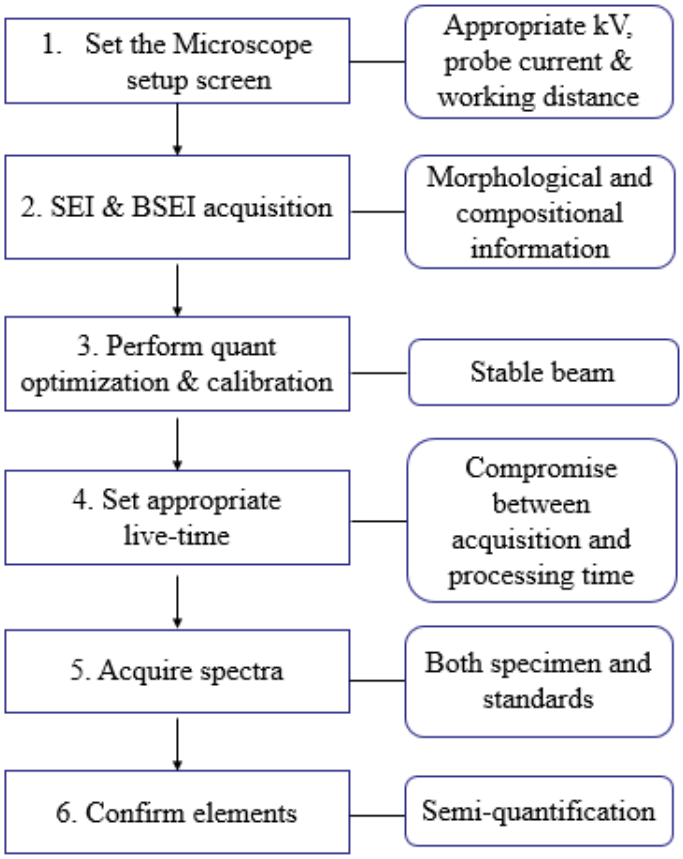

Figure 3-5 Flow chart of SEM-EDS.

Transmission Electron Microscope - Energy Dispersive Spectroscopy

The JEOL 2010F TEM was used for the TEM-EDS acquisition. The accelerating voltage was fixed at 200kV, and the STEM mode was used because a small beam (approximately 1nm in diameter) was necessary to probe the composition within even smaller regions within the NMC particles.

Samples were prepared using the holey carbon grid as support of the NMC material. A suspension of NMC powder ground with a mortar and pestle in methanol was produced and dispersed in an ultrasonic bath. Then the pipette was used to deposit one or two drops of the suspension on the grid and was left until under an incandescent light bulb to dry.

The same INCA system was used for the acquisition of the spectrum, data analysis and final semi-quantification.

3.1.4. Auger electron spectroscopy

The experiments were carried out using a JEOL JAMP-9500F, field emission Auger microprobe based on an ultrahigh vacuum SEM. After the sample and standards preparation (produced in the same way as for the EDS quantification), the acquisition were performed. The step-size of detection, accelerating voltage were tested and set later by the experiments. In terms of other factors, the dwell time was set around 100ms, and there was about 6 sweeps for each range scanned. The working distance was fixed to around 23mm, and tilting angle was kept around 30º. The current affects the counts, and the higher the current is, the more counts it can collect and the more accurate the results can be represented. However, higher beam current means the beam has larger diameter. In this way, the beam cannot be focused on a small interaction area so that the spatial resolution is reduced. Therefore, the optimal current is tested. Both the specimens and standards were analyzed with the same conditions providing more accurate and precise results.

The sample preparations were done in the same way with SEM-EDS by cross-section polishing and the pellets fabrication. Specifically, the Auger electrons can only be detected from the top surface (2-10 nm depending on the energy). Therefore, if there is any surface contamination from hydrocarbons, from exposure to air or prior work in the SEM, this carbon contamination must be removed and exposure to air must be reduced. Therefore, in this experiment, the sample prepared right after cross-sectional polishing and the pellets were put in the high vacuum Auger chamber to reduce the contamination. Moreover, since epoxy could not be inserted into the high-vacuum chamber the mechanically polished/embedded samples could not be used.

The manufacturer's preselected standards were not well matched with the NMC powder and the conditions provided in this machine, the spectral energy range, the level of noise in the reference spectra, and the different acquisition condition (mode, current or tilting angle). Therefore customized standards were prepared, using the same microscope and experiment conditions. In this way, less systematic problems are expected. The most problematic standard was for Li. Different approaches were used to get standard spectra for Li: 1) using a pure Li foil produced by scratching away the oxidized surface prior to insertion in the microscope, 2) using Li_2O pellets prepared in a vacuum chamber. In terms

of the transition metals, we used the pellet standards that were used in EDS quantification, since this was the only way with only pure sample powders. Two sets of pellets were used: $LiMn_2O_4$, $LiCoO_2$, $LiNiO_2$; and MnO_2, Co_3O_4, NiO.

The first step was to acquire spectra from the area of interest, which is also supposed to be from flat surfaces of the particles and from an area with less interstitials or smaller particles. After a secondary electron image was obtained, the areas of interest that satisfy the requirements were selected. In order to avoid electron beam damage during the long acquisition times, the image was defocused so as to spread the electron beam onto a larger area. Parameters such as step size, dwell time, tilting angle and acquisition mode were set up so that no charging could occur. Before the acquisition of all spectra, pre-acquisition was needed to check the carbon deposition. If there were too much carbon, then ion sputtering needed to be done. However, this should be avoided since this generates the sputtering of Li as well which deteriorated the whole surface of the sample. Moreover, the tilting of the sample or the charge neutralization were needed sometimes to prevent too much charging on the surface. Neutralization were done by bombarding the sample softly by using positive ions just to neutralize the extra charging on the surface. When the spectra were acquired, spectrum splitting was used to save time and provided for the convenience of the quantification later. In the case of NMC, only 10-120 eV, including all Li peaks and transition metal peaks, and 440-880 eV including all main peaks of transition were used. In addition, carbon peaks were acquired too to assure the carbon concentration was low enough.

In all, the composition of NMC was checked during which the optimal conditions of the AES quantification were found. Then, the same approach were used to quantify and compare the NMC particles compositions before and after ball-milling, before and after electrolyte submerging. Moreover, the changes in composition on 1, 50, 100 cycles of high energy NMC ($Li_{1.2}Mn_{0.54}Co_{0.13}Ni_{0.13}O_2$) were compared as well.

3.2. Structural analysis

Most of the research related to the structure of NMC has been based on the in-situ and ex-situ experiments using X-ray Diffraction (XRD) and Neutron Diffraction (ND) techniques. Both techniques provide information for the bulk cathode materials, such as

the lattice parameters change, phase transformation during charging and discharging and reversibility of cathode material. More specifically, the question on the structural development during the charging and discharging in a local area, specifically inside a small primary NMC particle was unsolved. For example, there is no long-range superlattice found in NMC however, short-range superlattice needs to be checked. Moreover, some defects in the NMC powders generated from the synthesis process or during cycling are of interest as well.

First of all, XRD detection was done to show that what the bulk structure was like in the 333 compound. Then local structural information was acquired by TEM based ED. Electron diffraction pattern were found in some certain zone axes with the assistance of Kikuchi lines. However, since the NMC powders with all various compositions tended to agglomerate together to form a cluster, only isolated particles or the edge parts of the clusters were used. Moreover, since the NMC particles were beam sensitive, this generated some difficulties of the experiment.

3.2.1. X-ray Diffraction

The Rigaku Cu rotating generator was firstly used for XRD detection. The machine has parallel focusing mirrors, a three-circle Bruker D8 diffractometer and a SMART6000 CCD detector.

Then the high resolution Bruker D8 Advance Powder diffractometer with a Ge monochromator was used. This instrument is capable of performing high resolution structure studies on NMC.

X-ray diffraction data were obtained over the range of 10-100° 2θ. Especially in the second machine, step size was as 0.04° first and then 0.02°, in order to give accurate enough peaks' position and shape.

3.2.2. Transmission Electron Microscope

By using JEOL 2010F and Philips CM12, after all the alignment and correction of astigmatism, both machines were used for the acquisition of TEM images. The accelerating voltage was fixed at 200kV and 120kV, respectively. Sample preparation was exactly the same with the one mentioned above for EDS-TEM.

3.2.3. Electron Diffraction

Battery Preparation

The first step was the cathode preparation. The conductive carbon and the cathode material NMC were ground and mixed by the ratio of 1:8. The mixture was baked in the oven for an hour. Then polyvinylidene fluoride (PVDF) was added to the mixture as the binder by the ratio of 1:1 with NMC. The mixture was stirred with stirring bar overnight and was put in the oven connecting to a container which is cooled down by liquid nitrogen. This step was to get rid of N-methyl-2-pyrrolidone (NMP) solution and collect it in the container. The next day, the Al foil used as current collector was put on a flat glass and the mixture slurry was pasted onto the Al foil and then dried in a vacuum oven.

After the cathode sheet was ready, the whole battery batch was fabricated. For the anode, Li metal foil was used. After scraping the surface oxidized Li, the Li metal foil was rolled to be flat. A small circle of cathode was punched and put in a current collector. The electrolyte LiPF6 was dropped on top of the cathode to rinse it. The separator was added on top of the cathode and O-ring as well to separate the electrodes and seal the battery. Both the anode and spacer were put on top of the separator, and after that, spring was put on top as well. The whole battery was pressed by the presser after all.

Then, the NMC cycling was between 2.5 and 4.6V at a rate of C/10. Meanwhile the HENMC was between 2.0 and 4.6V at a rate of C/10.

Electron Diffraction Pattern

The TEM needed to be adjusted and calibrated well with proper alignment and astigmatism. Then isolated particles needed to be found since it was easier to tilt to the zone axis. Since most of NMC particles tended to agglomerate, search of isolated particles was very time-consuming. Then the double-tilt holder was tilted so that the intersection point of most Kikuchi lines in that local area was moved to the central point of the screen. When the intersection center was in the middle of the screen, the sample was in one zone axis and the diffraction pattern was taken. The selected-area aperture was in and intensity was adjusted to make the pattern dim. Exposure time was set up and the diffraction pattern image was taken.

The structure of NMC particles was first checked. Differences between NMC particles' structure and reference materials LMO, LCO and LNO were compared. Then detailed analysis of the pristine samples and those after 1, 50 electrochemical charging/discharging cycles of high energy NMC ($Li_{1.2}Mn_{0.54}Co_{0.13}Ni_{0.13}O_2$) and on original, 1, 10, 20, 50 cycles of "regular" NMC ($LiMn_{0.33}Co_{0.33}Ni_{0.33}O_2$) were studied as well.

There are actually two ways to analyze the diffraction pattern. The first method was by directly calculation of the zone axes. This can be done within the Digital Micrograph software after suitable calibration, using the equation $Rd = L\lambda$, since L was the camera length which was given by the microscope. The camera length describes the magnification of the diffraction pattern. λ is the wavelength of the electron beam. R, the distance between the transmitted to the diffracted spot, could be measured. So the d spacing could be calculated. By applying the cif file from the ICSD (Inorganic Crystal Structure Database) to Mercury (a software for the analysis of XRD dataset), the corresponding relationship between d-spacing and $[h_1k_1l_1]$ value was found. The procedures was repeated to find the R in another direction to find another $[h_2k_2l_2]$. By using cross product of both vector, $[h_1k_1l_1]$ and $[h_2k_2l_2]$, the zone axis was determined. Since the phases in different compounds are different, below is the Table 3-2 for all of them. The high energy NMC ($Li_{1.2}Mn_{0.54}Co_{0.13}Ni_{0.13}O_2$) cif. file was made using the JEMS software to simulate it.

Table 3-2 Phases used in the compounds analyzed by the electron diffraction.

Compound	Space groups
$LiCoO_2$	R-3m, Fd-3m
$LiNiO_2$	R-3m
$LiMn_2O_4$	Fd-3m
$LiMn_{0.33}Co_{0.33}Ni_{0.33}O_2$	R-3m, P-3m1
$Li_{1.2}Mn_{0.54}Co_{0.13}Ni_{0.13}O_2$	R-3m, P-3m1; C2/m, Fd-3m

The second way was by comparing the simulated diffraction pattern and the real pattern. From the transmitting spot in the pattern to different diffracted spots, there are some vectors formed. The ratio of the different lengths between vectors and the angle between the vector of transmitted spot and diffracted spots of simulated diffraction were compared. The fastest

way was by overlapping simulated pattern and real pattern to check if they overlap well. Firstly, the simulated pattern was established. Using *JEMS*, directly cif file was imported and the simulation was done. In HENMC, a new cif file was established by imputing some structural parameters such as the space group, all the elements, and their related Wyckoff number, their atomic coordination and occupancy. After the simulation, the similar DP with certain zone axis was found, and the real DP was put under the simulated DP. The camera length, angle of the DP was changed to fit better the real DP. Finally, the DP was indexed according to the simulated DP.

Ch 4. Results & Discussion

4.1. Compositional analysis of NMC

4.1.1. Quantification methodology

4.1.1.1. Bulk material compositional analysis

The Inductively Coupled Plasma Mass Spectrometry (ICP-MS) is useful to give a general idea of the elemental composition in bulk materials, such as $LiMn_{0.33}Ni_{0.33}Co_{0.33}O_2$ (labeled hereafter as "333" compound) powder. In this powder there are a total of five elements: Li, Ni, Mn, Co and O. Due to the lack of reference material of oxygen, no absolute value of the oxygen could be obtained from this method. Thus, weight and atomic ratio between any other two elements was compared.

If all five elements are homogenously distributed inside the particles, then the expected atomic fractions should be Li: Mn: Co: Ni: O = 25.0%: 8.3%: 8.3%: 8.3%: 50% due to the given nominal formula of $LiMn_{0.33}Ni_{0.33}Co_{0.33}O_2$. However, since the oxygen reference was not available, O was assumed to be 50.0% because of charge neutrality. From ICP, the atomic percentage of Li was then found to be approximately 24.5±0.4%, and in terms of transition metals Mn: Co: Ni was 8.2±1.0%: 8.7±0.6%: 8.4±1.2%. Therefore, the composition of the results was consistent with the expected theoretical composition shown in the formula unit.

Although ICP-MS suggests the above atomic ratios and percentages of the bulk material, one of the objectives of this project is to explore if there is a local variation of composition between different particles. Since different transition metals have their own function during charging-discharging cycle, as mentioned in the introduction, the distribution of all three transition metals might affect the crystalline structure of NMC, and thus could affect the electrochemical performance of the battery. Similarly, the Li distribution inside the NMC particle could also affect the Li ion insertion and extraction. Both in pristine and high energy NMC, the distribution of Li ions can play a very critical role in the battery performance.

4.1.1.2. Micro-scale material compositional analysis: SEM-EDS

Morphology Characterization

The basic morphology and size information of cathode material of 333 compound are shown in Fig. 4-1. There are large spherical particles identified as “secondary particles” present in this material which consist of agglomeration of smaller “primary particles”. The size of most secondary particles is in the range of 8-12 μm in diameter and the size of the smallest primary particles is less than 500 nm. Some residues of the dried solvent, used for dispersion of the powder, is visible between secondary particles, which was from the carbon tape.

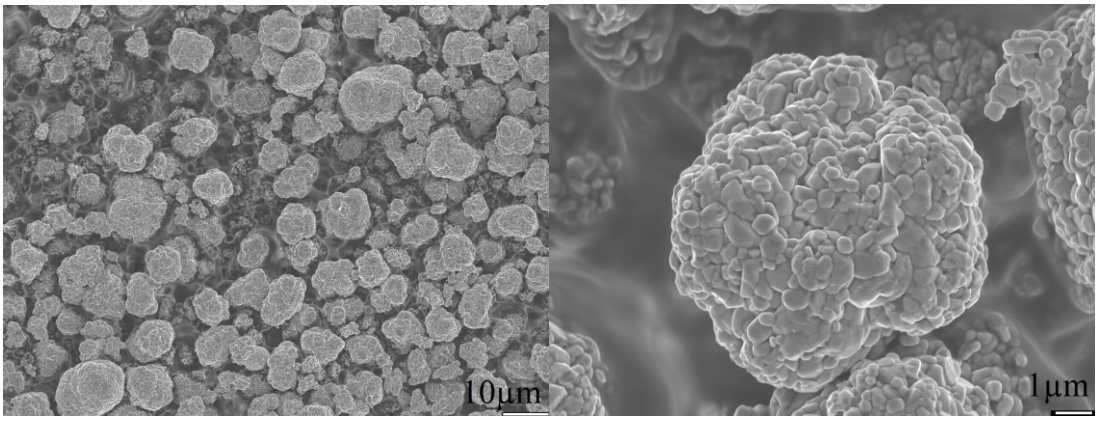

a) b)

Figure 4-1 SEM images of cathode of 333 compound showing of a) distribution of secondary particles and b) one secondary particle consisting of primary particles

Monte Carlo simulation of interaction volume

Since the region of interest is inside each single secondary particle, signal from outside the particles, in neighboring particles and support used to observe them must be eliminated by using the appropriate experimental conditions. Therefore a lower accelerating voltage is needed during SEM observations and analysis in order to ensure that the acquired X-ray signal is solely from within the secondary particle investigated. However, for analytical work, it is important that there is sufficient signal and that all peaks of the elements analyzed can be detected. This, on the other hand, is only possible at higher accelerating voltage of the electron beam: higher accelerating voltages are needed for the quantification work of a large range of elements. Therefore, an optimal accelerating voltage, balancing the need to contain the interaction volume within the secondary particles and the need to

excite the higher atomic number elements, was sought after. Interaction volumes for the electron beam interacting with the 333 compound specimen were therefore simulated with the Monte Carlo method using software available in the literature (the CASINO software from McGill University[46]). Then, the size of the simulated interaction volume was compared with the size of the secondary particles of 333 compound to find the optimal accelerating voltage.

There are two diagrams showing the electron's trajectory in Fig. 4-2. The interaction volume was observed from x-y, and x-z cross sections directions. The red trajectory represents the electrons that make their way out of the interaction volume as backscattered electrons while the blue one represents electrons that remain inside the sample and never make their way out. Therefore, as long as the volume contained within the red and blue trajectories is smaller than the size of secondary particles, the X-rays will be generated from within the secondary particles representing exactly the local compositional information.

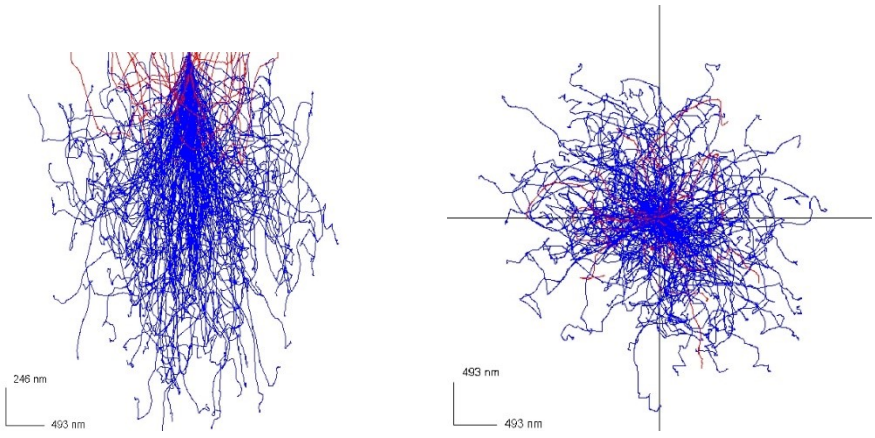

a) b)

Figure 4-2 The interaction volume represented by Monte Carlo Simulation results calculated with CASINO software [46]. a) x-y cross-section and b) x-z cross-section of the interaction volume under 15kV accelerating voltage. The scale bar in different direction varies, and the corresponding results of the dimension of electron trajectories (red lines) are shown in Table 4-1.

Table 4-1 shows the size of the interaction volume under different accelerating voltages. Usually 5kV is too small for activating enough signal as the K lines for Co, Mn and Ni are not excited, and 20kV causes charging effect during imaging and analysis due to the low conductivity of the NMC material, so these two values are used as the extremes. However, even under 20kV, hence the largest interaction volume with the specimen, the size of the simulated red line is only 4.0 × 3.5 × 3.2 μm. These dimensions are much smaller than the average diameter of the secondary particles which ensures all the signals detected are from one single secondary particle. Moreover, when the measurements were carried out, the central position of the large particles was used in order to ensure no possible signals from the other areas surrounding the particles. Considering the difficulties due to charging effects of the 333 compound, accelerating voltages of around 15kV were used for the measurements.

Table 4-1 The dimensions of the interaction volume of NMC with different accelerating voltage.

Dimension	Accelerating voltage			
	5kV	10kV	15kV	20kV
x(nm)	1210	2159	3044	4138
y(nm)	1420	2213	2829	4203
z(nm)	546	857	1085	1354
Interaction Volume(μm^3)	0.938	4.093	9.345	23.548

As shown in Fig 4-1, secondary particle consists of many small primary particles with some small amount of voids between them. This means that electrons might travel to slightly larger volumes than the assumed from calculations of a fully dense NMC secondary particle. However, due to the large size difference between the interaction volume and the particle's diameter, this effect can be safely ignored.

ZAF Factors

Matrix effects including ZAF factors need to be considered for the determination of accelerating voltage as well, because the optimal accelerating voltage determination is necessary for more accurate quantitative EDS data. However, there are additional

limitations for the quantification. The Li X-ray signal cannot be detected by EDS, so the ZAF calculations cannot be applied for the full list of elements. A small energy range, from 13, 15, 18 to 20kV was chosen as the condition to calculate the ZAF factors. Basically the Oxford Instrument's software *Cal ZAF* was used to simulate the interaction between high energy electrons and atoms in the specimen. Then the corresponding ZAF factor of each atom was calculated by the software. The best ZAF value would be the one closest to 1, which means less matrix effects need to be corrected, as explained in section 2.4.2. ZAF factor values of different elements under different accelerating voltages are shown in Table 4-2. The numbers in bold and italic were closest to the ideal value, which means least matrix effects were corrected. The chosen accelerating voltage of was 15kV due to a compromise between low values of O and transition metals ZAF factors.

Table 4-2 The ZAF factor calculated according to different accelerating voltage.

ZAF	10kV	13kV	15kV	18kV	20kV	30kV
Ni Kα	1.1463	1.1257	1.1176	1.1103	***1.1076***	1.1084
Co Kα	1.18	1.164	1.1584	1.1544	***1.1539***	1.1657
Mn Kα	1.0969	1.046	1.023	0.9989	***0.9862***	0.9384
O Kα	1.1416	***1.2948***	1.4033	1.5697	1.6798	2.152

Standards preparation

As discussed in chapter 3, experimental procedure section, there were four standards preparation methods (Fig. 3-4). We did not use the "standardless" method because of the limited accuracy compared to the customized standards quantification method. This was proven through the comparison between the "standardless" method and the customized standards method. With the use of the standards, the relative error in the carbon quantification (carbon would be detected because of carbon block matrix, deposition on the sample, or even from the detector itself) was reduced to a value lower than 2% (Table 4-3). In addition, the intensity correction index was used to measure the closeness between the real spectrum and the simulated spectrum with standards. Ideally if the intensity correction index is 1, there is perfect match between the simulated and experimental spectrum and a more accurate quantitative value is expected. Usually, the acceptable range

of the correction index is between 0.8 and 1.25. After the standardization, the O value is closer to 0.8 which means the quantitative result is more reliable (Table 4-3). These tabulations indicate that standards must be used to lower the relative errors, and reduce the intensity correction index to an acceptable range.

Table 4-3 Comparison of relative errors and intensity correction index before (using a standardless quantification) and after standardization with reference samples prepared in our work. The standard samples are prepared by cross-sectional polishing as described in section 3.1.3.

	Relative Errors		Intensity Correction Index	
	Before	After	Before	After
C	***2.08%***	***1.94%***	0.6299	0.5361
O	0.46%	0.45%	***1.8902***	***0.7764***
Mn	1.03%	1.31%	0.9407	1.1268
Co	1.18%	1.57%	0.8488	1.0055
Ni	0.60%	1.75%	0.8786	1.0314

Among all four standard sample preparation methods, the two using epoxy were not chosen. There are two reasons for this: one contribution is related to the charging effects. In order to avoid charging, a layer of carbon coating is necessary. This would result in a bias in the quantification since there are a lot of other elements in the epoxy (C, O, F, S), in addition to the extra carbon to avoid the charging. The second issue is contamination building up during analysis with the electron beam. Both issues complicate the whole process of quantification as standards are supposed to be as pure as possible.

If the composition (or average atomic number) of standards is closer to the composition of the specimen, the magnitude of the atomic number correction is closer to 1.0 and a smaller matrix effects correction is needed. Moreover, the amount of absorption is similar to the specimen because the characteristic x-rays absorption is more similar to the absorption in the sample. In the 333 compound, the fluorescence effect is very close to 1 so it was ignored. Therefore, the pellets standards of $LiMn_2O_4$, $LiCoO_2$, and $LiNiO_2$, were used finally.

SEM-EDS Analysis

The area of interest for analysis was imaged with secondary electrons and backscattered electrons in (Fig. 4-3).

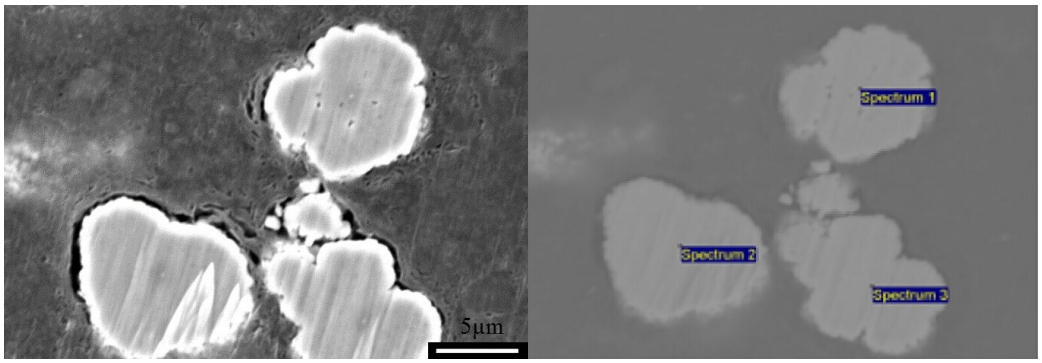

a) b)

Figure 4-3 Cross-section polished NMC secondary particles in a) SEI and b) BSEI.

The signal from the carbon block used was not considered in the quantification. Also, since Li was not detected by EDS, Li was set by default at 25% based on the nominal formula unit so that the absolute composition ratio of other elements could be compared with the stoichiometry of the nominal chemical formula of $LiMn_{0.33}Co_{0.33}Ni_{0.33}O_2$, in which Li is 25%, O is 50% and all transition metals are claimed to be 8.33%.

The data was acquired from the center of the large secondary particles as shown in Fig. 4-4. In each measurement, 30 particles were analyzed to check the composition, and then the average and the standard deviation of different elements compositions were calculated. Below are all the results comparing with ICP-MS in Table 4-4.

Table 4-4 Quantitative results of 333 compound by three preparation methods comparting to ICP-MS results.

%	Mn	Co	Ni	O
Cross-sectional polishing NMC	12.3±0.9	13.3±0.6	13.6±0.4	35.8±0.5
Mechanical polishing NMC	16.1±2.7	12.3±2.2	12.8±2.7	39.6±1.0
Pellets NMC	11.7±1.0	14.3±1.1	14.6±0.8	34.4±1.7
ICP-MS results	9.0±1.0	8.7±0.6	8.4±1.2	50.0±0.4

Our results show that preparation of samples with mechanical polishing generates very high standard deviations indicating unstable results. We postulate that it is the introduction of cracks and contamination from the epoxy and the roughness due to polishing that causes the large deviation in the quantitative analysis results. Results from samples prepared as pellets and the cross-sectional methods appear more stable based on the standard deviation. However, comparing to the ICP results it is clear that there are systematic deviations in the content of the transition metals. We believe this is due to the inaccuracy in the detection of low energy X-rays for low atomic number elements and in this case for O which skews the other values of composition for the cations. In addition, in the "pellets NMC" method, the sample and all three standards can be inserted into the chamber together. In the "pellets" method, the approach of preparing the sample and standards is exactly same. Therefore, there are similarities in the sample geometry and this lowers some of the systematic errors. Therefore, all the results shown below were obtained with pellets of NMC, and three pellets of the standards: $LiMn_2O_4$, $LiCoO_2$, and $LiNiO_2$.

Fig. 4-4 a) shows the variance of the oxygen concentration, and all transition metals in different secondary particles. It is obvious that the O content varies a lot. As mentioned before, the quantification of low atomic number elements like oxygen in EDS would not be considered accurate. Therefore, we will comment only on the relative ratio of transition metals. In order to reduce the variability and focus on the quantification of the transition metals, we simplified the quantification by assuming that the oxygen concentration 50% as shown in Fig. 4-4 b). It is claimed by S.C. Yin [47] that the 333 compound can be considered as the solid solution of $LiMn_{0.5}Ni_{0.5}O_2$ and $LiCoO_2$. However, according to the results shown in 4-4 b), the Mn doesn't follow exactly the same trend as Ni. On the other hand, in most particles, Ni and Co seem to have similar values in the distribution. In addition, the $LiCo_{0.5}Mn_{0.5}O_2$ is not considered structurally stable as discussed in section 2.2. So the assumption of solid solution of $LiCo_{0.5}Mn_{0.5}O_2$ and $LiCoO_2$ cannot be proposed. Therefore, considering the random distribution of transition metals in the transition metal layer [1], this 333 compound we have studied would rather be considered as the solid solution of $LiMn_2O_4$, $LiCoO_2$, and $LiNiO_2$.

Moreover, there is less Mn than Ni or Co in most particles shown. The characteristic energy of the Mn Kα peak is only 5.9eV, which is lower than the one for Ni (Kα peak:

7.5eV) and Co (kα peak: 6.9eV). This means that it is, in principle easier to excite X-rays from Mn atoms than from Ni or Co atoms and therefore the differences are significant, leading to the conclusion that the concentration of Mn is lower than Ni or Co in secondary particles.

In conclusion, inside secondary particles, there are variations in the concentration of different transition metals. Even though in some secondary particles, Ni and Co concentrations are similar, for most of the particles, three transition metal atoms have different concentrations. In addition, among different secondary particles, the concentration of Mn is not stable, so does Co or Ni.

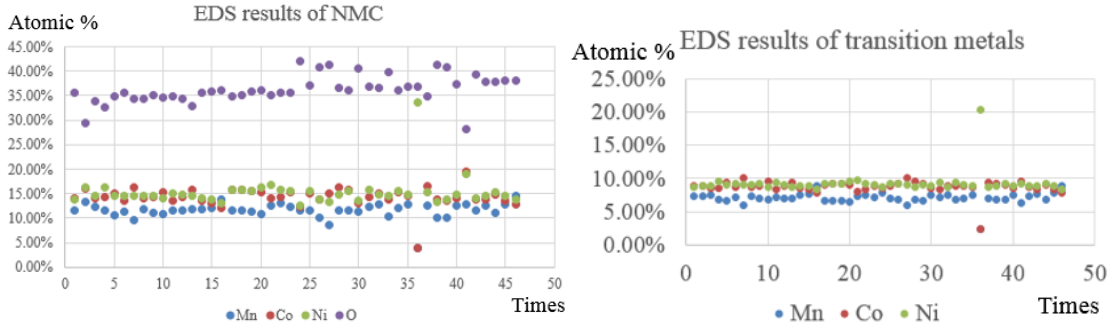

a) b)

Figure 4-4 The EDS results of oxygen and all three transition metals in 333 compound metals.

4.1.1.3. Micro-scale material compositional analysis: SEM-AES

Sample preparation

In AES measurements, the sample surface must be flat. In addition, since the epoxy charges vigorously, mechanical polishing of embedded samples and the coating with a carbon layer cannot be considered. Therefore, the cross-sectional polishing and the pellet methods must be used in the Auger measurements. However, since the cross-sectional polishing method reveals more internal structure of the particles, we opted for this method as the main approach to do the AES quantification of the 333 compound.

Standards preparation

Similar to EDS, customized Auger spectra of standards are needed, since the manufacturer's internal reference spectra from standards are not obtained in exactly the same condition as the measurements in our work. In addition, the composition and crystallographic structure of the standards is not exactly the same (leading to shifts in the spectra and lower fits in the quantification). In our work, we ensured that the spectra of standards and specimen were detected under the same conditions, so that discrepancies in the fitting of spectra can be reduced and the quantification can be done more accurately.

The major difference in AES measurements, as compared to EDS is about the Li standards preparation. The first approach we attempted was through the use of Li oxide powder pellets, in which the pure Li oxide peaks are assumed to be similar to the Li-O bonding in the 333 compound. However, our results show that this reference is not suitable because of the poor fit of the Li peak of the reference as compared to the Li in the 333 compound. References of the Li peak in standard of $LiMn_2O_4$, $LiCoO_2$, $LiNiO_2$ were therefore selected.

In terms of the standards for the transition metals, we opted for the references of $LiMn_2O_4$, $LiCoO_2$, $LiNiO_2$ and MnO_2, Co_3O_4, NiO as the valence in these elements approaches what is expected to be in the 333 compounds. There are totally three methods discussed below.

Optimal operational condition

Moreover, for the same sample and standards preparation, different modes and accelerating voltages were tested. Results are shown in Table 4-5. Mode 3 can provide higher energy resolution, but higher noise level as well. On the other hand, Mode 5 has lower energy resolution therefore insufficient signals can be acquired. In the experiment, mode 3, 4 and 5 were tested. Results under mode 3 were not stable and not comparable with the quantification results acquired from ICP-MS and EDS. Mode 4 and 5 could give stable and trustable results. Therefore, mode 4 was chosen as the optimal mode due to its higher energy resolution.

In terms of the accelerating voltage, both 5kV and 10kV could provide stable and trustable results under mode 4, however, since 10kV might cause more charging effect for NMC materials, 5kV was used.

Table 4-5 Quantification results of method 3 with different modes and accelerating voltages.

Mode	kV	**Li**	**O**	**Mn**	**Co**	**Ni**
M5	10	21.7	52.2	8.9	8.1	9.1
M4	10	21.7	52.2	8.9	7.9	9.3
M4	5	21.5	52.4	9.5	8.5	8.3
M3	5	20.7	52.8	11.3	7.8	7.3
M3	5	15.0	66.0	7.9	5.3	5.8

AES-analysis

Li peaks are only present in the low energy range of the Auger spectrum, which is below 100eV. In this range, however, there are peaks from all transition metals as well. All peaks in low energy range are overlapping and therefore the peaks appear broader. Another complication is the carbon contamination on top of the specimen and the fact that it is not homogeneously distributed. When Auger electrons pass through this carbon layer, they are absorbed and lose energy and this causes some broadening of the peaks. For a spectrum with broader features, the convolution process is a challenge.

The carbon peak is around 250eV. Because carbon absorbs the Auger electrons, it must be removed using sputtering with an Ar beam within the vacuum chamber. This process, however, will cause the roughness of the sample surface which reduces the accuracy and stability of the results.

In the higher energy range from around 400eV to 900eV, there is the oxygen peak around 510eV and all transition metal peaks. The oxygen peak is isolated from other peaks, while all transition metal peaks are overlapping. However, compared to the low energy range, there are fewer overlapping peaks, and both oxygen and transition metals have their own independent peaks making the quantification easier and more accurate in this range.

Several different approaches were applied to do the quantification analysis. The first approach (Fig. 4-5) was based on the characteristic peaks of all elements. That is to say,

the quantification of Li was carried out from the low-energy range, while transition metals and oxygen signals were extracted and quantified from high-energy range. More specifically, in the low energy range, all standards of Li_2O, MnO_2, Co_3O_4, and NiO were used to quantify the composition of Li. Then the spectrum was scaled down to around the oxygen peak, and Li_2O was used for the quantification of oxygen. The last step was to quantify all transition metals in the whole transition metal range, using MnO_2, Co_3O_4, and NiO. In this way, all different elements were quantified separately.

However, the first problem encountered is related to the Co valence, which was not purely +3 in Co_3O_4 and this meant that the composition ratio of Co to oxygen deduced from the measurement would not be accurate because of the spectrum of Co in the +3 valence state was not a perfect reference for the quantification. In addition, the lithium was removed fast during sputtering to remove the carbon contamination or during the analysis because of the incident high energy electrons. This could give rise to additional quantification errors. In order to avoid some of these effects, a fresh sample, inserted in the vacuum chamber right after the sample preparation was used so as to reduce the carbon contamination and the sputtering. Lower accelerating voltage was also used to avoid electron beam-induced effects. In addition ion neutralization was used to reduce the charging effects and related errors.

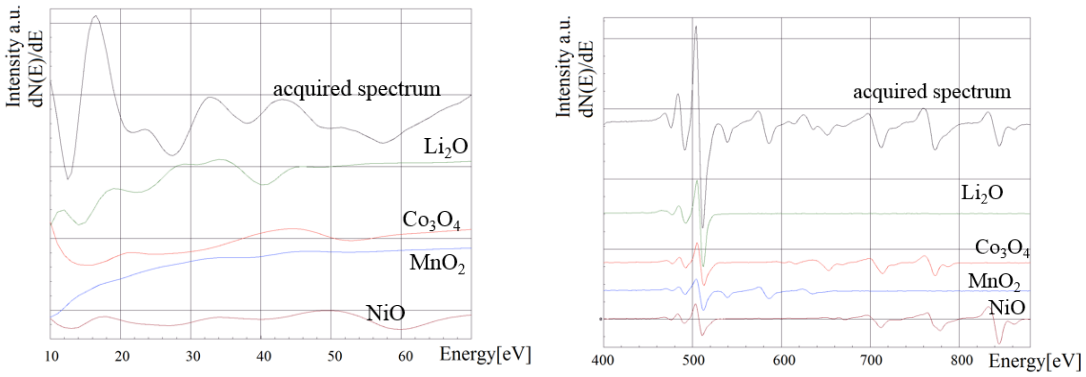

a) b)

Figure 4-5 (a) The convolution work of the first method by using three transition metal oxides and lithium oxide to be the standards in low energy range. (b) Oxygen peak with Li_2O standards; transition metal oxides as standards in high energy range.

In spite of the attention to such details, this energy fitting approach with consideration of the low energy range for the Li peak failed. Therefore a method without consideration of low energy range was tried.

This second approach makes use of the high energy range from 400 to 900 eV. However, there is no Li signal used and, therefore, the excess oxygen was assumed to be bonding with lithium. In this way, the Li concentration is derived from the quantification of the other four elements. This affects the quantitative analysis of concentration of Li, since all elements' quantification is carried out separately.

The third approach is based on the same high-energy range but with different standards, namely $LiMn_2O_4$, $LiCoO_2$ and $LiNiO_2$. In this way, the Li was assumed to be bonding to different transition metals and calculated based on the concentration of all the three standards. There were still possible sources of errors: first of all, the Mn and Ni valence was different from the valence in the 333 compound; second, the relative ratios of Li and O are fixed in all three standards, and this might cause some inaccuracy in the calculation of Li and O concentrations in the 333 compound. In all, even though problems still exist, this method can provide more consistent results than the first two methods.

Table 4-6 are the summary of all three AES methods combining with ICP-MS and some EDS results:

Table 4-6 Quantitative results of all Auger methods, ICP-MS, and EDS methods.

Atomic %	Li	O	Mn	Co	Ni
Auger Method 1	3.2±1.7	57.3±2.3	13.0±7.2	9.7±8.6	16.9±7.0
Auger Method 2	13.5±8.2	54.6±3.2	13.0±2.2	8.8±1.7	10.0±2.0
Auger Method 3	21.8±0.1	52.1±0.1	8.5±0.3	8.3±0.3	9.3±0.1
ICP-MS	25.0±0.4	49.0±0.4	9.0±1.0	8.7±0.6	8.4±1.2
EDS CP		35.8±0.5	12.3±0.9	13.3±0.6	13.6±0.4
EDS Pellets		34.4±1.7	11.7±1.0	14.3±1.1	14.6±0.8

In method 1, the Li concentration is very low, and significantly out of the range expected from the ICP results. The transition metal concentrations have very high standard deviation

which means the results are not stable and consistent. In method 2, the results are much better than method 1 in that the standard deviation is lower. However, in comparison with ICP results, the Li and O standard deviations are still high which means the results are not reliable. So in all, both method 1 and 2 are not reliable in the quantification of NMC materials, mostly due to the unreliable Li quantification. Method 3 was stable and results were very consistent considering the standard deviation as well. Comparing with ICP, it also showed quite similar results which meant Auger results were much closer to reality than EDS results.

Since method 1 took all the characteristic peaks of different elements into account in the quantification, it was expected to be the most accurate. However, since there were too many overlapping peaks and fitting errors occurred in the low energy range, this quantitative results were not stable and consistent. Method 2 cannot provide as consistent results as method 3, because of the wrong choice of the standards. Method 3 appeared to give very stable results. The first reason for this is that it considers only the high energy range with little overlap of peaks. The other reason is that $LiMn_2O_4$, $LiCoO_2$ and $LiNiO_2$ have similar bonding with the 333 compound so that fewer matrix effects needed to be corrected. Therefore, in the following work we used this method for the for the quantification of NMC materials and their evolution.

The results in Fig. 4-6 a) show several concentration measurements of the 333 compound. It is obvious that, compared to the EDS results, the O concentration is very stable, except for only one spot with large deviation. The Li concentration does not show large variation as well, which means the results are consistent and reliable. In terms of transition metals, in a), they are almost overlapping with each other which means that they have similar concentration in different secondary particles. When we analyze in details the transition metal results in b), we observe that the AES results have the opposite trends as compared to the EDS results. Among 11 datasets, in 7 locations, the Mn concentration is between the Ni, and Co while in EDS measurements, the Mn concentration is usually the lowest.

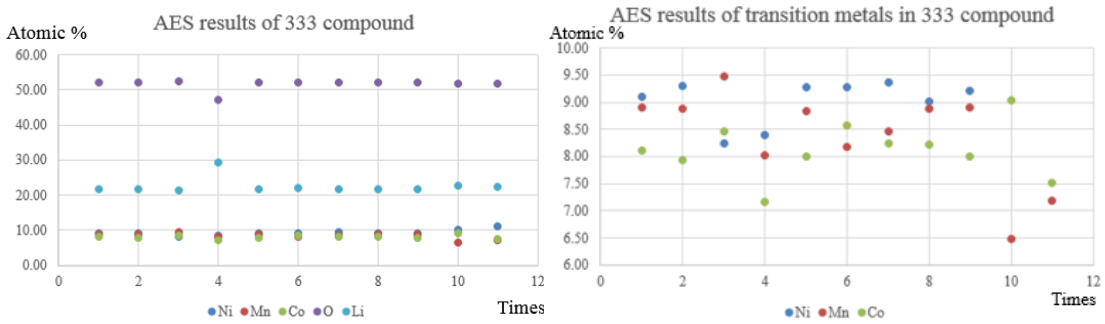

a) b)

Figure 4-6 The AES results of a) lithium, oxygen and all three transition metals in 333 compound; and b) only transition metals.

In conclusion, no matter in EDS or AES, the variation between Mn, Ni and Co inside each secondary particle exists, and the variation of one transition metal between different secondary particles exists as well.

4.1.1.4. Nano-scale material compositional analysis: TEM-EDS

In TEM-EDS, similar procedures were applied as in SEM-EDS. Table 4-7 are the final quantification results of TEM-EDS compared to the ICP-MS and SEM-EDS results.

Table 4-7 The ICP-MS results and all EDS results comparison.

Atomic %	**Li**	**O**	**Mn**	**Co**	**Ni**
ICP-MS	25.0±0.4	49.0±0.4	9.0±1.0	8.7±0.6	8.4±1.2
SEM-EDS CP	25.0 assumed	35.8±0.5	12.3±0.9	13.3±0.6	13.6±0.4
SEM-EDS Pellets	25.0 assumed	34.4±1.7	11.7±1.0	14.3±1.1	14.6±0.8
TEM-EDS	25.0 assumed	28.8±7.1	15.3±3.5	15.8±2.4	15.0±2.1

Generally in EDS analysis, the peaks for low atomic number elements could not be detected very accurately due to the absorption in the detector window. This also applies for in TEM-EDS. Therefore, oxygen composition variations are not unexpected. For the

transition metals we expect a more reliable results from TEM and the TEM average results are very similar to each other in Table 4-7. However, considering the standard deviation into account, there is even bigger variation in different particles for each transition metal comparing to SEM-EDS results. This effect can be explained at the structural level as primary particles may have different composition even if, on average, when added together the results from many particles are statistically similar to each other. While inside the large secondary particles, the SEM-EDS results were a bit different because of more influential factors involved such as: the pore numbers and size, and transition metal ions dissolution.

The quantification results of oxygen and all transition metal elements in TEM EDS are shown in Fig. 4-7 a). Compared to the SEM-EDS, and AES, the results in TEM-EDS are much more variant, especially in the low atomic number elements, such as in oxygen. If we focus on the transition metals alone [Fig. 4-7 b)] assuming a stoichiometric oxygen content, we can comment on the relative concentration of the transition metals. At the primary particle scale, the results show that Mn concentration varies the most. In addition, in most primary particles detected, there is more Co than Ni. Again, in TEM-EDS, the variation of three transition metals inside one particle and the variation for one transition metal between particles exist. The errors caused by the techniques or standards might influence the quantification results as well.

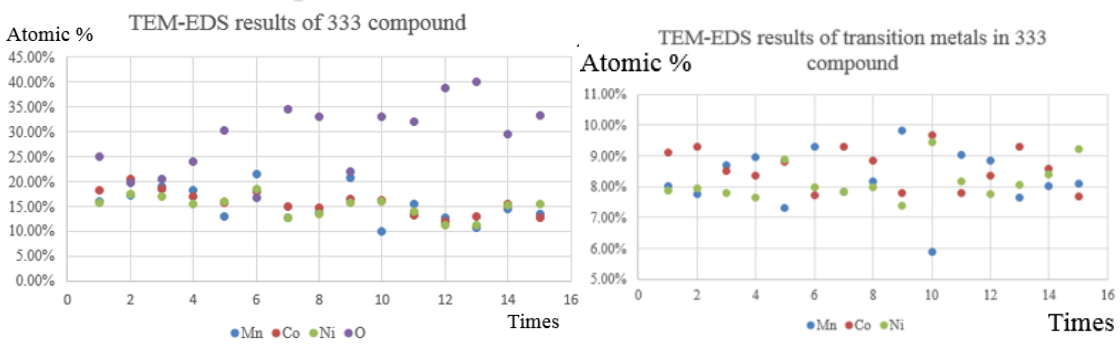

a) b)

Figure 4-7 The TEM-EDS results of a) oxygen and all three transition metals in 333 compound; and b) only transition metals.

4.1.2. Compositional comparison of pristine and cycled $Li_{1.2}Mn_{0.54}Co_{0.13}Ni_{0.13}O_2$

After the comparison among different quantification methods and the demonstration that AES provides reliable results at the scale of primary particles, we are able to use these methods to study different materials. In addition, Li can be detected in AES and not in EDS or WDS. Moreover, the amount of sample needed in AES was much lower than in SEM-EDS. In AES, only very few small particles (the cathode material from the button battery is enough for at least 5 samples in AES), while in EDS, the cathode material from at least 4 to 5 button batteries is barely enough for making even one pellet to do the EDS measurements.

Therefore, the composition of cathode material $Li_{1.2}Mn_{0.54}Co_{0.13}Ni_{0.13}O_2$ (HENMC) is checked in this thesis by AES. There are pristine HENMC, and HENMC samples after 1, 50, 100 cycles, and the corresponding compositional change was analyzed.

Pristine $Li_{1.2}Mn_{0.54}Co_{0.13}Ni_{0.13}O_2$

Both the method 1 and 3 of AES were used to do comparison and they were tested to see whether it was applicable in the case of high energy lithium transition metal oxide or not in Table 4-8 and Figure 4-8:

Table 4-8 The quantitative results of pristine $Li_{1.2}Mn_{0.54}Co_{0.13}Ni_{0.13}O_2$.

Atomic %	Expected ratios	Method 3
Li	30	17.4±1.1
Ni	3.25	3.7±1.2
Mn	3.25	20.2±0.9
Co	3.25	3.7±1.7
O	50	55.1±0.7

According to the results, for method 1, the Li and O compositions were undergoing big variations which are unstable and not trustable. Secondly, the standard deviation was out of range as well. Therefore again the method 1 was not suitable for the HENMC and it will not be applied to the rest of the discussion.

Based on the formula $Li_{1.2}Mn_{0.54}Co_{0.13}Ni_{0.13}O_2$, the atomic ratio is expected to be Li: Ni: Mn: Co: O = 30: 3.25: 13.5: 3.25: 50 as shown in Table 4-8. Therefore, there is large

difference in compositions of Mn and Li between expected ratio and the results extracted from method 3. The Li results are clearly different from the expected atomic percentage of 30%, the partial reason is that the lithium concentration is quantified directly, and it relied on the quantification of all three transition metals. The extra Mn might be from the local heterogeneous distribution of Mn. Since the pristine $Li_{1.2}Mn_{0.54}Co_{0.13}Ni_{0.13}O_2$ composition is based on two components, Li_2MnO_3 and $LiMn_{0.33}Co_{0.33}Ni_{0.33}O_2$, the Mn concentration in these two phases are different. It has been demonstrated that in the pristine HENMC these two components exist in the form of solid solution, that is to say, both components distributes homogeneously in the particles. However, this might not apply to each small area in nano-scale. Therefore, the little amount of excess of Mn can be explained by the Mn-rich area reasonably.

In most particles, the concentration of oxygen is quite stable. Moreover, the concentration of Li is stable too. Except for one particle, there is a big variance of transition metals, which causes the change of Li concentration. Overall in three transition metals, the concentration of both Co and Ni are pretty stable, and they have similar concentration as shown in the formula unit as well. On the other hand, the concentration of Mn is much higher than 13.5 and it also shows larger variance. This can be explained by the possible existence of Mn-rich domains in micron-level. How the Mn-rich domains are distributed needs further experiments.

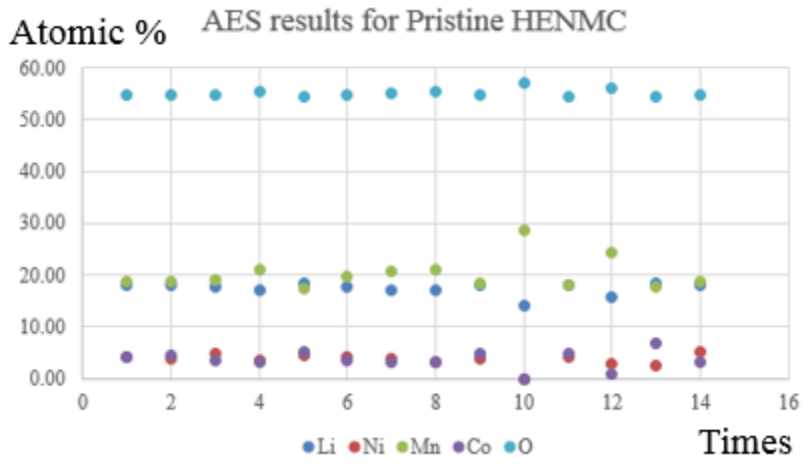

Figure 4-8 The AES results of lithium, oxygen and all three transition metals in HENMC.

Later on, the compositions of pristine HENMC and after 1, 50, 100 cycles HENMC are compared.

$Li_{1.2}Mn_{0.54}Co_{0.13}Ni_{0.13}O_2$ with 1, 50 and 100 cycles

For all three samples, method 3 was applied. The results combining with pristine HENMC sample results were shown in Table 4-9 and in order to have a better view of the changing trend, Fig. 4-9 was drawn.

Table 4-9 The quantitative results of non-cycle and cycled $Li_{1.2}Mn_{0.54}Co_{0.13}Ni_{0.13}O_2$ with method 3.

Atomic %	Pristine	1 cycle	50 cycles	100 cycles
Li	17.4±1.1	16.8±2.0	15.8±0.2	16.0±1.1
Ni	3.7±1.2	2.1±1.1	2.0±0.3	1.7±2.0
Mn	20.2±0.9	21.9±5.3	24.6±0.4	24.1±3.0
Co	3.7±1.7	3.7±5.4	1.5±0.3	2.2±1.2
O	55.1±0.7	55.5±1.3	56.1±0.1	56.0±0.8

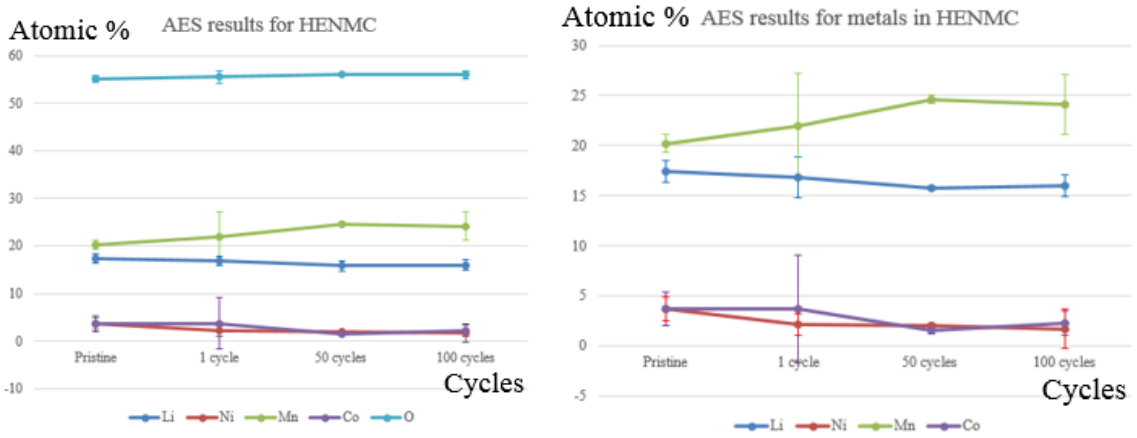

Figure 4-9 The quantification results of HENMC by using method 3.

Since in cross-sectional polished samples, spots of interest were chosen randomly inside the particles, the average concentration underwent insignificant difference. However, taking the standard deviation into account, after the 1st cycle, the Mn concentration

experienced a big variation. However, after 50 cycles, it becomes stable. Moreover, after 100 cycles, it is unstable again.

During the first cycle, the Li and O was removed from Li_2MnO_3 by the ratio of 2:1, and there is a big variation in Mn. Especially for Li_2MnO_3, some spinel structure was observed from the DPs and the distribution of Mn changed according to the AES results. According to Jarvis [48], pristine $Li_{1.2}Mn_{0.54}Co_{0.13}Ni_{0.13}O_2$ can be treated as the solid solution of: $LiMn_{0.33}Co_{0.33}Ni_{0.33}O_2$ and Li_2MnO_3. However, during cycling, a new spinel phase appeared indicating phase transformation. In the surface, more Mn rich phase would show up, while in the bulk material, more of the 333 compound exists. That is to say, the separation of two phases (monoclinic and rhombohedral phases) explains the uneven distribution of Mn in my results. During the 50th cycle, there was no big standard deviation observed. This is because local transformation from monoclinic structure Li_2MnO_3 to the spinel structure $LiMn_2O_4$ was complete in most domains of the sample. However, when it goes up to the 100th cycle, there is a big difference because of the formation of new structure. Morphologically, there is a thick layer (pointed by the arrow) that shows up as in Fig. 4-10.

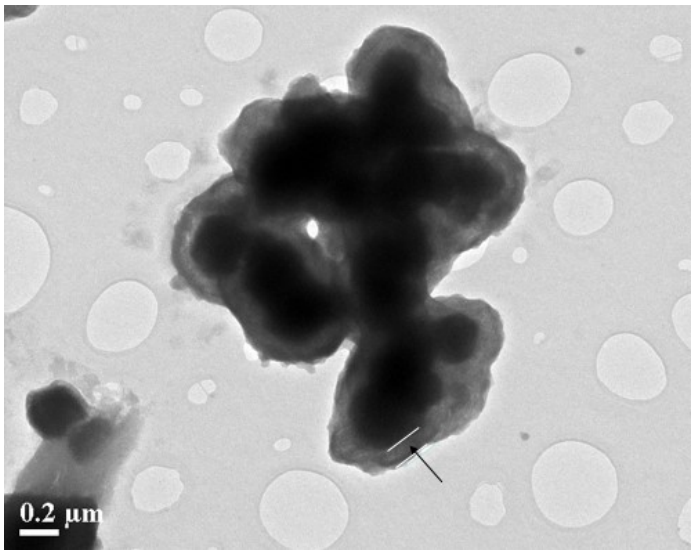

Figure 4-10 The SEI around HENMC particles morphology after 100 cycles.

This is potentially the solid-electrolyte interphase (SEI). Since after long cycling, there is the possibility that the electrolyte decompose slowly and form this SEI layer to inhibit more electrolyte with further decomposition. According to Jung Tae Lee [49], the SEI layer

is supposed to contain C, H, Li and O. In the TEM-EDS measurements, there is no signal from other elements this being consistent with the SEI (Fig. 4-11). However, since the particles are beam sensitive, the signal is very weak from these thick layers and further measurements would be needed to study quantitatively this decomposition products. The dark-field images demonstrate that, during line scan analysis the SEI layer appears damaged.

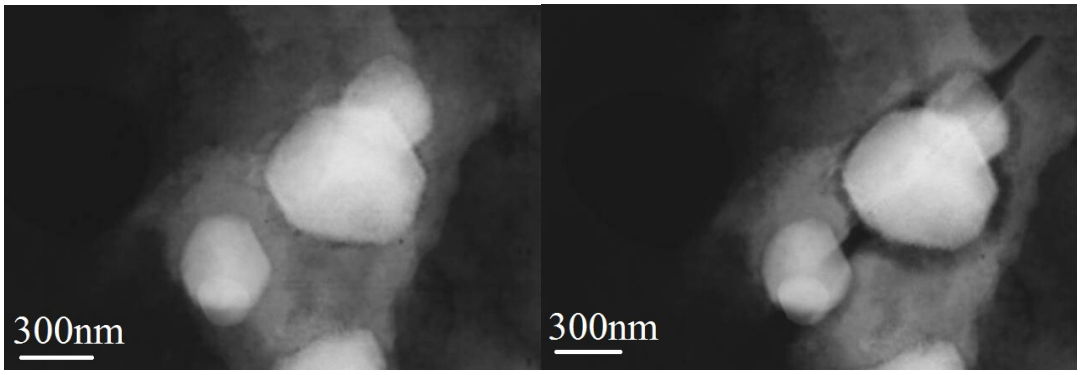

a) b)

Figure 4-11 The dark field images of HENMC after 100 cycles, a) before and b) after the TEM-EDS test.

4.1.3. Compositional comparison of pristine and ball-milled $LiMn_{0.33}Co_{0.33}Ni_{0.33}O_2$

As we have shown previously, pristine $LiMn_{0.33}Co_{0.33}Ni_{0.33}O_2$ (333 compound) is composed of secondary particles (around 8-12 μm) generated by the agglomeration of smaller primary particles. After ball milling, the particles are crushed into smaller ones.

The 333 compound was ball milled (BNMC is short for the 333 compound after ball milling treatment) to see if the performance of the cathode can be improved as a result of more surface area. In reality, the performance of BNMC was much worse than the pristine 333 compound with secondary particles. Here we studied the morphology and compared the composition of the pristine and ball milled NMC.

The most significant morphological difference between the two samples was that the 333 compound has secondary particles, however, in BNMC, all the big particles were

crushed into small ones which might introduce defects and contamination during ball-milling. The morphological comparison is given in Fig. 4-12.

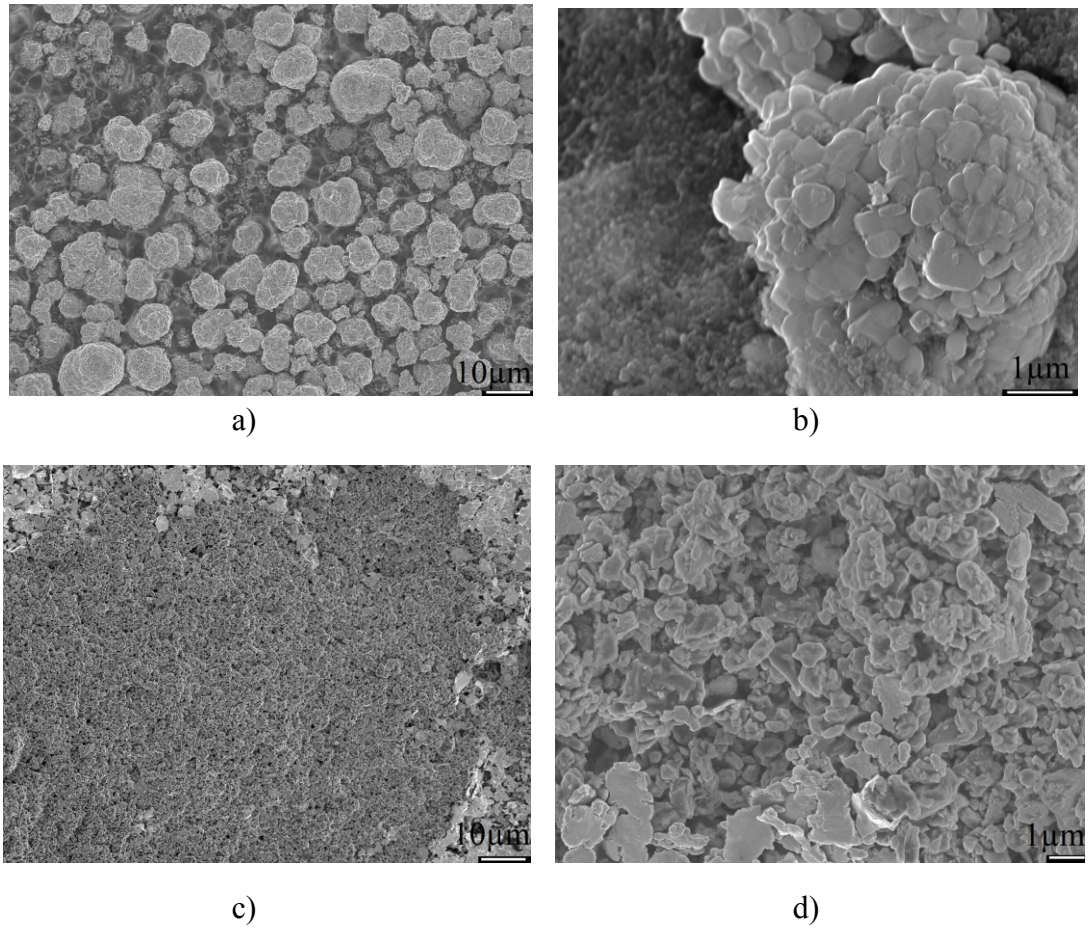

Figure 4-12 SEM images from NMC particles with a) low and b) high magnification. Ball milled NMC particles with c) low and d) high magnification.

By using these two materials, new cathode materials are fabricated in Fig. 4-13.

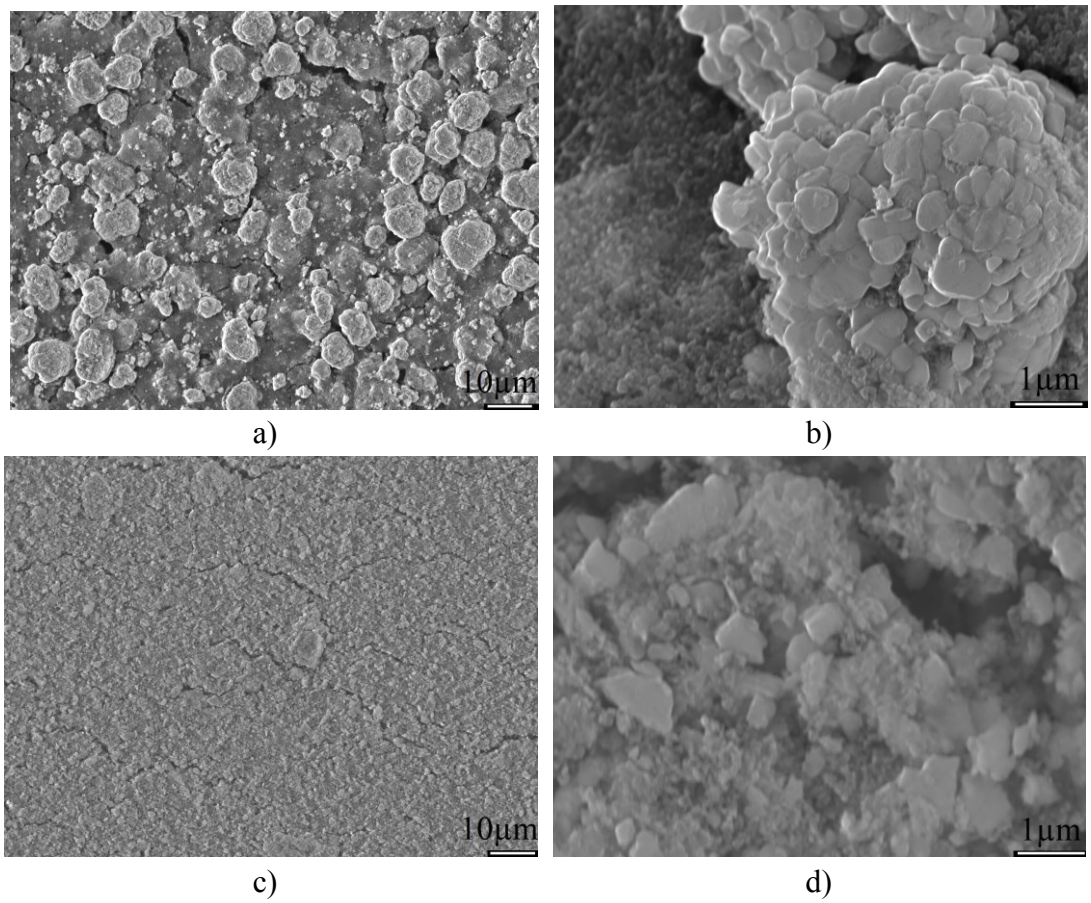

Figure 4-13 SEM images from NMC cathode with a) low and b) high magnification. Ball milled NMC cathode with c) low and d) high magnification.

Morphological difference might be one reason why the ball-milled NMC did not perform well during cycling. Li ions needed to diffuse from the cathode material (NMC) to the anode for the charge and discharge process. In between the large secondary particles, there is a significant volume to be filled with electrolyte and the binder (the electrically conductive phase), which means Li ions and charges can travel almost unrestrictedly. In the ball milled sample, large secondary particles were crushed into small pieces and these nano scale particles tended to agglomerate together. In this case, there is little space for either the electrolyte or the electrically conductive binder and leaving almost no space for diffusion of Li and electrons. Therefore, one explanation that the performance might be lower for BNMC is that the diffusion of the electrolyte is lower. However, this argument cannot explain why secondary particles, within which the diffusion of the electrolyte is

even lower within the particle, performs better. Table 4-10 are the results of the compositional information from EDS.

Table 4-10 The results of average and standard deviation of compositions of Oxygen and all transition metal results in NMC and ball-milled NMC (BNMC).

Atomic %	Mn	Co	Ni	O	Zr
NMC	11.7±1.0	14.3±1.1	14.6±0.8	34.4±1.7	/
BNMC	11.1±0.7	13.6±0.8	13.7±0.8	36.6±1.7	0.09±0.2

The transition metals and oxygen concentration for the BNMC does not appear to be significantly different: concentration and the standard deviation ranges were similar. However, the relative standard deviation of Zr, originating from the ball mills used for the milling process in BNMC was larger than average. This is due to the fact that the Zr was very unevenly distributed. It is unlikely that such small amounts of Zr are at the source of the lower performance of BNMC compared to NMC as well.

Some Auger analysis was also done to compare with EDS measurements. Since the Zr concentration was not very homogeneous distributed it was not taken into consideration in the AES quantification.

Table 4-11 The AES quantitative results comparison between NMC and BNMC

Atomic %	NMC Method3	Ball milled NMC Method 3
O	52.1±0.1	51.9±0.8
Ni	9.3±0.1	10.2±3.5
Mn	8.5±0.3	7.7±2.1
Co	8.3±0.3	8.1±1.8
Li	21.8±0.1	21.2±0.5

Table 4-11 shows similar situation with the pure pristine NMC results. Moreover, the composition of transition metals experienced a big difference. Even though the average values of all transition metals appears to change, taking into account the standard deviation there appears to be not much difference in the quantitative results. There is an obviously

larger variance in the BNMC results. This can be explained by two effects: 1) the composition of secondary particles and 2) the rough nature of the sample. Inside large secondary particles (the pristine material), the average composition is averaged over many primary particles. In the process of ball milling, the large secondary particles are broken apart and more local information can be revealed from the primary particles. It is therefore likely that subtle composition differences arise from changes in the primary particles. This is consistent with the data obtained in TEM-EDS results that has higher variation than SEM-EDS as well. The second effect is that the surfaces of the ball-milled sample as probed by in the AES measurements are more rough, giving rise to large signal variance due to the escape depth and angles of the sample surfaces, compared to the electron beam.

4.2. Structural Analysis

4.2.1 Structural analysis of pristine $LiMn_{0.33}Ni_{0.33}Co_{0.33}O_2$

4.2.1.1. Bulk material X-ray diffraction analysis

The structural information, such as lattice parameters and space group, from the bulk material $LiMn_{0.33}Ni_{0.33}Co_{0.33}O_2$ (333 compound) was acquired with X-ray diffraction (XRD). The determination of these parameters depends on fitting the acquired pattern with patterns available in the Inorganic Crystal Structure Database (ICSD) using Topas. The shape and the intensity of the characteristic peaks from the acquired (shown in blue) and the Topas simulated patterns (red) are shown in Fig. 4-14. A comparison between both patterns indicate a good agreement and the structural information acquired from the simulation is summarized in Table 4-12. Generally, the 333 compound is in a rhombohedral phase and belongs to the R-3m space group. Li, transition metals and oxygen atoms are in different atomic layers.

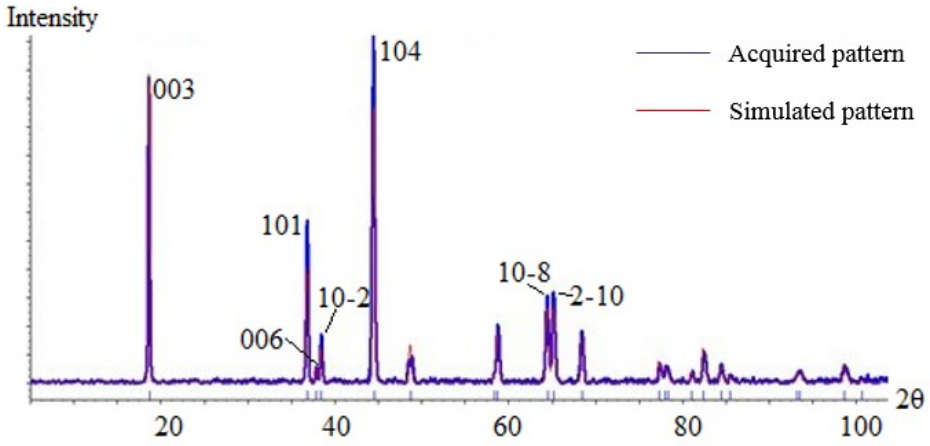

Figure 4-14 The comparison between acquired (blue line) and simulated (red line) XRD patterns with all characteristic peaks.

Table 4-12 Structural information acquired from XRD.

Atom	Occupancy	Atomic layer	Parameters

Li1	0.975	3a	Space Group R-3m
Ni2	0.025	3a	
Mn1	0.333	3b	
Ni1	0.309	3b	Lattice Parameters a = 2.86Å c = 14.23Å
Co1	0.333	3b	
Li2	0.025	3b	
O	1	6c	

When the intensity ratio of the main characteristic peaks, (003) and (104), is larger than 1.2, Whitfield et al., (2005) indicated that Li^+ ions are introduced into the transition metal layer. Moreover, the same work explained that the poor separation of the peak doublets (006)/(10-2) and (110)/(10-8) was due to a layered structure and disordered cations. In our project, the ratio of (003) and (104) is less than 1, showing that a small portion of Li ions was introduced into the transition metal layer. Poor separation of the same peak doublets are visible in Figure 4-14 indicating presence of a layered structure and disordered cations in the 333 compound.

High resolution XRD experiments were done with the step size 0.04º for a more detailed structural information. In order to calibrate peak positions, the 333 compound powder was mixed with a 1:2 ratio of Si single crystal, due to its fixed characteristic peaks (indicated by arrows) and absence of peak overlap. The comparison of acquired X-ray pattern and simulated pattern is shown in Fig. 4-15. A fine feature located approximately at 68º (circled in both Fig. 4-15 and Fig. 4-16) could indicate the presence of a second phase. Therefore, a smaller step size of 0.02º was used to differentiate this peak with background noise, as can be seen in Fig. 4-16. This small feature is more obvious with the smaller step size, but could still be considered noise and so further investigations with TEM electron diffraction may be useful to determine a second phase in the bulk material.

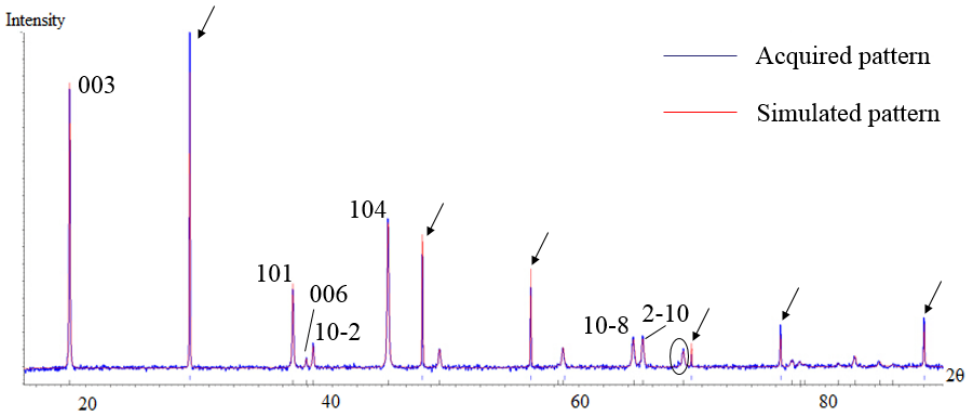

Figure 4-15 The comparison between experimental pattern of a mixture of Si (used as reference and its peaks are pointed by arrows) and 333 compound (blue line) with simulated pattern (red line) in high resolution XRD.

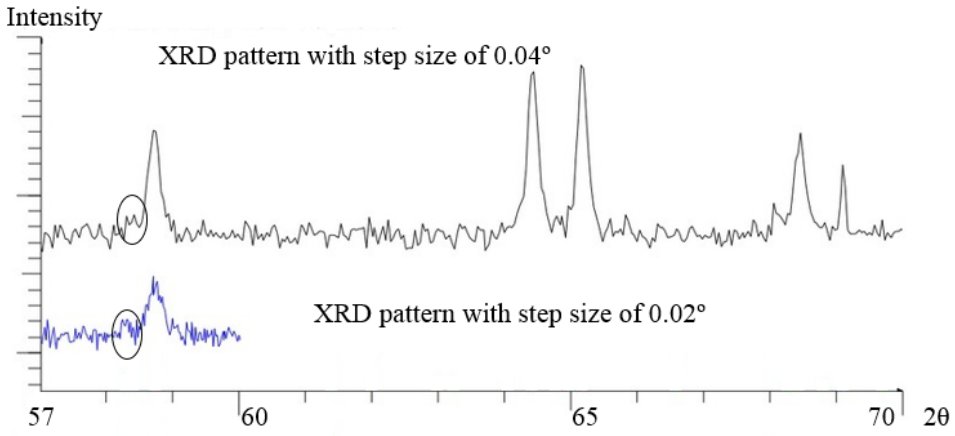

Figure 4-16 Comparison between XRD patterns of step size 0.04º and 0.02º.

4.2.1.2. Nano-scale TEM characterization: morphology and structure

Bright-Field Transmission Electron Microscopy (BF-TEM) images of the 333 compound are presented in Fig. 4-17. Most particles agglomerate as shown in Fig. 4-2-4a and are too thick for electron transmission. This can be overcome by analyzing the edge of the particle in an agglomeration or smaller single particles, found more rarely (Fig. 4-2-4

b). DPs can then be acquired and are used to check the nanoscale structural information of the primary particles.

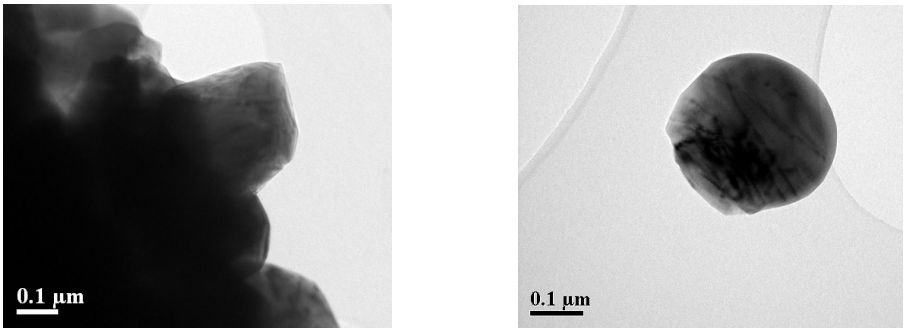

a) b)

Figure 4-17 TEM bright field images of 333 compound indicating that most particles are a) agglomerated, while some b) can be found isolated.

The determination of the space group can be done by indexing an acquired DP and comparing with a simulation using JEMS, as mentioned in section 3.2.3. According to Shaju, [50], two space groups have been detected in pristine 333 compound: trigonal R-3m (majority) and cubic Fd-3m. Therefore, we simulated DPs with the trigonal space group in different zone axis [shown below in Fig. 4-18 a), c) and e)] and compared with experimental DPs of the pristine 333 compound [Fig. 4-18 b), d) and f)]. Although the intensities of the spots between the simulated and experimental DPs are different, the position and distances of each spot are comparable. Therefore, they were indexed accordingly for the different zone axes: [001], [100] and [110]. Some spinel phases were also found with less frequency and Fig. 4-18 shows a simulation of Fd-3m space group in [001] zone axis with corresponding experimental DP. According to H. Gabrisch[51], there are approximately 11.1% of spinel phases among all the 30 DPs acquired in their work.

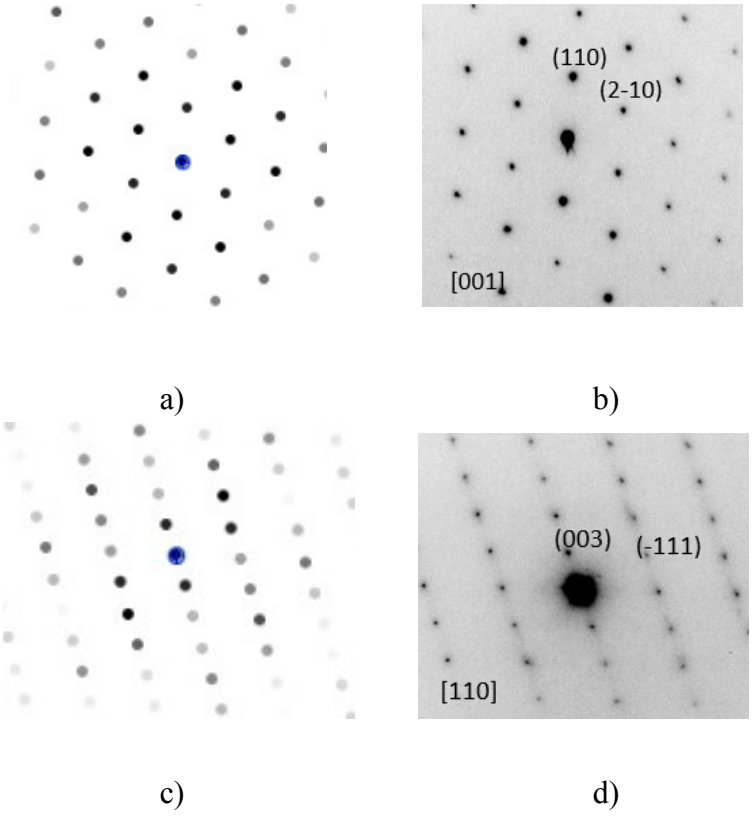

Figure 4-18 The simulated patterns of R-3m space group of zone axes by *JEMS* a) [001], c) [110]. b), d) are the corresponding real diffraction pattern of 333 compound.

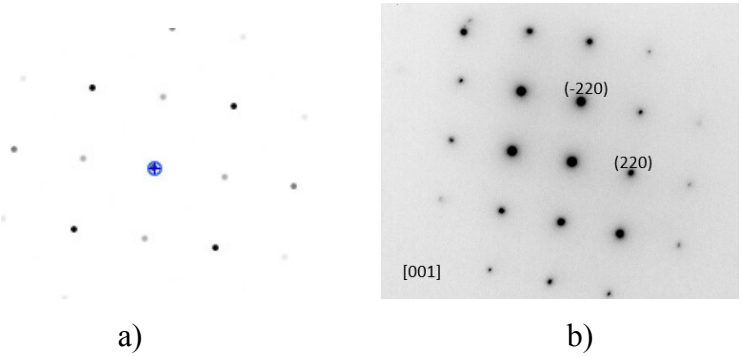

Figure 4-19 The simulated pattern of 333 compound in Fd-3m space group of zone axis [001] using JEMS and b) corresponding experimental diffraction pattern.

In some cases, both rhombohedral and spinel phases (space group: R-3m and Fd-3m) were detected simultaneously due to the existence of the bicrystal as shown in BF images

in Fig. 4-20 a). Fig. 4-20 b) are the corresponding DPs acquired from the circled areas in the BF images. In b), the main DP is in the rhombohedral phase zone axis [211], while the spinel phase pattern can be indexed in zone axis <113>. In b), the acquired DP can be indexed with the spinel phase in [441] zone axis (with the simulated pattern in the corner). Some extra spots marked by the arrows can be indexed in the O3 [001] zone axis.

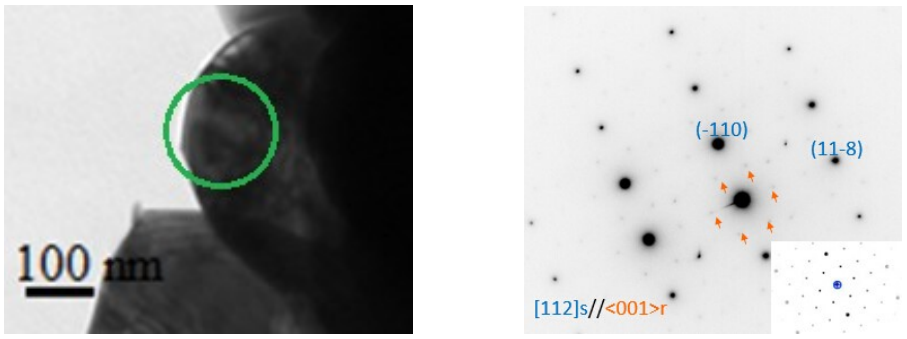

a) b)

Figure 4-20 DPs showing coexistence of both spinel phase and rhombohedral phase (shown in the indexation of the DPs as "s" and "r") in pristine 333 compound. b) main spinel phase in zone axis [112] with rhombohedral phase in zone axis <001>. a) is the corresponding bright field images and the corresponding simulated pattern is in the corner of b).

According to the DPs acquired, both rhombohedral and spinel phases exist in pristine 333 compound. The majority of DPs are shown in rhombohedral phase, which is consistent with the XRD data. In addition, the existence of the alternative spinel phase is proven by the DPs, which corresponds with the extra peak in the XRD pattern. Furthermore, DPs that consist of two sets of patterns representing both R-3m and Fd-3m lattices are also acquired from the bicrystals[52]. The main pattern was shown with high intensity. However, in order to determine if the weak pattern in the different space group is from a different particle or from different domains inside the same primary particles needs further investigation.

4.2.1.3. Comparison between $LiMn_{0.33}Ni_{0.33}Co_{0.33}O_2$ with $LiMn_2O_4$, $LiCoO_2$, and $LiNiO_2$

In the literature[53], $LiMn_{0.33}Ni_{0.33}Co_{0.33}O_2$ is considered a lithium single transition metal oxide, with a mixture of transition metal species in the corresponding layer.

Therefore, it is relevant to compare the structure of the 333 compound with other triple-element-oxide compounds, such as LMO, LCO and LNO, to give a better understanding of the formation of its structure. All samples of three compounds were prepared in the same way as 333 compound. Fig. 4-21 shows TEM BF images of all four compounds and their tendency to agglomerate and form clusters. LCO [shown in Fig. 4-21 b)] has an analogous particle morphology to 333 compound [shown in Fig. 4-21 a)]. The dark appearance in both images indicate the presence of thicker particles if compared to LNO and LMO [shown in Fig. 4-21 c) and d], respectively]. On the other hand, LNO and LMO particles tend to have smaller sizes and possibly higher tendency to agglomerate when compared with the 333 compound and LCO. Furthermore, LNO consists of edged particles while all other compounds are spherical-shaped.

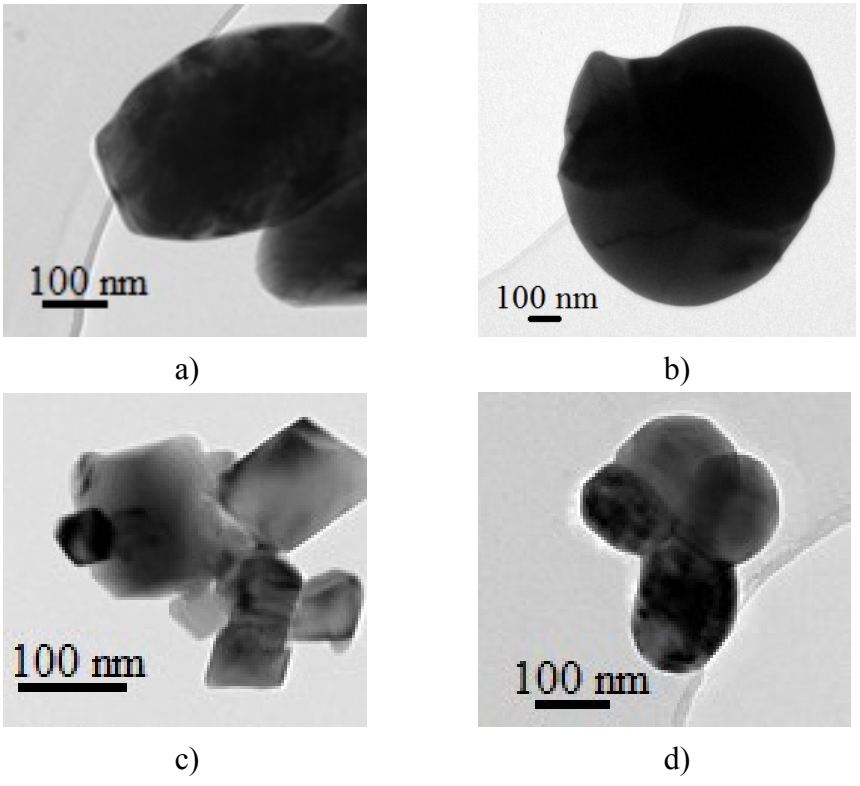

a) b)

c) d)

Figure 4-21 TEM BF images of agglomerated particles of a) 333 compound, b) LCO, c) LNO, and d) LMO.

The crystal structure of all four compounds are shown in Fig. 4-22, based on the ICSD database. As explained in 4.2.1 (XRD), the space group of 333 compound is R-3m in a layered structure, which is identical to LCO, LNO (ICSD), and therefore similar structural characteristics should be observed. On the other hand, LMO has a spinel structure in Fd-3m space group. Since Mn, Ni and Co have similar atomic radii and electron distribution of the ion, small portion of spinel phase domains are present in LCO and LNO, as well as the 333 compound. Therefore, generally in the 333 compound, Mn, Ni and Co are mixed in the transition metal layer and form similar structure with LCO and LNO: major rhombohedral phase in combination with minor spinel phase.[1] Particularly, there is a cation-mixing phenomenon: small portion of Li and Ni ions switch their atomic positions in Li and transition metal layers due to similar radii in LNO[54]. The 333 compound structure undergoes the same as shown in the Fig. 4-22 below. The occupancy of Li and Ni ions represents the same phenomenon in Table 4-12.

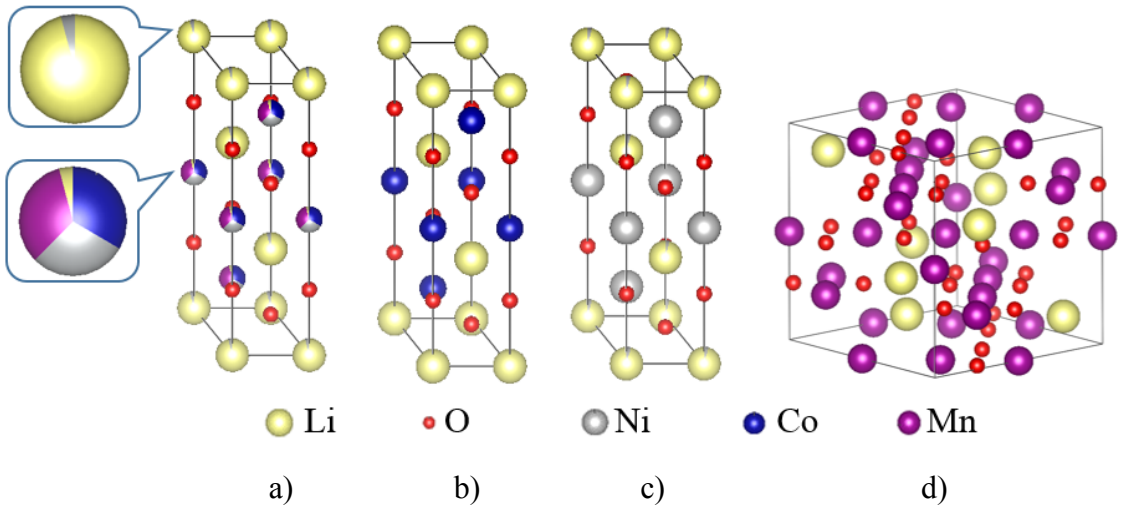

Figure 4-22 The schematic structure of a) 333 compound, b) LCO, c) LNO, and d) LMO crystalline structures. The magnified figures show the ion mixing phenomenon of Li and Ni cations in a) 333 compound and c) LNO.

LCO structural information determined from DPs is shown in Fig. 4-23. Usually, the patterns can be indexed in the rhombohedral R-3m space group, as shown in Fig. 4-23 a)

and b) which are related to different zone axes. Occasionally, some spinel phases in LCO can be indexed in Fd-3m space group, as in Fig. 4-23 c). Due to similar structure, the indexed DPs of LNO were also from both phases (not shown). On the other hand, in LMO, only Fd-3m space group was found and indexed, seen in Fig. 4-23. Secondary diffraction was also present and thus intensity parameters were not considered in the indexation of selected area diffraction patterns.

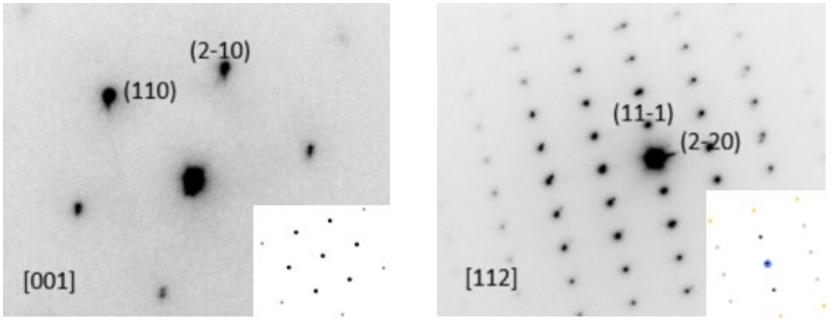

a) b)

Figure 4-23 In LCO particles, most of the DPs acquired are in rhombohedral phase, as a) [001] zone axis. However, there are some spinel phase found as well, as b) in [112] zone axis. All the corresponding simulated patterns are shown in the corner.

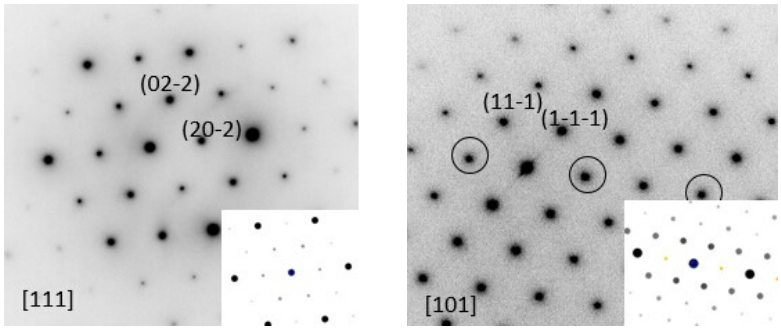

a) b)

Figure 4-24 The DPs of LMO particles with the space group Fd-3m, zone axes of a) [111] and b) [101]. All the simulated DPs are shown in the corner. Particularly in b), the yellow dots in the simulated pattern come from the double diffraction, which corresponds to the circled dots in the real DP.

In all, the 333 compound crystal structure could be considered analogous to the structures of LCO and LNO, which explains most DPs identified as rhombohedral phase in space group R-3m. Occasionally, some spinel phases in space group Fd-3m were observed, indicating similarity to the LMO crystal structure, which consists of this phase.

4.2.2. Structural comparison of non-cycled and cycled $LiMn_{0.33}Ni_{0.33}Co_{0.33}O_2$

Fig. 4-25 compares the morphology between the non-cycled and cycled 333 compound with different number of cycles. A comparison between the particles in a) pristine 333 compound, b) 333 compound after 10 cycles and c) after 50 cycles shows that there are not significant differences in size or shape.

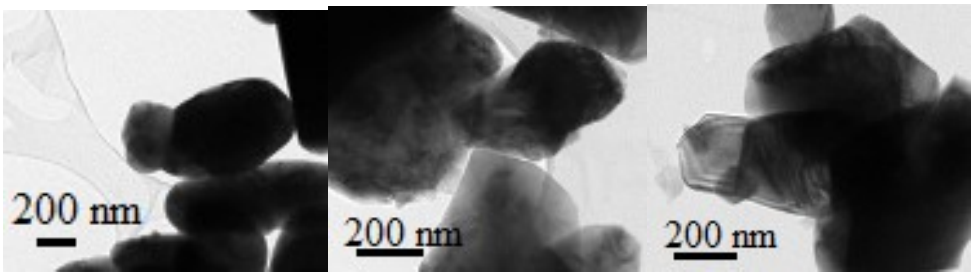

a) b) c)

Figure 4-25 BF-TEM images of a) pristine 333 compound, b) after 10 cycles and c) after 50 cycles. The images demonstrate the transformation of a spherical to sharp edged particles as the number of cycles increase.

DPs were acquired for samples of the 333 compound that underwent 1, 10, 20, and 50 cycles and our analyses indicated that R-3m space group layered rhombohedral phase was still identified in all samples, as indicated partially in Fig. 4-26. In addition, the spinel phases were also observed in the cycled NMC samples (images not shown). The most commonly found zone axis in the rhombohedral phase is [001], and usually there is no superlattice for the pristine 333 compound (Fig. 4-18 above). However, after 20 cycles [shown in Fig. 4-26 a)], extra spots are visible (and are indicated with the arrows) and can be related to the forbidden {100} reflections due to the loss of Li ions. This is explained by

the disturbance of the rhombohedral symmetry of the phase[52], and they disappeared after aging of the 333 compound. Therefore, both aging and cycling can result in the deterioration of the rhombohedral symmetry. After 50 cycles, no more extra spots were found in the DP anymore [Fig. 4-26 b)]. One possible explanation might be the completion of transformation from R-3m lattice to the P-3m1 lattice.

Although the O1 phase was not found in the pristine 333 compound, it was identified in the samples that underwent cycling. The O1 phase appeared more often in the samples that underwent a higher number of cycling and the appearance and consequent growth can be related to the degradation of the battery. The appearance of the O1 phase was observed by another group[32]. Neutron diffraction and X-ray diffraction have been mainly used in combination with electrochemical analysis to determine the formation of new phases. In our project, the experimental DPs of the cycled samples indicating the presence of O1 phases are shown in Fig. 4-27 a) and b), embedded with the simulated DPs.

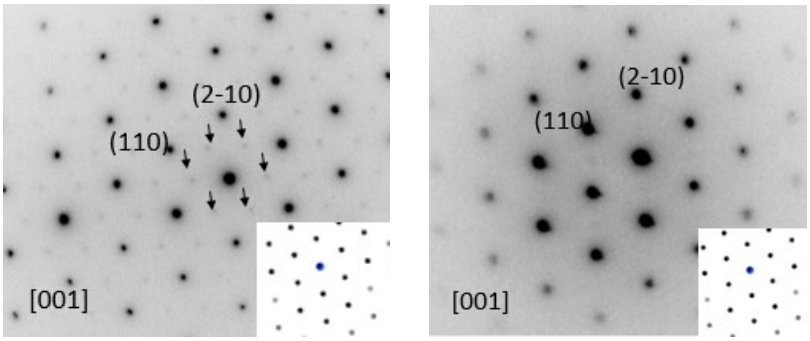

a) b)

Figure 4-26 DP from the 333 compound after a) 20 cycles and b) 50 cycles, indicating the same space group R-3m as in the pristine sample in zone axis [001].

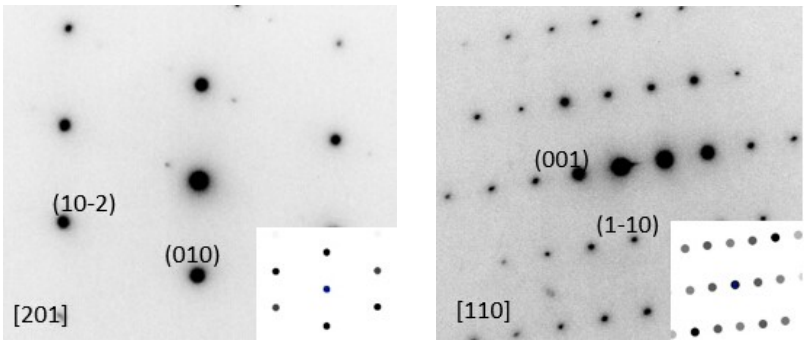

a) b)

Figure 4-27 The DPs in the P-3m1 space group from particles of a) 333 compound after 1 cycle, [201] zone axis; and b) after 20 cycles, [110] zone axis. Corresponding simulated patterns are shown in the corner.

As explained in section 2.3.1, the O1 phase formation can be related to the charging-discharging process, in which most of the cathode materials maintain the reversible R-3m lattice. However, a portion of the particles transform to the irreversible O1 phase, and therefore, partial capacity is lost. The higher number of cycles is related to the growth of the O1 phase, which finally leads to the failure of the battery[32]. In our samples cycled for 50 times with a voltage range between 2.0V and 4.6V and charging rate of C/10, most of the batteries died and were not rechargeable.

Finally, for each of the analyzed samples, approximately 10 to 20 DPs were acquired and indexed to analyze the local structural changes. This means that it is possible we overlooked additional phases and structural differences to fully understand the processes involved during cycling. The data-base may not be sufficient for statistical analysis and significance. Therefore, more investigation using selected area diffraction patterns could be used to give statistical conclusion. In addition, other techniques can be used to support the results acquired from DPs, such as Convergent Beam Electron Diffraction (CBED).

4.2.3. Structural analysis of pristine $Li_{1.2}Mn_{0.54}Ni_{0.13}Co_{0.13}O_2$

A BF-TEM image demonstrating the morphology of pristine $Li_{1.2}Mn_{0.54}Ni_{0.13}Co_{0.13}O_2$ is shown in Fig. 4-28. The primary particles are seen as clusters and the edges are sharper

as compared to the pristine 333 compound, while the size of the particles are approximately the same (Fig. 4-17).

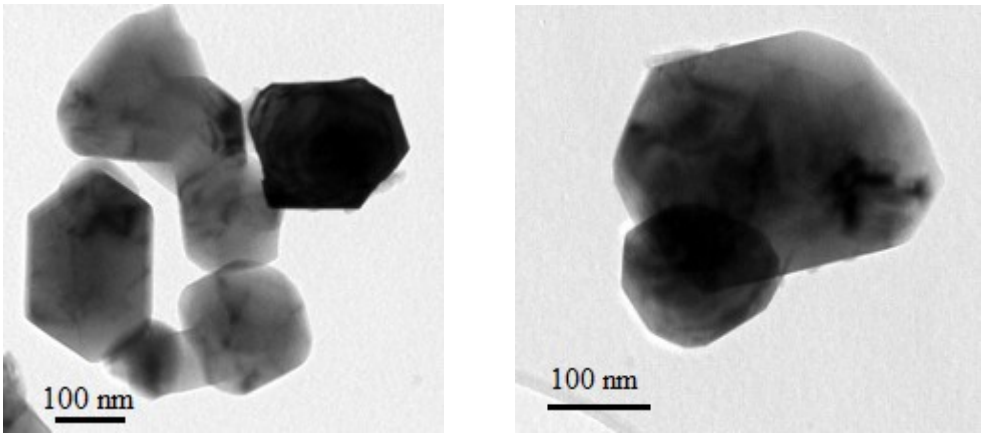

Figure 4-28 BF-TEM image of pristine $Li_{1.2}Mn_{0.54}Ni_{0.13}Co_{0.13}O_2$. a) big clusters of primary particles; and b) small clusters of primary particles.

Since the $Li_{1.2}Mn_{0.54}Ni_{0.13}Co_{0.13}O_2$ (HENMC) structure consists of both pristine 333 compound lattice and Li_2MnO_3 lattice, both trigonal and monoclinic space groups can be found among different domains. Moreover, since the Li and Mn rich phase (Li_2MnO_3) possesses a higher cation ordering than 333 compound[38], superlattice extra spots were found in almost all of the DPs in the pristine HENMC. This phenomenon corresponds to the extra superlattice peaks found in the range of 21–25° from an XRD pattern, which the authors relate to the highly ordered Li cations present in the transition metal layer[35]. With the increase of Li_2MnO_3 content, the intensity of superlattice reflection peak (020) increases significantly[38].

The DP shown in Fig. 4-29 a) was identified as rhombohedral phase in R-3m space group in zone axis [001]. There are extra diffraction spots with weak brightness located in the 1/3 and 2/3 positions between the fundamental spots, indicating the existence of a $\sqrt{3}a_{hex}\times\sqrt{3}a_{hex}$ superstructure in which all transition metal and Li-ions are located regularly in the transition metal layer as demonstrated in the schematic Fig. 4-29 b) [2]. As explained in section 2.3.2, there are α and β sites which suit ions with different sizes; Li^+ and Ni^{2+} ions usually fit in the α sites, while the Mn^{4+} and Co^{3+} ions can be inserted in the β sites. The ratio between these two sites are: α : β = 1 : 2 [33] which means that according to the

composition of $Li_{1.2}Mn_{0.54}Ni_{0.13}Co_{0.13}O_2$, it is more likely to encounter superlattice structure in nanoscale when compared to $LiMn_{0.33}Ni_{0.33}Co_{0.33}O_2$.

In fact, the ratio between the large (Li^+, Ni^{2+}) and small (Mn^{4+}, Co^{3+}) cations inside the transition metal layer determines the superlattice intensity[33]. The further the ratio deviates from 1, the higher the contrast between these spots with the fundamental spots. Therefore, a higher intensity ratio between the superlattice spots and fundamental reflections can be achieved with over lithiation[55]. Actually, this can be seen in the DPs, in almost all the HENMC DPs superlattice spots are clearly visible (Fig. 4-29), while these spots were rarely seen in 333 compound (Fig. 4-23).

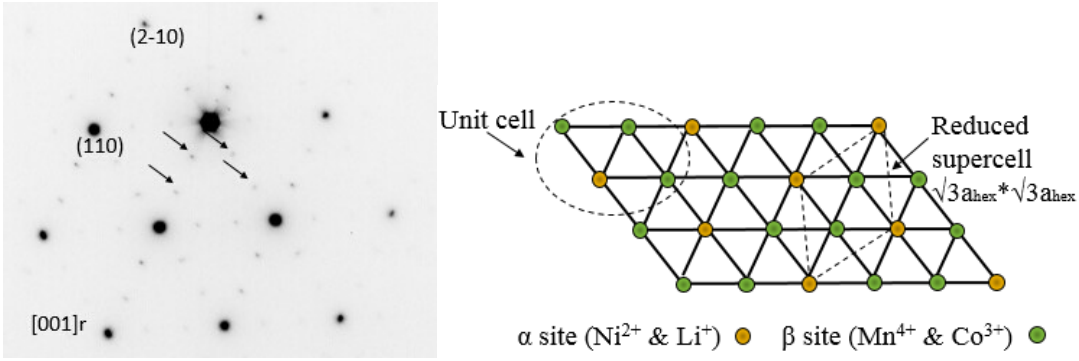

a) b)

Figure 4-29 a) DP in zone axis [001] of R-3m space group with superlattice spots in the 1/3 and 2/3 position between fundamental spots (indicated with arrows), and b) corresponding structural representation of the distribution of α and β sites in an ordered transition metal layer.

Monoclinic phases are also present in the pristine HENMC, shown in Fig. 4-30. Although there appears to be one particle in the BF-TEM image shown in Fig. 4-30 a), in Fig. 4-30 b), the circled DP spots with weak intensity belongs to a different pattern comparing to the main DP spots with strong intensity. That is to say, the DP contains more than one set of patterns, meaning that there are at least two different crystals. The main pattern in c) was indexed in the [001] zone axis with C2/m monoclinic phase and extra spots found between this pattern is related to a superlattice structure (indicated with arrows).

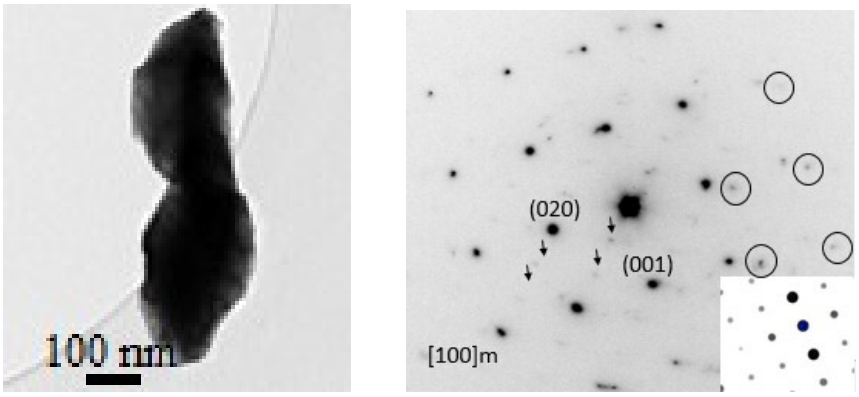

a) b)

Figure 4-30 a) BF-TEM image of two pristine HENMC particles and b) the DP, in zone axis [001] space group C2/m with superlattice spots.

A BF-TEM image of a (HENMC) particle is shown in Fig. 4-31, with its corresponding DP. This pattern shows a new feature: fine streaks are visible between the fundamental spots and are indicated with arrows in Fig.4-31 e). The main space group of this DP is in R-3m with zone axis [210] [Fig. 4-31 a)] without considering the streaks. It would be challenging to index the diffuse streaks, however, some extra elongated spots (circled) along the streaks can be indexed by the C2/m space group within [110] zone axis [Fig. 4-31 b)]. This phenomenon can be explained by the superposition of the Li_2MnO_3 monoclinic structure along the rhombohedral phase. Therefore, the particle shown has a combined crystal structure of space group R-3m [210] and C2/m in [110] zone axis.

The appearance of the streaks is along [210] zone axis. According to Jarvis[40], the structure in these regions might consist of many monoclinic nanoscale platelets with various orientations. These platelets are produced by the displacement of the planes along different directions. These planar defects might cause the streaking in the DP. In addition, streaks or elongated spots might be from the thin-plate-shaped regions as well[56].

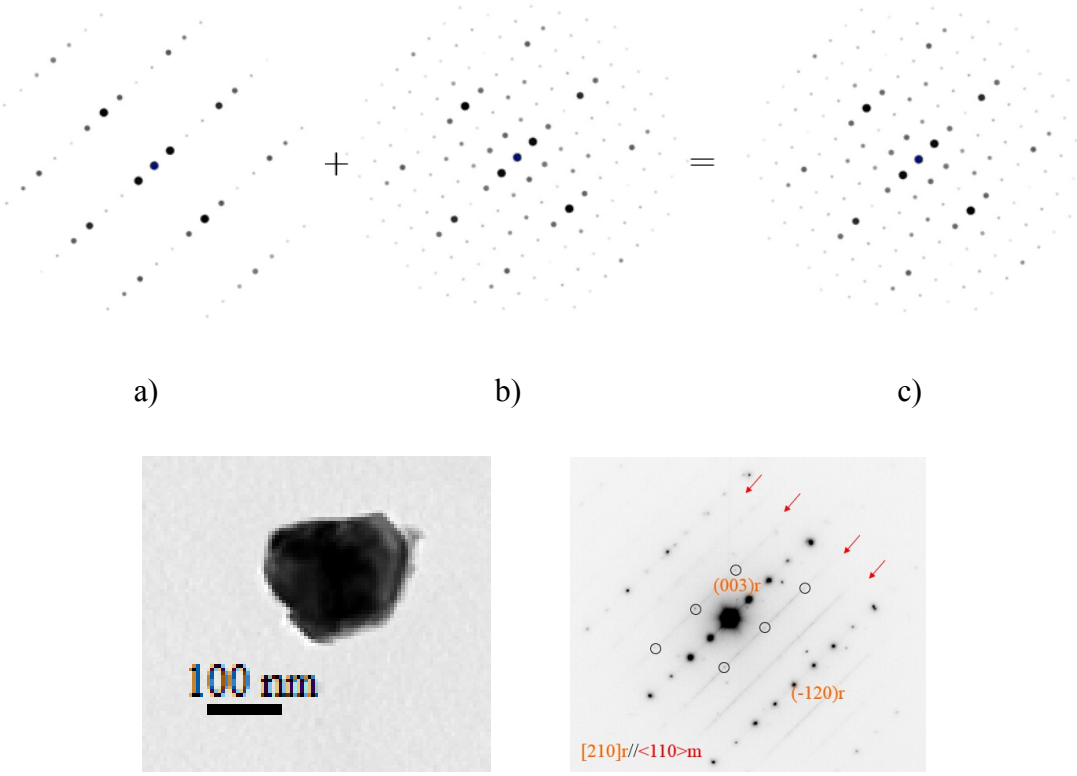

Figure 4-31 Simulated DPs a) and b) are combined to form c) which is used to index DP e) with streaks, and the corresponding BF-TEM image is d). The main zone axis is a) R-3m [210] with extra patterns b) C2/m [110] zone axes. Particularly in the indexation of e), "r" and "m" represents rhombohedral and monoclinic phases.

The DP shown below in Fig. 4-32 e) (with corresponding BF-TEM image shown in d) is indicative of a twin-like structure due to the overlap of the simulated patterns shown in Fig. 4-32 a) and b), which forms c). Since the spots pointed by the arrows are distinct and elongated, there could be two sets of patterns overlapping acquired from two lattice regions instead of real twin structure from one lattice. The two *c* axes were in different directions, and they are on top of each other. Therefore, the DP can be seen as a twin-like structure[57].

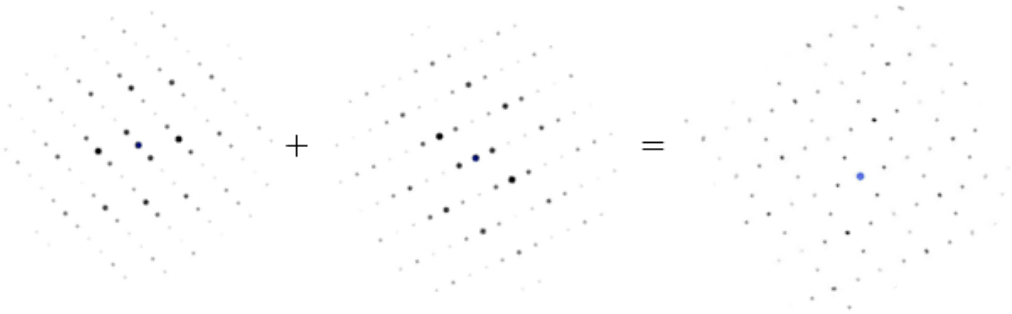

a) b) c)

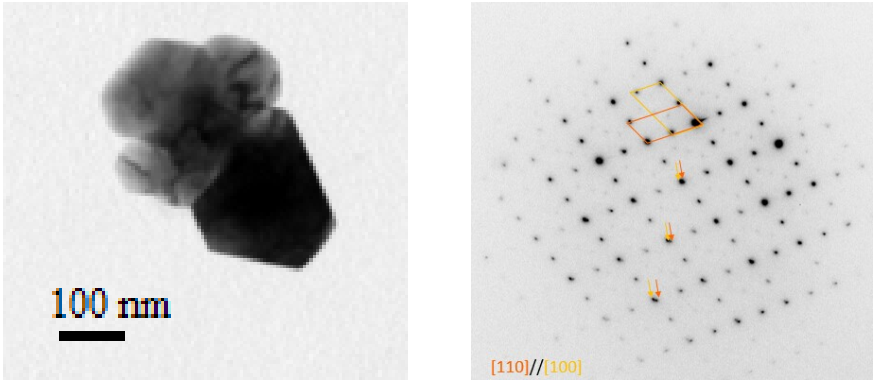

d) e)

Figure 4-32 The DP e) with twin-like structure which can be simulated by c) which is formed by R-3m zone axes a) [110] and b) [100]. The corresponding BF-TEM image is d).

4.2.4. Structural comparison of non-cycled and cycled $Li_{1.2}Mn_{0.54}Ni_{0.13}Co_{0.13}O_2$

The BF-TEM images in Fig. 4-33 shows the morphology changes from pristine HENMC (shown in a)) to HENMC after 50 cycles (shown in b)) and after 100 cycles (shown in c)). There isn't a noticeable difference between the morphology in the first two cases. However, for the sample cycled 100 times, there is a thick layer with light color that might be the solid electrolyte interphase as explained in section 4.1.2, and could explain why the battery does not work with high efficiency and capacity after extensive cycling.

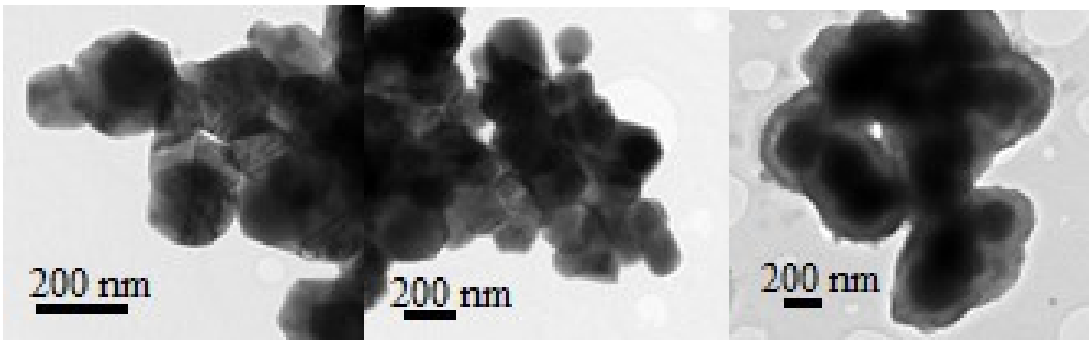

a) b) c)

Figure 4-33 The BF-TEM images of a) pristine, b) after 50 cycles, and c) after 100 cycles of HENMC particles. There is a distinct morphology difference between the pristine and particles after 100 cycles, indicating the potential formation of SEI layer.

For the cycled samples, the most significant difference is the absence of superlattice structure identified in most DPs. Moreover, the appearance of spinel phases was also observed in the cycled HENMC samples, being identified more frequently with higher number of cycles. Although the monoclinic phase transforms from the spinel phase[58], the monoclinic phase was still identified in the sample after 50 cycles. This indicates that the transformation does not occur homogenously but rather in different domains inside the agglomerated primary particles.

The DPs acquired from the pristine HENMC, cycled 1 and 50 times are shown in Fig. 4-34 and all were identified as a rhombohedral phase in space group R-3m with a zone axis [001]. The pristine HENMC DPs are shown in Fig. 4-34 a) and b) and high resolution of superlattice spots between the fundamental spots (pointed with arrows) can be observed. For the 1 cycle sample, the extra superlattice spots were much dimmer in the same exposure time, indicating a loss of ordering inside the transition metal layer. Moreover, the appearance of the forbidden reflections in the [100] zone axis (shown in circles) were observed. In some cases no superlattice spots were observed (Fig. 4-34 d). Instead, only forbidden reflections were identified, indicating the disturbance of structural stability. For the sample cycled 50 times, there were three phases in coexistence which are shown in Fig. 4-34 e) and f): monoclinic [111], spinel [001] and rhombohedral [001], also seen in

Mohanty's work [1]. In e) the existence of spinel and monoclinic phases is blurred, but in f) the coexistence of three phases are clearly shown and identified.

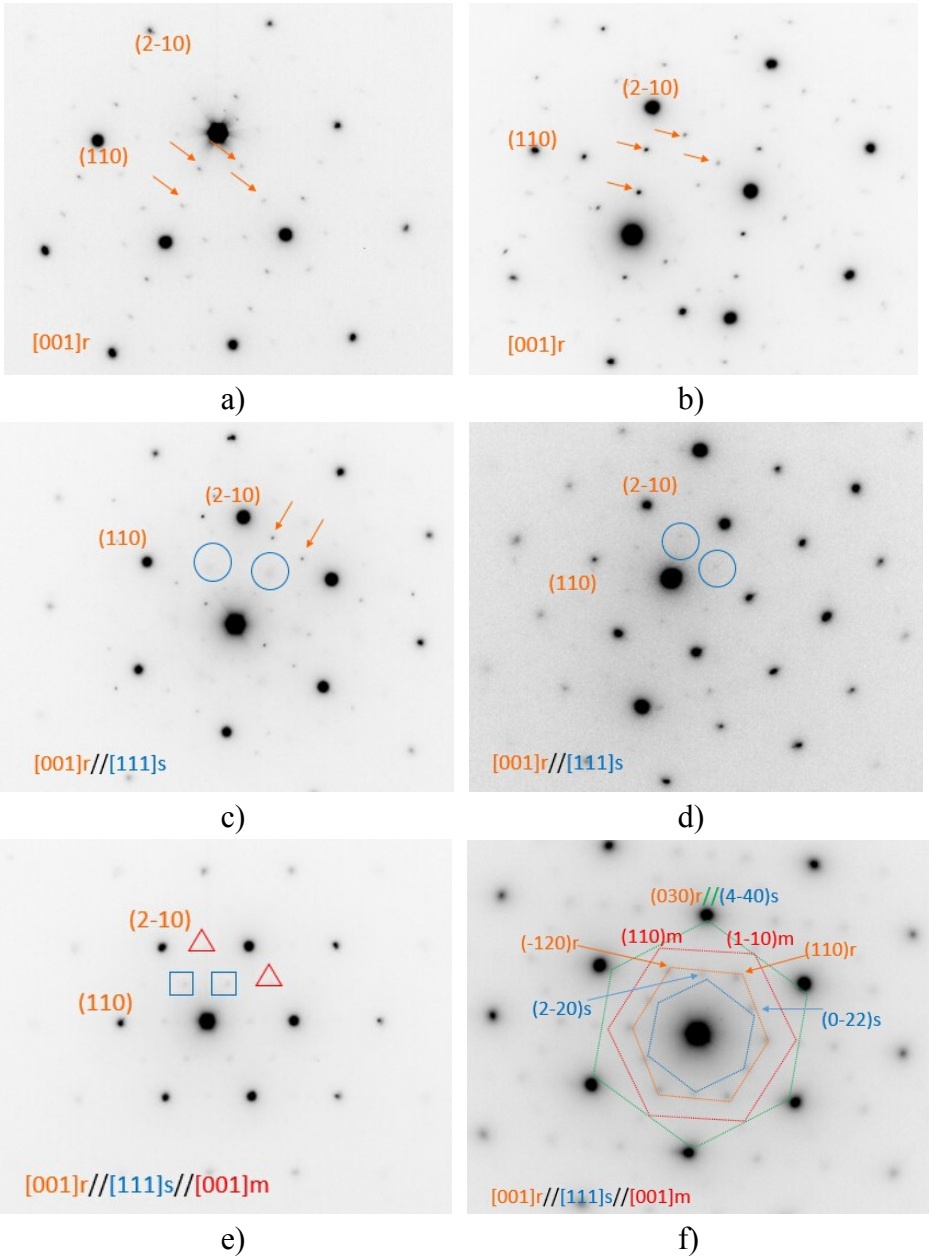

Figure 4-34 All the DPs are mainly in R-3m space group with [001] zone axis. They are from particles of a), b) a pristine HENMC; c), d) HENMC after 1 cycle, and e), f) after 50 cycles. Only R-3m fundamental spots and extra superlattice spots are shown in a) and b). In c) and d), loss of superlattice from rhombohedral phase and the appearance of spinel

phase can be found. After 50 cycles in e) and f), rhombohedral, monoclinic and spinel phases (shown in the indexation as “r”, “m” and “s”) were all identified.

DPs belonging to the pristine and cycled HENMC with monoclinic phase are shown in Fig. 4-35. All DPs are from the zone axis [001] in C2/m monoclinic phase. Extra superlattice spots between the main spots were found and are indicated with arrows. After 1 cycle with a similar exposure time as for the pristine sample (Fig. 4-35 b), the two extra spots are absent. Instead, new extra spots were identified (shown with an arrow), indicating the presence of the forbidden reflections in the middle of the two fundamental spots. One of the extra spots is identified from the appearance of the spinel phase [shown in Fig. 4-35 b) and c)][56]. After 50 cycles (Fig. 4-35 c), no superlattice spots are visible and several more DPs with spinel phases are present. However, there are totally 12 DPs for each sample so this cannot represent statistical results.

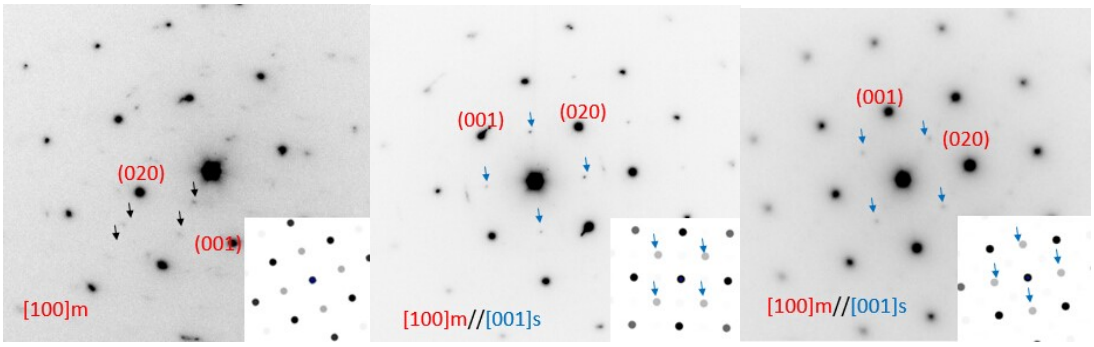

a) b) c)

Figure 4-35 DP in C2/m space group with [001] zone axis, showing the loss of superlattice from monoclinic phase and the increase of spinel phase from particles of a) pristine HENMC, b) 1 cycle HENMC, c) 50 cycles HENMC.

In the DP of the pristine HENMC (shown in Fig. 4-36 a) more spots in the three-times-periodicity are present with streaks. Indexation determined one of the sports to be from the main rhombohedral phase and the other two due to monoclinic phases. Two-times-periodicity streaks, related to the formation of spinel structure, were identified in the

sample cycled 1 time (shown in Fig. 4-36 b). Moreover, according to Fig. 4-36 c), which is HENMC after 50 cycles, the intensity of the spots and streaks from the spinel phase was similar to the HENMC after 1 cycle, indicating that most of the transformation might be completed during the first cycle. However, even though most of the monoclinic phases is transformed into spinel phase after 50 cycles, there were still some monoclinic phases left, according to Ito[57]. In all, cycling of HENMC particles results in the appearance of the two-times-periodicity spots and the three-times-periodicity spots become dimmer. This means that spinel phases were formed from the monoclinic phases during the 1st cycle and the structure experienced insignificant changes after 50 cycles.

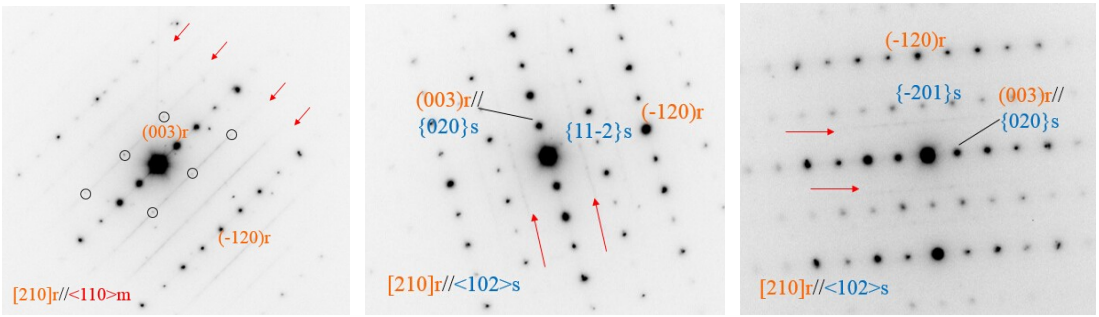

a) b) c)

Figure 4-36 DPs with streaks are from particles of a) pristine HENMC, b) 1 cycle HENMC, c) 50 cycles HENMC; main zone axis of all three DPs is R-3m [210]. a) with extra C2/m [110] and [100] zone axes; b) and c) with extra Fd-3m [111] zone axis.

In certain DPs the distance between fundamental spots are evenly distributed in a 6-fold symmetry. There are only 3 visible spots in the 1/3, 1/2 and 2/3 positions between two fundamental spots due to the intensity. These “triplets” are an indication of higher ordering, as shown in Fig. 4-37 a) in the twin-like structures. After cycling, most of the superlattice spots disappear [Fig. 4-37 b)], which means that this cation arrangement is not energetically favorable[52] and less cation ordering exists in the rhombohedral phase.

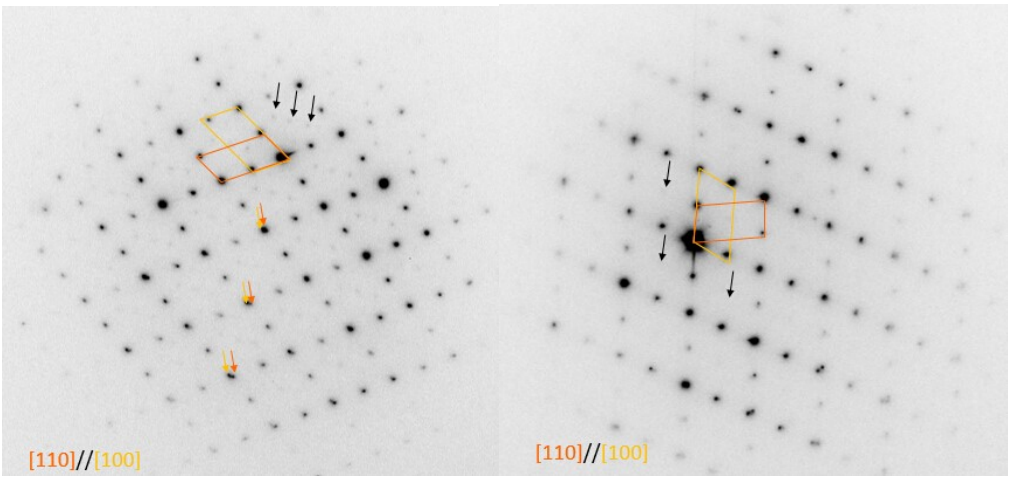

a) b)

Figure 4-37 DPs with twin-like structures, a) pristine HENMC, b) HENMC after 1 cycle. Both of them have phases from R-3m space group, zone axes [110] and [100].

In pristine $Li_{1.2}Mn_{0.54}Co_{0.13}Ni_{0.13}O_2$, both rhombohedral and monoclinic phase were identified, separately, in the DPs. After the 1st cycle, the spinel phase $LiMn_2O_4$ was also identified, which was converted from monoclinic phase Li_2MnO_3. After the 50th cycle, more spinel phases were found, however, with a monoclinic phase residue. The final oxide structure consists of a mixture of layered hexagonal, layered monoclinic and spinel phases, which were shown from Fig. 4-34 e) and f). In addition, the superlattice reflections in the rhombohedral phase gradually disappear which shows that this phase is not energetically favorable. After the 100th cycle, potential thick solid-electrolyte layer was formed indicating deterioration of the battery.

A series of structural difference were observed by the comparison of two compounds with different compositions: $LiMn_{0.33}Co_{0.33}Ni_{0.133}O_2$ and $Li_{1.2}Mn_{0.54}Co_{0.13}Ni_{0.13}O_2$. In the 333 compound, the switch of atomic positions between Li and Ni ions leads to a loss of capacity and lithium diffusion reduction. With more stoichiometric introduction of Li ions in HENMC, extra Li ions are inserted into the transition metal layer contributing to the partial reason of the increased capacity and energy density during cycling. Furthermore, in the 333 compound, superlattice reflections are supposed to appear due to the cations ordering in transition metal layer, however, this was proven wrong and transition metals

are randomly distributed. On the contrary, in HENMC, with the introduction of a large portion of Li in the transition metal layer, superlattice were observed often indicating the higher stability of the cathode material.[2]

On the other hand, more Mn and less Co/Ni also result in significant changes. Within HENMC, monoclinic phases $LiMnO_3$ were identified, in combination with 333 compound in the rhombohedral phase. During cycling of HENMC, the transformation of 333 compound from R-3m space group to P-3m1 were not observed, which is the main deterioration mechanism in the pure 333 compound. While during the first HENMC cycles, monoclinic phases change to spinel phases. After 100 cycles, the potential SEI layer was formed and the battery performed poorly, so significant structural variation of the whole battery system occur during the extra 50 cycles. Therefore, the change of composition results in the change of deterioration process as well, and further investigations on HENMC between 50 cycles and 100 cycles are needed.

Ch 5. Conclusions and Future work

Conclusions

In this project, a systematic compositional characterization of Li-ion battery cathode material $LiMn_{0.33}Ni_{0.33}Co_{0.33}O_2$ and $Li_{1.2}Mn_{0.54}Ni_{0.13}Co_{0.13}O_2$ were performed to explore the most reliable quantification method and the appropriate procedure for quantification. The compositional and structural change following long electrochemical cycling was also explored for these materials, as well as changes caused by ball milling for electron microscopy.

First, optimal procedures of compositional quantification were tested. Stable and more reliable quantification of EDS data can only be achieved by stringent preparation of samples, appropriate standards and optimizing acquisition parameters. In terms of AES, the optimal operating conditions for quantification with AES were investigated with the use of different combination of standards. Consequently, the reliable micron-scale quantification procedures to determine the composition of NMC nanoparticles, using EDS and AES, were determined.

Second, the phase changes of HENMC during cycling were investigated with AES and TEM based DPs. In the original HENMC, both rhombohedral and monoclinic phase were found, separately. After the 1st cycle, the spinel phase $LiMn_2O_4$ was found, which was converted from the monoclinic phase Li_2MnO_3. After the 50th cycle, more spinel phase was found, however, there is always a spinel phase residue. In addition, the superlattice reflections in the rhombohedral phase gradually disappeared, thus indicating that this phase is not energetically favorable. After the 100th cycle, a thick solid-electrolyte layer was formed indicating deterioration of the battery.

Finally, the phase changes of the 333 compound during cycling were supported by AES and TEM based DPs. Most domains of the original 333 compound has the same layered rhombohedral phase as the LCO and LNO phases, and small portion of other domains have the spinel phase as LMO. With more and more cycling, the 333 compound gradually exhibits more O1 phase domains, while the majority domains are still O3 phase. After ball milling, the performance of the corresponding cathode did not perform well due to the reduce density of paths for Li-ions to transfer.

Future work

Whether alternative samples (except for the 333 compound or HENMC) with different stoichiometric compositions can provide better battery performance is still of interest. Moreover, the change in compositions and structures of these compounds are to be explored before and after cycling.

In all, the composition of the optimal NMC materials is still under exploration, and more systematic studies of the original material after cycling need to be further undertaken to understand the degradation process of these materials in different conditions.

Appendix I $LiMn_{0.33}Ni_{0.33}Co_{0.33}O_2$ O3 phase CIF file

data_171750-ICSD

_database_code_ICSD 171750

_audit_creation_date 2006-10-01

_audit_update_record 2013-02-01

_chemical_name_systematic

'Lithium cobalt nickel manganese oxide (1/0.33/0.33/0.33/2)'

_chemical_formula_structural 'Li Co0.333 Ni0.333 Mn0.333 O2'

_chemical_formula_sum 'Co0.333 Li1 Mn0.333 Ni0.333 O2'

_chemical_name_structure_type NaCrS2

_exptl_crystal_density_diffrn 4.77

_publ_section_title

;

X-ray/neutron diffraction and electrochemical studies of lithium

de/re-intercalation in Li(1-x) Co(1/3) Ni(1/3) Mn(1/3) O2 (x = 0 - 1)

;

loop_

_citation_id

_citation_journal_full

_citation_year

_citation_journal_volume

_citation_page_first

_citation_page_last

_citation_journal_id_ASTM

primary 'Chemistry of Materials' 2006 18 1901 1910 CMATEX

loop_

_publ_author_name

'Yin, S.-C.'

'Rho, Y.-H.'

'Swainson, I.'

'Nazar, L.F.'

_cell_length_a 2.860(2)

_cell_length_b 2.860(2)

_cell_length_c 14.227(8)

_cell_angle_alpha 90.

_cell_angle_beta 90.

_cell_angle_gamma 120.

_cell_volume 100.78

_cell_formula_units_Z 3

_symmetry_space_group_name_H-M 'R -3 m H'

_symmetry_Int_Tables_number 166

_refine_ls_R_factor_all 0.0295

loop_

_symmetry_equiv_pos_site_id

_symmetry_equiv_pos_as_xyz

1 'x-y, -y, -z'

2 '-x, -x+y, -z'

3 'y, x, -z'

4 'x-y, x, -z'

5 'y, -x+y, -z'

6 '-x, -y, -z'

7 '-x+y, y, z'

8 'x, x-y, z'

9 '-y, -x, z'

10 '-x+y, -x, z'

11 '-y, x-y, z'

12 'x, y, z'

13 'x-y+2/3, -y+1/3, -z+1/3'

14 '-x+2/3, -x+y+1/3, -z+1/3'

15 'y+2/3, x+1/3, -z+1/3'

16 'x-y+2/3, x+1/3, -z+1/3'

17 'y+2/3, -x+y+1/3, -z+1/3'

18 '-x+2/3, -y+1/3, -z+1/3'

19 '-x+y+2/3, y+1/3, z+1/3'

20 'x+2/3, x-y+1/3, z+1/3'

21 '-y+2/3, -x+1/3, z+1/3'

22 '-x+y+2/3, -x+1/3, z+1/3'

23 '-y+2/3, x-y+1/3, z+1/3'

24 'x+2/3, y+1/3, z+1/3'

25 'x-y+1/3, -y+2/3, -z+2/3'

26 '-x+1/3, -x+y+2/3, -z+2/3'

27 'y+1/3, x+2/3, -z+2/3'

28 'x-y+1/3, x+2/3, -z+2/3'

29 'y+1/3, -x+y+2/3, -z+2/3'

30 '-x+1/3, -y+2/3, -z+2/3'

31 '-x+y+1/3, y+2/3, z+2/3'

32 'x+1/3, x-y+2/3, z+2/3'

33 '-y+1/3, -x+2/3, z+2/3'

34 '-x+y+1/3, -x+2/3, z+2/3'

35 '-y+1/3, x-y+2/3, z+2/3'

36 'x+1/3, y+2/3, z+2/3'

loop_

_atom_type_symbol

_atom_type_oxidation_number

Li1+ 1

Co3+ 3

Ni2+ 2

Mn4+ 4

O2- -2

Li1+ 1

Ni2+ 2

loop_

_atom_site_label

_atom_site_type_symbol

_atom_site_symmetry_multiplicity

_atom_site_Wyckoff_symbol

_atom_site_fract_x

_atom_site_fract_y

_atom_site_fract_z

_atom_site_B_iso_or_equiv

_atom_site_occupancy

_atom_site_attached_hydrogens

Li1 Li1+ 3 a 0 0 0 0.0012(3) .975(1) 0

Co1 Co3+ 3 b 0 0 0.5 0.0012(3) .33333 0

Ni1 Ni2+ 3 b 0 0 0.5 0.0012(3) .309(1) 0

Mn1 Mn4+ 3 b 0 0 0.5 0.0012(3) .33333 0

O1 O2- 6 c 0 0 .2411(1) 0.0012(3) 1. 0

Li2 Li1+ 3 b 0 0 0.5 0.0012(3) .025(1) 0

Ni2 Ni2+ 3 a 0 0 0 0.0010(1) .025(1) 0

#End of TTdata_171750-ICSD

Appendix II $LiMn_{0.33}Ni_{0.33}Co_{0.33}O_2$ O1 phase CIF file

data_171755-ICSD

_database_code_ICSD 171755

_audit_creation_date 2006-10-01

_audit_update_record 2013-02-01

_chemical_name_systematic

'Lithium cobalt nickel manganese oxide (0.04/0.33/0.33/0.33/2)'

_chemical_formula_structural 'Li0.04 Co0.333 Ni0.333 Mn0.333 O2'

_chemical_formula_sum 'Co0.333 Li0.04 Mn0.333 Ni0.333 O2'

_chemical_name_structure_type LiTiS2

_exptl_crystal_density_diffrn 4.8

_publ_section_title

;

X-ray/neutron diffraction and electrochemical studies of lithium

de/re-intercalation in Li(1-x) Co(1/3) Ni(1/3) Mn(1/3) O2 (x = 0 - 1)

;

loop_

_citation_id

_citation_journal_full

_citation_year

_citation_journal_volume

_citation_page_first

_citation_page_last

_citation_journal_id_ASTM

primary 'Chemistry of Materials' 2006 18 1901 1910 CMATEX

loop_

_publ_author_name

'Yin, S.-C.'

'Rho, Y.-H.'

'Swainson, I.'

'Nazar, L.F.'

_cell_length_a 2.8269(4)

_cell_length_b 2.8269(4)

_cell_length_c 4.4894(6)

_cell_angle_alpha 90.

_cell_angle_beta 90.

_cell_angle_gamma 120.

_cell_volume 31.07

_cell_formula_units_Z 1

_symmetry_space_group_name_H-M 'P -3 m 1'

_symmetry_Int_Tables_number 164

_refine_ls_R_factor_all 0.0514

loop_

_symmetry_equiv_pos_site_id

_symmetry_equiv_pos_as_xyz

1 'x-y, -y, -z'

2 '-x, -x+y, -z'

3 'y, x, -z'

4 'x-y, x, -z'

5 'y, -x+y, -z'

6 '-x, -y, -z'

7 '-x+y, y, z'

8 'x, x-y, z'

9 '-y, -x, z'

10 '-x+y, -x, z'

11 '-y, x-y, z'

12 'x, y, z'

loop_

_atom_type_symbol

_atom_type_oxidation_number

Co3+ 3

Ni3+ 3.56

Mn4+ 4

O2- -2

Ni4+ 4.88

Li1+ 1

loop_

_atom_site_label

_atom_site_type_symbol

_atom_site_symmetry_multiplicity

_atom_site_Wyckoff_symbol

_atom_site_fract_x

_atom_site_fract_y

_atom_site_fract_z

_atom_site_B_iso_or_equiv

_atom_site_occupancy

_atom_site_attached_hydrogens

Co1 Co3+ 1 a 0 0 0 0.007(1) .3333 0

Ni1 Ni3+ 1 a 0 0 0 0.007(1) .307(4) 0

Mn1 Mn4+ 1 a 0 0 0 0.007(1) .33333 0

O1 O2- 2 d 0.3333 0.6667 0.2186(5) 0.008(1) 1. 0

Ni2 Ni4+ 1 b 0 0 0.5 0.007(1) .026(4) 0

#End of TTdata_171755-ICSD

Appendix III Li_2MnO_3 CIF file

data_165686-ICSD

_database_code_ICSD 165686

_audit_creation_date 2010-02-01

_audit_update_record 2013-08-01

_chemical_name_systematic 'Dilithium manganate(IV)'

_chemical_formula_structural 'Li2 (Mn O3)'

_chemical_formula_sum 'Li2 Mn1 O3'

_chemical_name_structure_type Li2MnO3

_exptl_crystal_density_diffrn 3.89

_publ_section_title

;

Reinvestigation of Li2 Mn O3 structure: electron diffraction and high

resolution TEM

;

loop_

_citation_id

_citation_journal_full

_citation_year

_citation_journal_volume

_citation_page_first

_citation_page_last

_citation_journal_id_ASTM

primary 'Chemistry of Materials' 2009 21 4216 4222 CMATEX

loop_

_publ_author_name

'Boulineau, A.'

'Croguennec, L.'

'Delmas, C.'

'Weill, F.'

_cell_length_a 4.9292(2)

_cell_length_b 8.5315(2)

_cell_length_c 5.0251(1)

_cell_angle_alpha 90.

_cell_angle_beta 109.337(2)

_cell_angle_gamma 90.

_cell_volume 199.4

_cell_formula_units_Z 4

_symmetry_space_group_name_H-M 'C 1 2/m 1'

_symmetry_Int_Tables_number 12

_refine_ls_R_factor_all 0.078

loop_

_symmetry_equiv_pos_site_id

_symmetry_equiv_pos_as_xyz

1 '-x, y, -z'

2 '-x, -y, -z'

3 'x, -y, z'

4 'x, y, z'

5 '-x+1/2, y+1/2, -z'

6 '-x+1/2, -y+1/2, -z'

7 'x+1/2, -y+1/2, z'

8 'x+1/2, y+1/2, z'

loop_

_atom_type_symbol

_atom_type_oxidation_number

Li1+ 1

Mn4+ 4

Li1+ 1

Mn4+ 4

Li1+ 1

Mn4+ 4

O2- -2

loop_

_atom_site_label

_atom_site_type_symbol

_atom_site_symmetry_multiplicity

_atom_site_Wyckoff_symbol

_atom_site_fract_x

_atom_site_fract_y

_atom_site_fract_z

_atom_site_B_iso_or_equiv

_atom_site_occupancy

_atom_site_attached_hydrogens

Li1 Li1+ 2 b 0 0.5 0 1. 0.854(4) 0

Mn1 Mn4+ 2 b 0 0.5 0 1. 0.146(4) 0

Li2 Li1+ 2 c 0 0 0.5 1. 1. 0

Li3 Li1+ 4 h 0 0.681(2) 0.5 1. 0.986(3) 0

Mn2 Mn4+ 4 h 0 0.681(2) 0.5 1. 0.014(3) 0

Li4 Li1+ 4 g 0 0.1687(3) 0 0.5 0.087(5) 0

Mn3 Mn4+ 4 g 0 0.1687(3) 0 0.5 0.913(5) 0

O1 O2- 4 i 0.224(2) 0 0.225(1) 0.8 1. 0

O2 O2- 8 j 0.253(1) 0.3230(6) 0.2275(9) 0.8 1. 0

#End of TTdata_165686-ICSD

Appendix IV $LiMn_2O_4$ CIF file

data_50415-ICSD

_database_code_ICSD 50415

_audit_creation_date 1999-11-30

_chemical_name_systematic 'Lithium dimanganese tetraoxide'

_chemical_formula_structural 'Li Mn2 O4'

_chemical_formula_sum 'Li1 Mn2 O4'

_chemical_name_structure_type Al2MgO4

_exptl_crystal_density_diffrn 4.28

_cell_measurement_temperature 295.

_publ_section_title 'A neutron diffraction study of Ni substituted Li Mn2 O4'

loop_

_citation_id

_citation_journal_full

_citation_year

_citation_journal_volume

_citation_page_first

_citation_page_last

_citation_journal_id_ASTM

primary 'Solid State Ionics' 1998 112 165 168 SSIOD3

loop_

_publ_author_name

'Berg, H.'

'Thomas, J.O.'

'Wen, L.'

'Farrington, G.C.'

_cell_length_a 8.251(4)

_cell_length_b 8.251(4)

_cell_length_c 8.251(4)

_cell_angle_alpha 90.

_cell_angle_beta 90.

_cell_angle_gamma 90.

_cell_volume 561.72

_cell_formula_units_Z 8

_symmetry_space_group_name_H-M 'F d -3 m Z'

_symmetry_Int_Tables_number 227

_refine_ls_R_factor_all 0.0558

loop_

_symmetry_equiv_pos_site_id

_symmetry_equiv_pos_as_xyz

1 '-z, y+3/4, x+3/4'

2 'z+3/4, -y, x+3/4'

3 'z+3/4, y+3/4, -x'

4 '-z, -y, -x'

5 'y+3/4, x+3/4, -z'

6 '-y, x+3/4, z+3/4'

7 'y+3/4, -x, z+3/4'

8 '-y, -x, -z'

9 'x+3/4, -z, y+3/4'

10 'x+3/4, z+3/4, -y'

11 '-x, z+3/4, y+3/4'

12 '-x, -z, -y'

13 '-z, x+3/4, y+3/4'

14 'z+3/4, x+3/4, -y'

15 'z+3/4, -x, y+3/4'

16 '-z, -x, -y'

17 'y+3/4, -z, x+3/4'

18 '-y, z+3/4, x+3/4'

19 'y+3/4, z+3/4, -x'

20 '-y, -z, -x'

21 'x+3/4, y+3/4, -z'

22 'x+3/4, -y, z+3/4'

23 '-x, y+3/4, z+3/4'

24 '-x, -y, -z'

25 'z, -y+1/4, -x+1/4'

26 '-z+1/4, y, -x+1/4'

27 '-z+1/4, -y+1/4, x'

28 'z, y, x'

29 '-y+1/4, -x+1/4, z'

30 'y, -x+1/4, -z+1/4'

31 '-y+1/4, x, -z+1/4'

32 'y, x, z'

33 '-x+1/4, z, -y+1/4'

34 '-x+1/4, -z+1/4, y'

35 'x, -z+1/4, -y+1/4'

36 'x, z, y'

37 'z, -x+1/4, -y+1/4'

38 '-z+1/4, -x+1/4, y'

39 '-z+1/4, x, -y+1/4'

40 'z, x, y'

41 '-y+1/4, z, -x+1/4'

42 'y, -z+1/4, -x+1/4'

43 '-y+1/4, -z+1/4, x'

44 'y, z, x'

45 '-x+1/4, -y+1/4, z'

46 '-x+1/4, y, -z+1/4'

47 'x, -y+1/4, -z+1/4'

48 'x, y, z'

49 '-z, y+1/4, x+1/4'

50 'z+3/4, -y+1/2, x+1/4'

51 'z+3/4, y+1/4, -x+1/2'

52 '-z, -y+1/2, -x+1/2'

53 'y+3/4, x+1/4, -z+1/2'

54 '-y, x+1/4, z+1/4'

55 'y+3/4, -x+1/2, z+1/4'

56 '-y, -x+1/2, -z+1/2'

57 'x+3/4, -z+1/2, y+1/4'

58 'x+3/4, z+1/4, -y+1/2'

59 '-x, z+1/4, y+1/4'

60 '-x, -z+1/2, -y+1/2'

61 '-z, x+1/4, y+1/4'

62 'z+3/4, x+1/4, -y+1/2'

63 'z+3/4, -x+1/2, y+1/4'

64 '-z, -x+1/2, -y+1/2'

65 'y+3/4, -z+1/2, x+1/4'

66 '-y, z+1/4, x+1/4'

67 'y+3/4, z+1/4, -x+1/2'

68 '-y, -z+1/2, -x+1/2'

69 'x+3/4, y+1/4, -z+1/2'

70 'x+3/4, -y+1/2, z+1/4'

71 '-x, y+1/4, z+1/4'

72 '-x, -y+1/2, -z+1/2'

73 'z, -y+3/4, -x+3/4'

74 '-z+1/4, y+1/2, -x+3/4'

75 '-z+1/4, -y+3/4, x+1/2'

76 'z, y+1/2, x+1/2'

77 '-y+1/4, -x+3/4, z+1/2'

78 'y, -x+3/4, -z+3/4'

79 '-y+1/4, x+1/2, -z+3/4'

80 'y, x+1/2, z+1/2'

81 '-x+1/4, z+1/2, -y+3/4'

82 '-x+1/4, -z+3/4, y+1/2'

83 'x, -z+3/4, -y+3/4'

84 'x, z+1/2, y+1/2'

85 'z, -x+3/4, -y+3/4'

86 '-z+1/4, -x+3/4, y+1/2'

87 '-z+1/4, x+1/2, -y+3/4'

88 'z, x+1/2, y+1/2'

89 '-y+1/4, z+1/2, -x+3/4'

90 'y, -z+3/4, -x+3/4'

91 '-y+1/4, -z+3/4, x+1/2'

92 'y, z+1/2, x+1/2'

93 '-x+1/4, -y+3/4, z+1/2'

94 '-x+1/4, y+1/2, -z+3/4'

95 'x, -y+3/4, -z+3/4'

96 'x, y+1/2, z+1/2'

97 '-z+1/2, y+3/4, x+1/4'

98 'z+1/4, -y, x+1/4'

99 'z+1/4, y+3/4, -x+1/2'

100 '-z+1/2, -y, -x+1/2'

101 'y+1/4, x+3/4, -z+1/2'

102 '-y+1/2, x+3/4, z+1/4'

103 'y+1/4, -x, z+1/4'

104 '-y+1/2, -x, -z+1/2'

105 'x+1/4, -z, y+1/4'

106 'x+1/4, z+3/4, -y+1/2'

107 '-x+1/2, z+3/4, y+1/4'

108 '-x+1/2, -z, -y+1/2'

109 '-z+1/2, x+3/4, y+1/4'

110 'z+1/4, x+3/4, -y+1/2'

111 'z+1/4, -x, y+1/4'

112 '-z+1/2, -x, -y+1/2'

113 'y+1/4, -z, x+1/4'

114 '-y+1/2, z+3/4, x+1/4'

115 'y+1/4, z+3/4, -x+1/2'

116 '-y+1/2, -z, -x+1/2'

117 'x+1/4, y+3/4, -z+1/2'

118 'x+1/4, -y, z+1/4'

119 '-x+1/2, y+3/4, z+1/4'

120 '-x+1/2, -y, -z+1/2'

121 'z+1/2, -y+1/4, -x+3/4'

122 '-z+3/4, y, -x+3/4'

123 '-z+3/4, -y+1/4, x+1/2'

124 'z+1/2, y, x+1/2'

125 '-y+3/4, -x+1/4, z+1/2'

126 'y+1/2, -x+1/4, -z+3/4'

127 '-y+3/4, x, -z+3/4'

128 'y+1/2, x, z+1/2'

129 '-x+3/4, z, -y+3/4'

130 '-x+3/4, -z+1/4, y+1/2'

131 'x+1/2, -z+1/4, -y+3/4'

132 'x+1/2, z, y+1/2'

133 'z+1/2, -x+1/4, -y+3/4'

134 '-z+3/4, -x+1/4, y+1/2'

135 '-z+3/4, x, -y+3/4'

136 'z+1/2, x, y+1/2'

137 '-y+3/4, z, -x+3/4'

138 'y+1/2, -z+1/4, -x+3/4'

139 '-y+3/4, -z+1/4, x+1/2'

140 'y+1/2, z, x+1/2'

141 '-x+3/4, -y+1/4, z+1/2'

142 '-x+3/4, y, -z+3/4'

143 'x+1/2, -y+1/4, -z+3/4'

144 'x+1/2, y, z+1/2'

145 '-z+1/2, y+1/4, x+3/4'

146 'z+1/4, -y+1/2, x+3/4'

147 'z+1/4, y+1/4, -x'

148 '-z+1/2, -y+1/2, -x'

149 'y+1/4, x+1/4, -z'

150 '-y+1/2, x+1/4, z+3/4'

151 'y+1/4, -x+1/2, z+3/4'

152 '-y+1/2, -x+1/2, -z'

153 'x+1/4, -z+1/2, y+3/4'

154 'x+1/4, z+1/4, -y'

155 '-x+1/2, z+1/4, y+3/4'

156 '-x+1/2, -z+1/2, -y'

157 '-z+1/2, x+1/4, y+3/4'

158 'z+1/4, x+1/4, -y'

159 'z+1/4, -x+1/2, y+3/4'

160 '-z+1/2, -x+1/2, -y'

161 'y+1/4, -z+1/2, x+3/4'

162 '-y+1/2, z+1/4, x+3/4'

163 'y+1/4, z+1/4, -x'

164 '-y+1/2, -z+1/2, -x'

165 'x+1/4, y+1/4, -z'

166 'x+1/4, -y+1/2, z+3/4'

167 '-x+1/2, y+1/4, z+3/4'

168 '-x+1/2, -y+1/2, -z'

169 'z+1/2, -y+3/4, -x+1/4'

170 '-z+3/4, y+1/2, -x+1/4'

171 '-z+3/4, -y+3/4, x'

172 'z+1/2, y+1/2, x'

173 '-y+3/4, -x+3/4, z'

174 'y+1/2, -x+3/4, -z+1/4'

175 '-y+3/4, x+1/2, -z+1/4'

176 'y+1/2, x+1/2, z'

177 '-x+3/4, z+1/2, -y+1/4'

178 '-x+3/4, -z+3/4, y'

179 'x+1/2, -z+3/4, -y+1/4'

180 'x+1/2, z+1/2, y'

181 'z+1/2, -x+3/4, -y+1/4'

182 '-z+3/4, -x+3/4, y'

183 '-z+3/4, x+1/2, -y+1/4'

184 'z+1/2, x+1/2, y'

185 '-y+3/4, z+1/2, -x+1/4'

186 'y+1/2, -z+3/4, -x+1/4'

187 '-y+3/4, -z+3/4, x'

188 'y+1/2, z+1/2, x'

189 '-x+3/4, -y+3/4, z'

190 '-x+3/4, y+1/2, -z+1/4'

191 'x+1/2, -y+3/4, -z+1/4'

192 'x+1/2, y+1/2, z'

loop_

_atom_type_symbol

_atom_type_oxidation_number

Li1+ 1

Mn3+ 3.5

O2- -2

loop_

_atom_site_label

_atom_site_type_symbol

_atom_site_symmetry_multiplicity

_atom_site_Wyckoff_symbol

_atom_site_fract_x

_atom_site_fract_y

_atom_site_fract_z

_atom_site_B_iso_or_equiv

_atom_site_occupancy

_atom_site_attached_hydrogens

Li1 Li1+ 8 a 0.125 0.125 0.125 0.35(38) 1. 0

Mn1 Mn3+ 16 d 0.5 0.5 0.5 0.63(11) 1. 0

O1 O2- 32 e 0.2628(2) 0.2628(2) 0.2628(2) 1.09(8) 1. 0

#End of TTdata_50415-ICSD

References

1. Mohanty, D. & Gabrisch, H. Microstructural investigation of LixNi1/3Mn1/3Co1/3O2 (x ≤ 1) and its aged products via magnetic and diffraction study. *J. Power Sources* **220,** 405–412 (2012).
2. Whitfield, P., Davidson, I., Cranswick, L., Swainson, I. & Stephens, P. Investigation of possible superstructure and cation disorder in the lithium battery cathode material LiMnNiCoO using neutron and anomalous dispersion powder diffraction. *Solid State Ionics* **176,** 463–471 (2005).
3. Ben-Kamel, K., Amdouni, N., Mauger, a. & Julien, C. M. Study of the local structure of LiNi0.33+δMn0.33+δCo0.33−2δO2 (0.025≤δ≤0.075) oxides. *J. Alloys Compd.* **528,** 91–98 (2012).
4. Kushnir, D. & Sandén, B. a. Multi-level energy analysis of emerging technologies: a case study in new materials for lithium ion batteries. *J. Clean. Prod.* **19,** 1405–1416 (2011).
5. Song, M.-K., Park, S., Alamgir, F. M., Cho, J. & Liu, M. Nanostructured electrodes for lithium-ion and lithium-air batteries: the latest developments, challenges, and perspectives. *Mater. Sci. Eng. R Reports* **72,** 203–252 (2011).
6. Eriksson, T. O. M. *LiMn 2 O 4 as a Li-Ion Battery Cathode*. (2001).
7. Rao, M. M. *et al.* High-temperature combustion synthesis and electrochemical characterization of LiNiO2, LiCoO2 and LiMn2O4 for lithium-ion secondary batteries. *J. Solid State Electrochem.* **5,** 348–354 (2001).
8. Mukherjee, R., Krishnan, R., Lu, T.-M. & Koratkar, N. Nanostructured electrodes for high-power lithium ion batteries. *Nano Energy* **1,** 518–533 (2012).
9. Arthur, T. S. *et al.* Three-dimensional electrodes and battery architectures. *MRS Bull.* **36,** 523–531 (2011).
10. Swainson, I. & Nazar, L. F. X-ray / Neutron Diffraction and Electrochemical Studies of Lithium. **2,** 1901–1910 (2006).

11. Levasseur, S., Menetrier, M., Suard, E. & Delmas, C. Evidence for structural defects in non-stoichiometric HT-LiCoO 2 : electrochemical , electronic properties and Li NMR studies. **128,** 11–24 (2000).
12. Dahn, J. R. & Michal, C. A. Structure and electrochemistry of Lil *,NiOz and a new Li2Ni02 phase with the Ni (OH) 2 structure. **44,** 87–97 (1990).
13. Sharma, N. *et al.* Structural changes in a commercial lithium-ion battery during electrochemical cycling: An in situ neutron diffraction study. *J. Power Sources* **195,** 8258–8266 (2010).
14. Park, B., Kim, Y. J. & Cho, J. Chapter 14 CATHODES BASED ON LiCoO 2 AND LiNiO 2.
15. Sharma, N. & Peterson, V. K. Current-dependent electrode lattice fluctuations and anode phase evolution in a lithium-ion battery investigated by in situ neutron diffraction. *Electrochim. Acta* **101,** 79–85 (2013).
16. Molenda, J., Wilk, P. & Marzec, J. Structural , electrical and electrochemical properties of LiNiO 2. **146,** 73–79 (2002).
17. Berg, H. & Thomas, J. O. Neutron diffraction study of electrochemically delithiated LiMn 2 O 4 spinel. **126,** 227–234 (1999).
18. Kim, D. K. *et al.* Spinel LiMn2O4 nanorods as lithium ion battery cathodes. *Nano Lett.* **8,** 3948–52 (2008).
19. Lee, S. *et al.* In Situ TEM Observation of Local Phase Transformation in a Rechargeable LiMn 2 O 4 Nanowire Battery. **12,** (2013).
20. Zhecheva, E. & Stoyanova, R. SOLID STATE IOWICS Stabilization of the layered crystal structure of LiNi02 by Co-substitution. **66,** (1993).
21. Cadi-ayyad, U. & Sciences-semlalia, F. positive electrode materials: rela tionships bet ween the structure, physical properties and electrochemical behaviour. **6,** 193–199 (1996).
22. Process, D., Co, N., Nakai, I. & Nakagome, T. In Situ Transmission X-Ray Absorption Fine Structure Analysis of the Li. **1,** 259–261 (1998).
23. Grey, C. P., Yoon, W.-S., Reed, J. & Ceder, G. Electrochemical Activity of Li in the Transition-Metal Sites of O3 Li[Li[sub (1−2x)/3]Mn[sub (2−x)/3]Ni[sub x]]O[sub 2]. *Electrochem. Solid-State Lett.* **7,** A290 (2004).

24. Armstrong, A. R., Paterson, A. J., Robertson, A. D. & Bruce, P. G. Nonstoichiometric Layered Li x Mn y O 2 with a High Capacity for Lithium Intercalation / Deintercalation. 710–719 (2002).
25. Armstrong, A. R., Robertson, A. D. & Bruce, P. G. Structural transformation on cycling layered Li (Mn 1 À y Co y) O 2 cathode materials. **45,** 285–294 (1999).
26. Spahr, M. E., Novák, P., Schnyder, B., Haas, O. & Nesperh, R. Characterization of Layered Lithium Nickel Manganese Oxides Synthesized by a Novel Oxidative Coprecipitation Method and Their Electrochemical Performance as Lithium Insertion Electrode Materials. **145,** 1113–1121 (1998).
27. Shaju, K. ., Subba Rao, G. . & Chowdari, B. V. . Li-ion kinetics and polarization effect on the electrochemical performance of Li(Ni1/2Mn1/2)O2. *Electrochim. Acta* **49,** 1565–1576 (2004).
28. Arachi, Y. *et al.* Structural Change of Li 1 À x Ni 0 : 5 Mn 0 : 5 O 2 Cathode Materials for Lithium-ion Batteries by Synchrotron Radiation. **32,** 60–61 (2003).
29. Yang, X., Mcbreen, J., Yoon, W. & Grey, C. P. Crystal structure changes of LiMn 0 : 5 Ni 0 : 5 O 2 cathode materials during charge and discharge studied by synchrotron based in situ XRD. **4,** 649–654 (2002).
30. Ohzuku, T. & Makimura, Y. 642 Chemistry Letters 2001. 642–643 (2001).
31. Kim, J.-M. & Chung, H.-T. Role of transition metals in layered Li[Ni,Co,Mn]O2 under electrochemical operation. *Electrochim. Acta* **49,** 3573–3580 (2004).
32. Swainson, I. & Nazar, L. F. X-ray / Neutron Diffraction and Electrochemical Studies of Lithium. **2,** 1901–1910 (2006).
33. Yu, H. & Zhou, H. High-Energy Cathode Materials (Li 2 MnO 3 − LiMO 2) for Lithium-Ion Batteries. (2013).
34. Myung, S., Komaba, S. & Kumagai, N. Effect of excess lithium on LiNi0.5Mn0.5O2+δ and its electrochemistry as lithium insertion material. *Solid State Ionics* **170,** 139–144 (2004).
35. Kang, S.-H., Sun, Y. K. & Amine, K. Electrochemical and Ex Situ X-Ray Study of Li(Li[sub 0.2]Ni[sub 0.2]Mn[sub 0.6])O[sub 2] Cathode Material for Li Secondary Batteries. *Electrochem. Solid-State Lett.* **6,** A183 (2003).

36. Kim, J. Synthesis and electrochemical behavior of Li[Li0.1Ni0.35−x/2CoxMn0.55−x/2]O2 cathode materials. *Solid State Ionics* **164,** 43–49 (2003).
37. Zheng, J. *et al.* Corrosion/Fragmentation of Layered Composite Cathode and Related Capacity/Voltage Fading during Cycling Process. (2013).
38. Liu, J. *et al.* General synthesis of xLi2MnO3·(1 − x)LiMn1/3Ni1/3Co1/3O2 nanomaterials by a molten-salt method: towards a high capacity and high power cathode for rechargeable lithium batteries. *J. Mater. Chem.* **22,** 25380 (2012).
39. Zhao, T. *et al.* Synthesis, characterization, and electrochemistry of cathode material Li[Li0.2Co0.13Ni0.13Mn0.54]O2 using organic chelating agents for lithium-ion batteries. *J. Power Sources* **228,** 206–213 (2013).
40. Jarvis, K. a., Deng, Z., Allard, L. F., Manthiram, A. & Ferreira, P. J. Atomic Structure of a Lithium-Rich Layered Oxide Material for Lithium-Ion Batteries: Evidence of a Solid Solution. *Chem. Mater.* **23,** 3614–3621 (2011).
41. Jin, X., Xu, Q., Yuan, X., Zhou, L. & Xia, Y. Synthesis, characterization and electrochemical performance of Li[Li0.2Mn0.54Ni0.13Co0.13]O2cathode materials for lithium-ion batteries. *Electrochim. Acta* **114,** 605–610 (2013).
42. Li, L. *et al.* Synthesis and electrochemical performance of cathode material Li1.2Co0.13Ni0.13Mn0.54O2 from spent lithium-ion batteries. *J. Power Sources* **249,** 28–34 (2014).
43. Par, H. K. Study of Li-rich lamellar oxides as positive electrode materials for lithium-ion batteries. (2013).
44. Ishida, N. & Fujita, D. Chemical-state imaging of Li using scanning Auger electron microscopy. *J. Electron Spectros. Relat. Phenomena* **186,** 39–43 (2013).
45. Johnson, B. Y., Edington, J., Williams, a. & O'Keefe, M. J. Microstructural characteristics of cerium oxide conversion coatings obtained by various aqueous deposition methods. *Mater. Charact.* **54,** 41–48 (2005).
46. Periodicals, W. CASINO V2 . 42 — A Fast and Easy-to-use Modeling Tool for Scanning Electron Microscopy and Microanalysis Users. **29,** 92–101 (2007).

47. Liu, H., Fell, C. R., An, K., Cai, L. & Meng, Y. S. In-situ neutron diffraction study of the xLi2MnO3·(1 − x)LiMO2 (x = 0, 0.5; M = Ni, Mn, Co) layered oxide compounds during electrochemical cycling. *J. Power Sources* **240,** 772–778 (2013).
48. Jarvis, K. a., Deng, Z., Allard, L. F., Manthiram, A. & Ferreira, P. J. Understanding structural defects in lithium-rich layered oxide cathodes. *J. Mater. Chem.* **22,** 11550 (2012).
49. Lee, J. T. *et al.* Comparative study of the solid electrolyte interphase on graphite in full Li-ion battery cells using X-ray photoelectron spectroscopy, secondary ion mass spectrometry, and electron microscopy. *Carbon N. Y.* **52,** 388–397 (2013).
50. Shaju, K. M., Subba Rao, G. V. & Chowdari, B. V. R. Influence of Li-Ion Kinetics in the Cathodic Performance of Layered Li(Ni[sub 1/3]Co[sub 1/3]Mn[sub 1/3])O[sub 2]. *J. Electrochem. Soc.* **151,** A1324 (2004).
51. Gabrisch, H., Yazami, R. & Fultz, B. A transmission electron microscopy study of cycled LiCoO2. *J. Power Sources* **119-121,** 674–679 (2003).
52. Gabrisch, H., Yi, T. & Yazami, R. Transmission Electron Microscope Studies of LiNi[sub 1/3]Mn[sub 1/3]Co[sub 1/3]O[sub 2] before and after Long-Term Aging at 70°C. *Electrochem. Solid-State Lett.* **11,** A119 (2008).
53. Wang, L. *et al.* Recent advances in layered LiNi x CoyMn1−x−y O2 cathode materials for lithium ion batteries. *J. Solid State Electrochem.* **13,** 1157–1164 (2008).
54. Yoon, W.-S. *et al.* Local Structure and Cation Ordering in O3 Lithium Nickel Manganese Oxides with Stoichiometry Li[Ni[sub x]Mn[sub (2−x)/3]Li[sub (1−2x)/3]]O[sub 2]. *Electrochem. Solid-State Lett.* **7,** A167 (2004).
55. Weill, F., Tran, N., Croguennec, L. & Delmas, C. Cation ordering in the layered Li1+x(Ni0.425Mn0.425Co0.15)1−xO2 materials (x=0 and 0.12). *J. Power Sources* **172,** 893–900 (2007).
56. Ito, A. *et al.* Cyclic deterioration and its improvement for Li-rich layered cathode material Li[Ni0.17Li0.2Co0.07Mn0.56]O2. *J. Power Sources* **195,** 567–573 (2010).
57. Ito, A. *et al.* Direct observation of the partial formation of a framework structure for Li-rich layered cathode material Li[Ni0.17Li0.2Co0.07Mn0.56]O2 upon the first charge and discharge. *J. Power Sources* **196,** 4785–4790 (2011).

58. Nayak, P. K., Grinblat, J., Levi, M., Markovsky, B. & Aurbach, D. Structural and Electrochemical Evidence of Layered to Spinel Phase Transformation of Li and Mn Rich Layered Cathode Materials of the Formulae xLi[Li1/3Mn2/3]O2.(1-x)LiMn1/3Ni1/3Co1/3O2 (x = 0.2, 0.4, 0.6) upon Cycling. *J. Electrochem. Soc.* **161,** A1534–A1547 (2014).